ISBN 0-315-54966-1

SUBSTRUCTURAL EVOLUTION, STRENGTHENING AND FRACTURE MECHANISMS IN AISI 4340 STEEL

by

Jonathan K. Cuddy

A thesis presented to
the University of Manitoba
in partial fulfillment of the
requirements for the degree of
Master of Science
in
Mechanical Engineering

Metallurgical Science Laboratories

Winnipeg, Manitoba

1988

SUBSTRUCTURAL EVOLUTION, STRENGTHENING AND FRACTURE MECHANISMS IN AISI 4340 STEEL

by

JONATHAN K. CUDDY

A thesis submitted to the Faculty of Graduate Studies of the University of Manitoba in partial fulfillment of the requirements of the degree of

MASTER OF SCIENCE

ABSTRACT

The evolution of substructure and the mechanisms of substructure strengthening during plastic deformation were studied in a commercial low alloy steel. The microscopic processes leading to ductile fracture of the material were also investigated. Tensile and microhardness tests were performed on three sample groups of AISI 4340 steel, each containing a different initial proeutectoid ferrite grain size. The room temperature mechanical properties were correlated with the ferrite grain size and other microstructural parameters determined by optical metallography. The influence of microstructure on substructural evolution and fracture mechanisms was also evaluated using transmission and scanning electron microscopy.

It was determined that the yielding behaviour is strongly dependent on the proeutectoid ferrite grain size in the steel groups, whereas the work hardening and flow properties are unaffected by this parameter. The flow curve of the steel can be divided into two distinct stages, based on both the macroscopic and microscopic observations. In stage 1, extending from the yield stress to the ultimate stress, the work hardening behaviour of the material is largely controlled by strengthening mechanisms in pearlite, where the cementite platelets act as rigid barriers to dislocation motion in the ferrite lamellae. As the platelets begin to shear at about the ultimate tensile strength, the increase in dislocation mobility results in larger plastic strains and cell evolution in the ferrite phase during stage 2. It was found that an inverse, linear strengthening relationship between cell size and flow stress is obeyed during this stage. At strains near the onset of fracture, the occurrence of subgrains and a very low work hardening rate indicate a possible transition to a new stage of plastic deformation. The exact nature of this stage could not be evaluated due to the onset of tensile instability and fracture in the material.

The study of ductile fracture mechanisms based on the combined TEM and SEM results suggest that microcracks are initiated at cementite platelets in pearlite under the

combined influence of tensile loading and localized shear in the adjacent ferrite. Microcracks then propagate through the ferrite grains by the nucleation and coalescence of voids along the well-developed cell wall structure, resulting in ductile fracture of the material.

This study has resulted in a greater understanding of the role of both microstructure and dislocation substructure in the processes of plastic deformation and fracture of steels, an important class of engineering materials.

ACKNOWLEDGEMENTS

The author would like to thank Dr. M.N. Bassim for the suggestion of this thesis topic and for his supervision and constant encouragement throughout the course of the research work.

Special thanks are due to Messrs. J. Van Dorp, D. Mardis, R. Hartle, R. Crampton and Y.J. Chang for their excellent technical assistance and their friendship. The financial support of the Natural Sciences and Engineering Research Council in the form of a post-graduate scholarship is gratefully acknowledged.

TABLE OF CONTENTS

page

page

page

LIST OF TABLES

LIST OF FIGURES

Chapter I

INTRODUCTION

The mechanical behaviour of materials undergoing plastic deformation is of considerable importance in many aspects of the design of engineering structures. For example, consideration of plastic deformation processes is necessary in the design of alloys exposed to fatigue, creep, wear, etc., during service. The most economical use of a material requires the exploitation of its load-bearing capacity well-beyond yielding without incurring the costly and sometimes disastrous consequences of fracture. The properties of plastically deformed metals is of particular concern in the fabrication of engineering components by mechanical working processes such as rolling and drawing.

Different approaches have been used to characterize the strength and ductility of metals undergoing plastic deformation. The continuum mechanics approach treats a material as an ideal, homogeneous, and isotropic body in order that plasticity theory may be applied to develop a mathematical description of the plastic deformation process. From a microscopic viewpoint however, it has long been realized that plastic deformation is an inhomogeneous process involving the creation and propagation of discrete crystalline defects known as dislocations. It has also been recognized that materials are heterogeneous and anisotropic at the microstructural level, and that mechanical properties are strongly dependent upon composition and microstructure. Therefore, the design of alloys requires a careful control of microstructural parameters to achieve the optimum combination of mechanical properties for a given application. This has led to a considerable amount of research over the last 30 years, on the part of materials scientists and metallurgists, aimed towards developing quantitative relationships between structure and properties. The basic flow and fracture properties derived from tensile and impact testing of iron-carbon (steel) microstructures have received particular attention.

The properties of alloys such as steel are influenced by a variety of strengthening mechanisms which include solid solution strengthening, precipitation hardening, grain boundary strengthening, and strain (or work) hardening. It is well known that work hardening, or increasing resistance to further deformation during plastic straining, is caused by the interaction of dislocations with each other and with microstructural barriers which impede their motion. In materials deformed to appreciable strains, the development of an inhomogeneous arrangement of dislocations, or dislocation substructure, is commonly observed by transmission electron microscopy. Often, the substructure is in the form of "cells" in which high-density dislocation tangles form walls enclosing low dislocation density regions. The exact nature of the dislocation substructure depends on the material, and the strain, strain rate, and temperature of deformation.

It has been experimentally determined that the scale of the dislocation cell structure depends primarily on the applied stress and once formed, the substructure can strongly influence the mechanical properties of a material during subsequent deformation. The theoretical aspects of the strengthening mechanism associated with dislocation cell structure evolution have been addressed in detail in the theory of work hardening of Kuhlmann-Wilsdorf.

Most of the experimental investigations concerning dislocation substructural evolution and substructural strengthening have focussed on relatively pure, single phase materials subject to moderate plastic strains. Few studies have been carried out on complex alloys due to the difficulty of assessing the various strengthening contributions from microstructural parameters. Even less attention has been given to the role of a well-developed dislocation substructure in the fracture process of ductile materials. A number of previous studies by Bassim and co-workers had identified dislocation cell structures in low alloy steels, and had found qualitative evidence in support of the work hardening theory of Kuhlmann-Wilsdorf for complex metals. Their studies had also suggested that cell structures may play a role in the micromechanisms of ductile fracture. However, the

influence of microstructural parameters on cell formation and the quantitative strengthening effect of cells were not considered.

The objective of this thesis is therefore to extend the study of substructural strengthening in a commercially-important, low alloy steel containing a complex microstructure. The effect of microstructural parameters, such as the ferrite grain size, on the development of cells and the quantitative strengthening effect of the cell structure is assessed. Also, the validity and limitations of the Kuhlmann-Wilsdorf work hardening theory with regards to cell evolution in the steel are established. The role of well-developed dislocation cell structures in the ductile fracture process is also considered. The main goal of this work is to develop a better understanding of the substructural mechanisms of plastic deformation and fracture in a practical engineering material.

The study was conducted by evaluating the room-temperature tensile flow properties of three sample groups of annealed AISI 4340 steel, each containing a different initial ferrite grain size. The grain size and other microstructural parameters such as the inclusion distribution and pearlite interlamellar spacing were determined using optical metallography and computerized image analysis. Transmission electron microscopy was used to study the evolution of dislocation cell structures with increasing applied stress up to fracture, and to evaluate the influence of microstructural elements such as grain boundaries on cell formation. Scanning electron microscopy of tensile fracture surfaces was employed to relate the microscopic evidence of ductile fracture to the substructural mechanisms of plastic deformation preceeding it. It is hoped that this work will provide a better understanding of the role of microstructure and dislocation substructure in the processes of plastic deformation and fracture of a traditional class of engineering materials, namely steels.

Chapter II

LITERATURE REVIEW

2.1 Introduction

Studies of the relation between microstructure and mechanical properties in metals and alloys have attempted to gain a better understanding of the operative strengthening mechanisms. This has been a very complex problem due to the number of strengthening variables arising from solid solution alloying, precipitation hardening, phase transformations, grains size effects, and strain hardening. From a microscopic viewpoint, it has long been recognized that the generation, multiplication, and interaction of dislocations underlies the observed strengthening due to strain or work hardening. Attempts have been made to introduce stable substructural arrangements of dislocations using mechanical-thermal treatments in order to improve the mechanical properties of materials which do not undergo strengthening from phase transformations.

The purpose of this review is to examine some aspects of the work hardening and strengthening of metals as a result of the evolution of dislocation substructure. Other microstructural strengthening effects arising from solid solution alloying, precipitation hardening, and phase transformations have been reviewed elsewhere [1-3] and are not considered here. The discussion is focussed on substructure evolution during low (room) temperature, quasi-static straining where slip is the dominant deformation mechanism, and twinning and diffusional contributions are usually small. The work hardening behaviour of single crystals and polycrystalline metals is presented, with consideration of the strengthening contribution from grain boundaries. Some aspects of substructure evolution during the deformation of metals are reviewed, including those containing two-phase microstructures, which are of particular interest in this study. A brief overview of some empirical expressions relating flow stress to substructure, as well as some theoretical work hardening models of the relationship are presented. Special emphasis is given to the "mesh

length" theory of work hardening due to its significance in the present work. Finally, a brief look at some microstructural aspects of ductile fracture is given.

2.2 Deformation of Single Crystals

The plastic flow of single crystals occurs by slip of dislocations on certain crystallographic planes and in particular directions. Under uniaxial strain, those planes experiencing the highest resolved shear stress will initiate dislocation glide, with the magnitude of this critical stress determined by the type of metal and its purity, the temperature of deformation, and the orientation of the slip planes with respect to the tensile axis [4]. When tensile data for single crystals is plotted as resolved shear stress vs shear strain, three distinct stages of work hardening can often be distinguished as shown in Figure 2.1.

Stage I work hardening is the region of "easy glide" which occurs in crystals so oriented that slip initially occurs on a single slip system only. Transmission electron microscopy (TEM) reveals that dislocations move over relatively large distances on "primary" slip planes, resulting in the parallel slip lines observed when dislocations intersect the crystal surface. Due to the small degree of interaction and high mobility of dislocations, the work hardening coefficient (rate) in this stage , θ_I, is quite low and is typically equal to ~ G/10,000, where G is the shear modulus.

The onset of stage II is associated with the activation and multiplication of dislocations on "secondary" slip systems. Thus, crystals oriented such that more than one slip system operates at the start of deformation will show little or no evidence of stage I hardening. The interaction between dislocations on intersecting glide planes produces many barriers which decrease the average slip line length, resulting in rapid, linear work hardening during stage II. Experimentally, the work hardening coefficient in stage II, θ_{II}, is found to be 3-10 times larger than that in stage I [4]. The value of θ_{II} is also found to be independent of temperature.

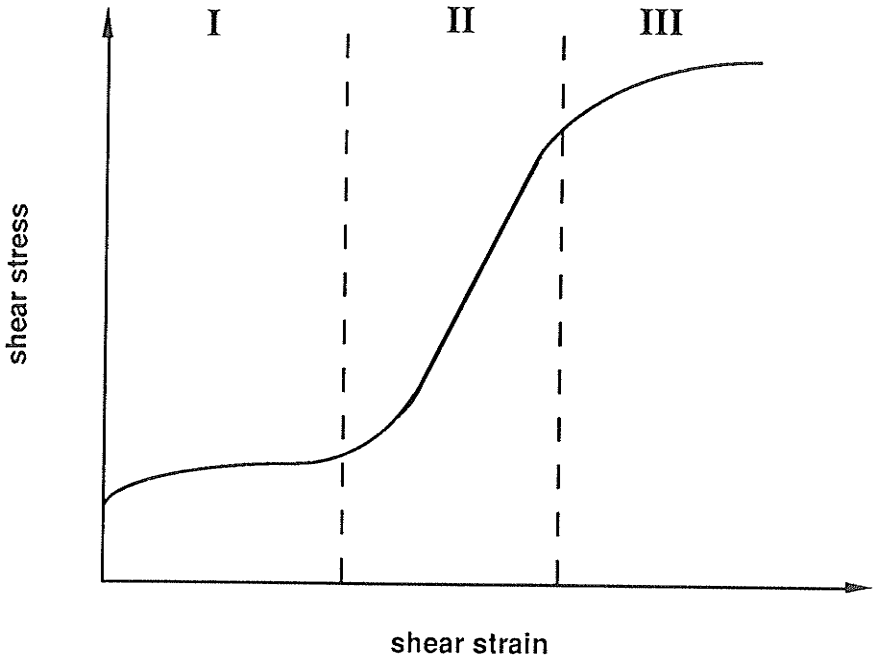

Figure 2.1 Three-stage work hardening curve for single crystals

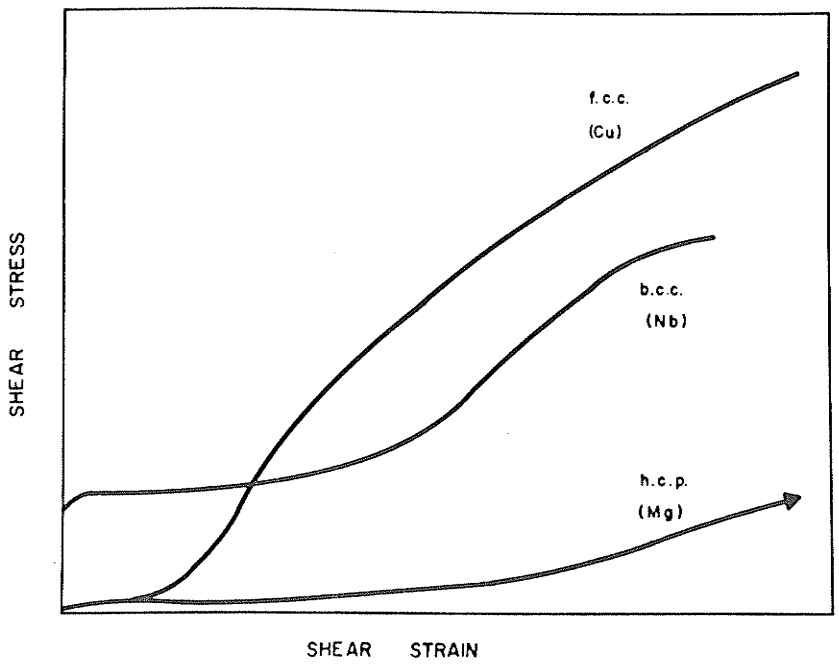

Figure 2.2 Stress-strain curves of FCC, BCC, and HCP single crystals (after ref. 24)

Stage III represents the region of a decreasing work hardening rate where the flow curve is roughly parabolic in shape. This region is generally associated with "dynamic recovery", involving dislocation cross slip and/or climb mechanisms activated at higher stresses [5]. These processes are also known to be thermally activated, which is reflected in the strong temperature dependence of the work hardening rate in stage III. Figure 2.2 compares the room temperature work hardening behaviour of FCC, BCC, and HCP crystals. The cubic crystals show much larger work hardening compared with the hexagonal structures, where slip is limited to basal plane glide (stage I behaviour).

Some investigators have suggested a further stage IV hardening region where the flow curve levels off to a low, nearly constant work hardening rate at large strains [6-8]. There is, however, a general lack of experimental data on the large strain behaviour of materials.

2.3 Polycrystalline Deformation

2.3.1 Overview

The most important difference between single crystals and polycrystals is the presence of grain boundaries which separate the material into individual crystallites of different orientations. A single crystal is free to deform on one slip system, whereas an individual grain of a polycrystal must accomodate the plastic shape changes of neighboring grains, and remain in contact with them. In order for a polycrystal to undergo general plastic shape changes while maintaining constant volume and continuity between grains requires the operation of five independent slip systems. This is known as the von Mises condition, and it explains the general ductility of most FCC and BCC metals (such as Cu and Fe) which have many active slip systems, compared with HCP metals (such as Zn and Mg) where 5 independent slip systems are not obtained and the ductility is limited. Thus, ductile polycrystalline metals are associated with multiple slip (slip on many systems) during plastic deformation and do not exhibit the three stage work hardening behaviour of

single crystals. However, stage II and III type behaviour can be found in some polycrystals as, for example, was observed by Kocks [9].

2.3.2 Grain Boundary Strengthening

Since grain boundaries are regions of high atomic misfit and large misorientation between crystals, they are relatively impenetrable and serve as strong barriers to the motion of glide dislocations. Experimentally, the strengthening effect of grain boundaries has been well established. One of the first empirical correlations of the strengthening due to grain boundaries was established by Hall [10] and Petch [11] for the grain size dependence of the lower yield stress in mild steel, namely

$$\sigma_{ys} = \sigma_i + \frac{k_y}{\sqrt{L}} \tag{2.1}$$

where σ_{ys} is the yield stress, σ_i is the friction stress opposing dislocation motion in the lattice, k_y is a material constant related to the "effectiveness" of a grain boundary in resisting slip, and L is the grain size. The Hall-Petch equation has been extended beyond yielding to express the grain size dependence of the flow stress, fatigue strength, and brittle fracture stress [12]. It should be noted that large deviations from Hall-Petch behaviour have been observed, and the relationship has been criticized for predicting infinite property values when extrapolated to very small grain sizes.

The original interpretation of eqn. (2.1) by Petch [11] was based on a pile-up model of the grain boundary. In this model, slip is propagated from one grain to another when the stress concentration at the head of a dislocation pile-up at the boundary becomes sufficient to operate a dislocation source in the adjacent grain. Thus by this interpretation, the strength of a grain boundary is related to the number of dislocations which pile-up against it before slip is propagated to the next grain.

Due to the general lack of experimental evidence for dislocation pile-ups, other interpretations of the strengthening property of grain boundaries have been proposed, and have been reviewed in detail by Hirth [13]. These interpretations are based on the contribution from grain boundaries to the local dislocation density, and hence, to the flow stress. For example, Li and Chou [14] have investigated the Hall-Petch equation in terms of a dislocation source model of the grain boundary, based on earlier experimental work [15] which gave evidence for the creation of dislocations at atomic ledges in the boundaries. Thompson et. al. [16,17] and Mecking [18] have modelled polycrystals as "two-phase" materials for which the grain boundary regions behave as a harder "phase" surrounding the softer grain interior "phase" due to local differences in work hardening behaviour. These models are based on Ashby's concept of "geometrically necessary" dislocations at grain boundaries, where multiple slip occurs in order to accomodate the deformation of neighboring grains [19]. In contrast, the grain interiors deform by slip on only 1 or 2 systems. Sangal and Tangri [20] have considered the hardening of the grain boundary region from an energetic viewpoint, based on the trapping of lattice dislocations by the boundary. These current theories of grain boundary strengthening are supported by experimentally observed differences in hardness [17] and dislocation arrangement [20-22] between grain interior and boundary regions.

The role of grain boundaries at large strains beyond yielding has received little attention, although it is generally noted that grain boundary strengthening diminishes due to the evolution of a dislocation substructure within the grains. The influence of grain boundaries on cell formation during plastic deformation is unclear, however.

2.4 Substructural Evolution in Deformed Metals

2.4.1 Low to Moderate Strains

Most of the early TEM studies of cold-worked substructures dealt with lightly to moderately strained single crystals exhibiting the three stage work hardening behaviour

during uniaxial straining. These studies were paramount to the understanding of the behaviour of dislocations and dislocation arrays under an applied stress, and led to a number of theories of substructure evolution and work hardening. The dislocation substructures observed in various crystals, and the early theories of work hardening have been reviewed by Nabarro et. al. [23] and Hirsch and Mitchell [24].

In single crystals oriented for multiple glide and in polycrystalline metals, profuse dislocation multiplication and interaction leads to the formation of a non-homogeneous, cellular arrangement of dislocations. The pioneering work of Keh and Weissmann [25] and Carrington et. al. [26] on BCC metals, and of Swann [27] on FCC metals found similar types of dislocation cells in both crystal structures. These cells are formed by the interconnection of dense tangles of dislocations to surround areas of a much lower dislocation density; approximately being 3 to 5 times lower. The cell walls become increasingly well defined and the distance between walls decreases as the strain increases. Furthermore, the cell walls accomodate a relative misorientation between adjacent cells, initially equal to about a degree and increasing with continued straining.

The tendency for cell formation seems dependent upon the three-dimensional mobility of dislocations, which in turn is dependent upon temperature, strain, strain rate, stacking fault energy (SFE), and impurity or alloy content of the material. The strain required to form cells tends to decrease with increasing temperature as shown in Figure 2.3 for α-iron [25]. Also, the cell formation strain is found to increase with increasing strain rate during high temperature deformation [28]. Bailey and Hirsch [29] have shown that cell formation tends to be inhibited in low SFE metals due to the restriction of tri-dimensional dislocation mobility through cross slip, with complex planar arrays of extended dislocations forming instead. With increasing strain, however, these give way to a ragged cell structure as found in aluminum and copper alloys by Swann [27], and more recently in 316L stainless steel by Kashyap et. al. [22]. Figure 2.4 shows the dependence of cell formation strain on SFE for silver-germanium alloys and stainless steels compiled

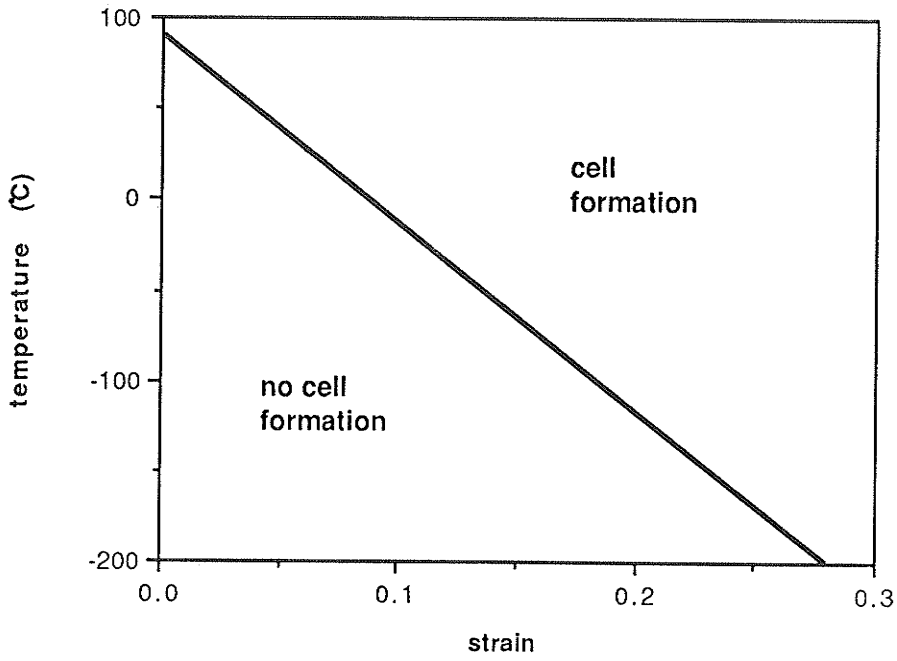

Figure 2.3 Influence of deformation strain and temperature on cell formation in iron (after ref. 25)

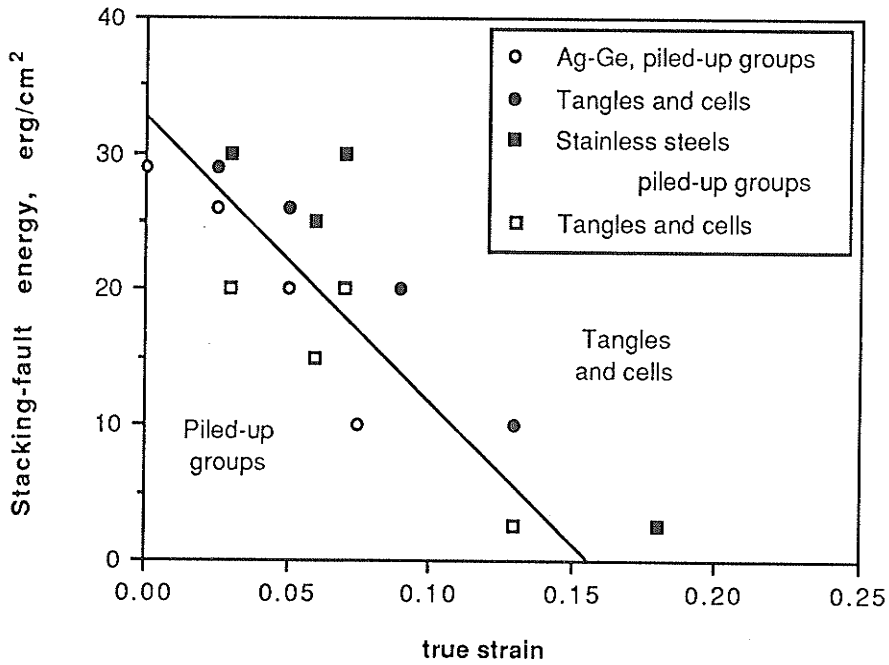

Figure 2.4 Dependence of tensile strain at which cell structures are formed on stacking-fault energy for silver-germanium alloys and stainless steels (after ref. 30)

by McElroy and Szkopiak [30]. In general, the presence of impurities and alloying additions tends to enhance the rate of dislocation generation and multiplication, leading to accelerated cell formation. However, this effect is complicated by the added influence of solid solution alloying on the SFE of many metals as was pointed out by Swann [27].

The driving force for a non-uniform arrangement of dislocations into cells is clearly a lowering of free energy such that dislocation cells, or any other arrangement, represent the configuration of lowest strain energy accessible to glide dislocations under the possible restrictions to dislocation mobility discussed earlier. Holt [31] pointed out that a uniform array of dislocations is unstable against fluctuations in density, since a reduction in elastic energy of the array can be achieved if dislocations cluster into regions of high density separating low density regions. Analogous to the theory of spinodal decomposition, he showed that the dominant wavelength of the clusters corresponds to the size of a dislocation cell. Kuhlmann-Wilsdorf [32-36] further predicted that dislocations in such an arrangement would screen one another's stress fields to the distance between neighboring dislocations, thereby reducing the long range stresses and strain energy to very low values. Computer modelling of various idealized cell structures by Bassim and Kuhlmann-Wilsdorf [37,38] confirmed this hypothesis. The preponderance of cell structures in materials deformed to appreciable strains, over dislocation arrangements associated with large long range stress fields such as pile-ups, further supports this notion.

The mechanism by which cell structures form is unclear. It was long ago proposed by Seeger [39] and Hirsch [40] that cells form as a result of screw dislocations cross-slipping from their original slip planes. This accords with the relationship between cell formation and SFE (and hence, cross slip) shown earlier. Also, a cross slip mechanism is the basis of a recent model of cell formation proposed by Jackson [41,42]. Kocks has somewhat differently modelled cell wall formation in terms of a statistical accumulation (or storage) of dislocations around "hard" areas or obstacles in the crystal produced mainly by forest dislocation bundles and particles [43].

A large body of experimental work has proven that dislocation cell formation and multiplication are typical features of stage II and III work hardening in single crystals and polycrystals strained by a number of modes. For example, cell formation is characteristic of the uniaxial deformation of copper [44,45], aluminum [46], and steel [47]. Cell structures have been observed in drawn pure Fe [48] and Fe-Ti alloy [49], and in cold-rolled Fe-3%Si [50], aluminum [51], and copper [52]. Dislocation cells have also been identified in different metals subject to fatigue [53-55], creep [56,57], and wear [58]. A valuable, up-to-date source of information on various aspects of cell structures can be found in the 1986 Proceedings of the International Conference on Low Energy Dislocation Structures [59].

2.4.2 Large Strains

The substructural features arising from large scale plastic deformation, which is of great importance to industrial metal forming processes, have received much less attention than the substructure of moderately strained materials. However, a rather exhaustive review of the subject of large strain ($\sim\varepsilon > 1.0$) deformation and work hardening has been compiled by Gil Sevillano et. al. [6,7]. Early studies of the large strain, plastic deformation of cold-drawn and rolled metals [48-50,60] indicated a number of structural departures from the cell multiplication processes characteristic of moderately strained materials. Generally, the major qualitative features of high strain deformation were found to be:

- a very low rate of cell size reduction
- a decrease in cell wall thickness and a clearing of cell interiors of dislocations
- the appearance of subgrains with well defined, two-dimensional boundaries associated with higher misorientations than cell walls

- subgrain coalescence, texture formation, and possibly dynamic recrystallization at very high strains
- a work hardening rate decreasing to a low, nearly constant value

Many subsequent experimental studies have indicated a transition from cells to subgrains with increasing strain for a variety of straining modes; including cold rolling [50,52,61], tension [62], torsion [63], and wear [58]. This transition seems to be concurrent with a decreased rate of change of substructural size in the strain range of ε = 1.0-1.5 for many different metals, as compiled by Gil Sevillano et. al. [6] in Figure 2.5. A change in the work hardening rate has also been observed at strains associated with the transitional behaviour [63-65].

Langford and Cohen [48] interpreted such a transition in drawn iron wire at $\varepsilon = 1.0$ as a transition from a work hardening stage characterized by cell multiplication, to a stage where cell wall annihilation and coalescence prevails. However, they found the actual rate of work hardening to remain nearly constant in spite of this substructural change. Others have explained a transitional behaviour as arising from dynamic recovery processes in the cell walls, whereby short-range rearrangement and annihilation of dislocations leads to a gradual transition from tangled cell walls to bidimensional (low angle) sub-boundaries [6,63,66].

According to Lucke and Mecking [5], dynamic recovery is a softening process which tends to offset work hardening during plastic deformation in stage III. It is related to a decrease in dislocation density and/or an increase in dislocation mobility occurring by either cross slip or climb mechanisms, depending on the level of stress and the temperature of deformation. Kocks [67] has theoretically predicted that dynamic recovery in polycrystals should lead to an almost negligible work hardening rate and a saturation in flow stress characteristic of stage IV, and such behaviour has been experimentally confirmed in some materials [7,63,65].

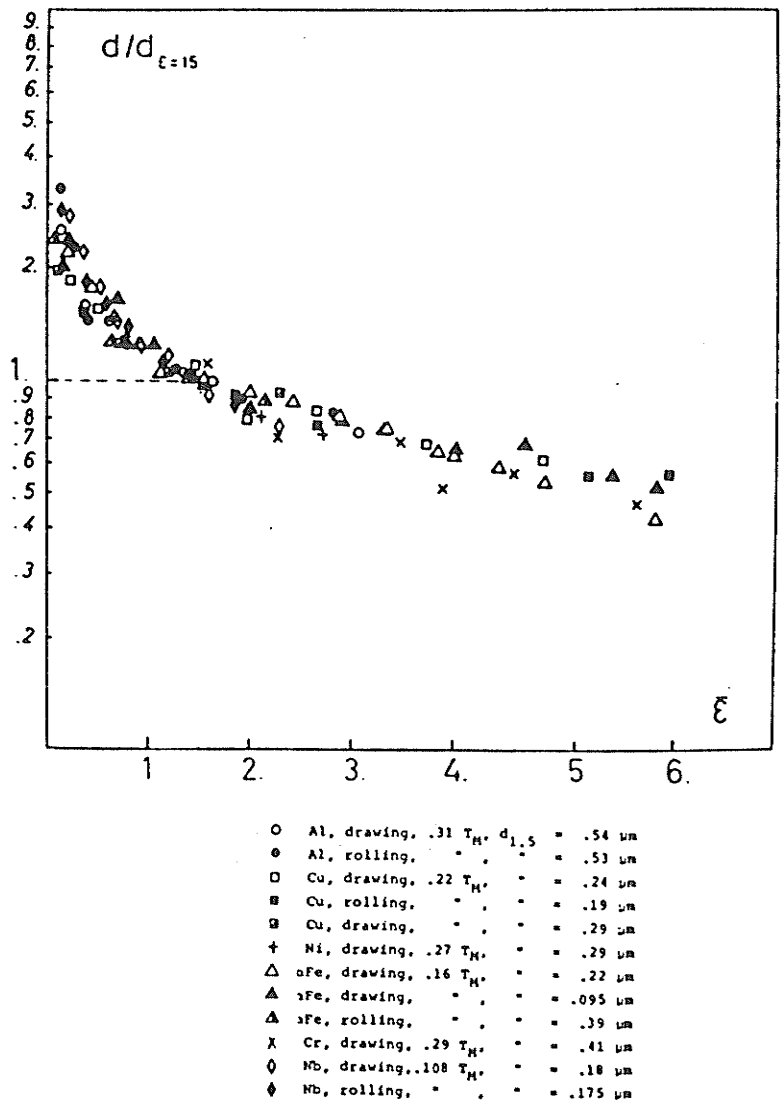

Figure 2.5 Substructural size as a function of equivalent strain relative to the size developed at $\varepsilon = 1.5$ (after ref. 6)

In addition to subgrains, Hansen and co-workers [68] have reported the presence of narrow, parallel bands of elongated subgrains, called "microbands", and narrow, continuous dislocation walls referred to as "dense dislocation walls" (DDW) at larger strains. Microbands and DDW's are apparently associated with relatively large orientation differences between adjacent areas within a grain [68], although their origin is not yet clear. Microbands have also been observed in rolled copper [69,70] and brass [71].

2.5 Deformation of Two-Phase Metals

Most of the investigations into the evolution of deformation substructure have focussed on relatively pure, single-phase metals. This is mainly due to the fact that the presence of a second phase in a heterogeneous microstructure adds considerable complexity to the development of substructure and the strengthening characteristics of a material. The morphology and distribution of the phases, the strength, work hardening characteristics, and interfacial bonding and energy are among the factors to be considered in a complete characterization. Two-phase microstructures may be categorized as either dispersed two-phase, or aggregated two-phase types of structures [2]. These two types are discussed presently.

2.5.1 Dispersed Microstructure

Work hardening and substructural evolution of metals containing a dispersion of particles will depend upon their size, strength and volume fraction as well as the degree of atomic mismatch or coherency between matrix and particle. The various strengthening effects arising from particle-dislocation interactions have been considered in detail elsewhere [2,3,72,73].

In general, particles retard the motion of dislocations either by forcing dislocations to bypass them, or by causing dislocations to accumulate around them. Ashby [74] proposed that in order to accomodate the increased strain in the matrix near particles, an

array of "geometrically necessary" dislocations have to be stored around the particles, similar to the situation for grain boundary compatibility. This array of dislocations contributes to a higher dislocation density than for the same metal without particles at a given strain and thus promotes cell formation. This notion is supported by experimental evidence associating cell wall formation with the linking-up of dislocation tangles between neighboring particles [60,75-77]. However, it has also been observed that for very small particles ($< 0.01\mu m$) and small interparticle spacing ($< 0.1\ \mu m$), cell formation is inhibited and a more uniform dislocation arrangement is promoted [60].

Hansen and Ralph [75,76] have developed theoretical strengthening models to account for the additive contributions from particles and grain boundaries. These models are in good agreement with experimental observations of dispersion-hardened copper polycrystals.

2.5.2 Aggregated Microstructure

Many aggregated two-phase metals contain the second phase in the form of quasi-continuous lamellae or fibres typified by the eutectoid structure. The structure and properties of eutectoid pearlite have been most widely studied and are of particular interest in the present work. Investigations into the work hardening and dislocation structure of pearlite have been carried out by Embury and Fisher [78], Langford [79], Gil Sevillano [80], and more recently by Dollar et. al. [81]. It was found that since the ferrite and cementite (Fe_3C) lamellae are so closely intermeshed, the two phases deform with practically the same strains. Dislocation production is favoured at the phase interfaces due to some incompatibility stresses, and the dislocation density rapidly increases in ferrite during work hardening. Langford [79] has pointed out that in order for pearlite to work harden as it does, plastic deformation of the Fe_3C phase must also occur, as has been observed [78,80]. The deformation characteristics of pearlite colonies are strongly dependent on both the orientation of the colonies with respect to the axis of the major

applied stress component and the spacing of the Fe_3C lamellae within the colonies. The cementite lamellae limit the slip distance of dislocations in ferrite, and thus the flow stress is largely governed by the interlamellar spacing.

Langford [79] modelled theoretically the strength of fine pearlite (of spacing of < 0.1 μm) in terms of the stresses required to generate and move dislocations in both ferrite and cementite phases. His analysis led to the following equation for flow stress

$$\sigma = \sigma_o + 0.35\,\overline{G}\left(\frac{b_c}{S_p}\right)^{1/2} + 0.70\,\overline{G}\left(\frac{b_f}{S_p}\right) \qquad (2.2)$$

where $\overline{G}$ is the geometric mean of the shear moduli of ferrite and cementite (= 77 x 10^3 MPa), b_c and b_f are the burgers vectors of dislocations in cementite and ferrite, respectively, S_p is the interlamellar spacing, and σ_o accounts for strengthening mechanisms which are independent of S_p. This result predicts that the strength of pearlite depends upon the interlamellar spacing, but the work hardening behaviour is largely controlled by the dislocation activity in ferrite (i.e., the 3rd term in eqn. (2.2)). This is in agreement with the work of Dollar et. al. [81] which showed that the work hardening rate is determined by the dislocation density in ferrite and is independent of the interlamellar spacing.

TEM observations of deformed pearlite have shown that a dislocation "cell" structure develops in the ferrite lamellae with an initial size determined by the interlamellar spacing [78,80]. The substructure consists mainly of transverse walls of dislocations connecting the ferrite/cementite interfaces. Where cementite lamellae have fragmented, cell walls composed of complex arrays of dislocations joining the lamellar fragments are observed [78].

2.6 Flow Stress - Substructure Relationships

Empirical relationships between flow stress and dislocation substructure have arisen from experimental observations of similar substructures produced in a number of metals independent of the mode of deformation. The qualitative features of these substructures were discussed earlier. These observations led to the conclusion that the dislocation substructure provides an indication of the macroscopic deformed state of metals, and that changes in certain substructural parameters should be related to changes in applied flow stress.

Most correlations between flow stress and substructure have been based on a single parameter description. The most fundamental parameter of the cold worked substructure of metals is the dislocation density. Dislocation density, ρ, has been correlated with both the critical resolved shear stress, τ, and the applied normal stress, σ, by the well known expressions

$$\tau = \tau_o + \alpha Gb\sqrt{\rho} \tag{2.3a}$$

and

$$\sigma = \sigma_o + \alpha' Gb\sqrt{\rho} \tag{2.3b}$$

where τ_o and σ_o are the shear and normal friction stresses, G is the shear modulus, b is the burgers vector, and α and α' are constants relating dislocation density to the applied stress with $\alpha' = M\alpha$, where M is an orientation factor for polycrystals. The parameter α has been found to vary between 0.3 and 0.6 in various metals. This equation stems from the earliest model of dislocation interactions by Taylor [82], and is predicted by nearly all modern work hardening theories. The relationship is not easily verified beyond moderate values of strain due to inhomogeneous distributions of dislocations which make the direct measurement of dislocation density very difficult.

An analysis by Holt [31] showed that the most frequent size of dislocation cell structures, d, for a given dislocation density, ρ, is given by

$$d = \frac{K}{\sqrt{\rho}} \tag{2.4}$$

This equation was subsequently verified for strained copper by Staker and Holt [44]. Combining equations (2.3b) and (2.4) results in

$$\sigma = \sigma_0 + kGb(d)^{-c} \tag{2.5}$$

where k is an adimensional material constant and c = 1. This relationship between flow stress (σ) and substructural size (d) is quite similar in form to the Hall-Petch equation for grain size strengthening given earlier (eqn. (2.1)). Gil Sevillano [6] has suggested that in this respect, the parameter k can be regarded as a measure of the relative "strength" of the substructural barrier which implies that both the spacing and structure of the dislocation walls are important for strengthening considerations. The inverse linear dependence between flow stress and cell size expressed by eqn. (2.5) with c = 1 has been experimentally reported for a variety of metals [44-49,60,83]. Figure 2.6 shows this type of relationship for a number of iron-based alloys compiled by Young and Sherby [83]; data for high angle grain boundaries are also shown.

Considerable controversy regarding the exact value of the exponent "c" in eqn. (2.5) has arisen from the fact that many other experimental data can be represented equally well by the same equation, but with c = 1/2 [30]. Some investigators have suggested that a change in dependence of flow stress on substructure size reflected by a change in the value of "c" may be related to a transition from cell multiplication to subgrain formation at larger strains [6,83,84] as alluded to earlier. The rationale behind this argument is that the

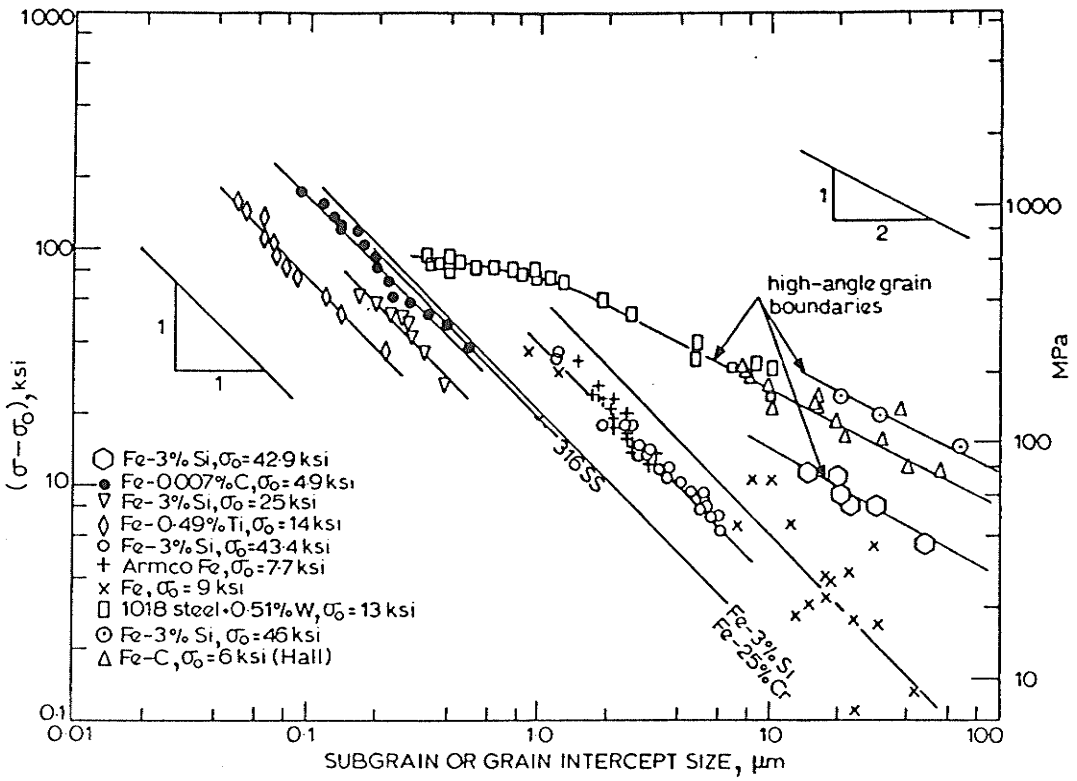

Figure 2.6 Correlation of flow stress with cell size after subtracting a "friction stress", σ_0, determined by extrapolation to infinite cell size on a graph of stress vs inverse cell size (after ref. 83)

increased misorientation and boundary perfection of subgrains give them the characteristic of high angle grains. It would seem that both the character of the substructural boundary and the cell/subgrain size influence the underlying strengthening mechanisms. An extensive survey of the reported values for c and k in eqn. (2.5) has been compiled by Raj and Pharr [85].

The influence of the type of sub-boundary (i.e., cell wall or subgrain wall) has been related to flow stress in terms of the sub-boundary misorientation, Θ, by

$$\sigma = \sigma_o + \frac{K'}{\sqrt{d}}\sqrt{\Theta} \tag{2.6}$$

where K' is a material constant. Such a relationship was demonstrated for cold worked aluminum [86] and wire drawn iron [49].

2.7 Work Hardening Theories

2.7.1 Review of Theoretical Models

Many theories were proposed to account for the substructural influence of dislocations on the work hardening and flow stress behaviour of metals. Most of the theories were originally predicated upon the experimental observations on single crystals, and especially the linear, stage II hardening region, but they generally seem to be applicable to polycrystals as well. All of the theories are based on the notion that the flow stress is controlled by the resistance to propagation of slip in a metal, and all lead to the familiar expression between flow stress and dislocation density given by eqn. (2.3).

Early theories of work hardening assumed that the flow stress is controlled by the "long range" stress field of groups of dislocations, or in other words, internal stresses which affect dislocations at large distances compared with the distance between dislocations within the groups. The original "long range stress theory" by Taylor [82] proposed that the

flow stress was equivalent to the stress required to move a dislocation through a two dimensional array of dislocations against the cumulative internal stress due to the dislocations. The flow stress is then given by

$$\tau - \tau_o = \left(\frac{1}{2\pi}\right) Gb\sqrt{\rho} \tag{2.7}$$

where τ_o is the lattice frictional stress and ρ is the density of dislocations in the array. Seeger [39] considered the long range stresses of piled-up groups of dislocations. In his model, he assumed that dislocations are nucleated at sources and become piled-up at barriers in their glide planes. Typical barriers would include sessile (immobile) dislocations such as Lomer-Cottrell locks, formed by intersections of glide dislocations. As deformation proceeds, the number of barriers and pile-ups increases, so that the flow stress is controlled by the resistance to motion of glide dislocations from the long range stress fields of pile-ups. Assuming that a piled-up group of n dislocations acts as a single dislocation of burgers vector nb, the flow stress is

$$\tau - \tau_o = \left(\frac{1}{2\pi}\right) G(nb)\sqrt{\rho_p} = \left(\frac{1}{2\pi}\right) Gb\sqrt{n}\sqrt{\rho} \tag{2.8}$$

where ρ_p is the density of piled-up groups and ρ is the primary dislocation density $= n\rho_p$. Seeger's model has been criticized for the lack of experimental evidence for pile-ups except in low-strained, low SFE alloys. Also, detailed calculations by Hirsch and Mitchell [24] based on actually observed dislocation arrangements showed that pile-up stresses predicted by the Seeger model account for less than 50% of the total flow stress.

Other models have developed to account for the contribution from secondary or "forest" dislocations intersecting the slip planes of primary dislocations. Basinski [87] considered the flow stress to be determined by the stress required for glide dislocations to

overcome the elastic stress fields of the dislocation forests. In his analysis, the flow stress is largely determined by the forest dislocation density, ρ_f, as

$$\tau - \tau_o = \left(\frac{1}{2\pi}\right) Gb\sqrt{\rho_f} \tag{2.9}$$

Such a relationship generally assumes a uniform distribution of forest dislocations and tends to underestimate the flow stress for metals developing an inhomogeneous dislocation structure. Kocks [43] has considered the internal resistance to dislocation movement in a heterogeneous structure consisting of "hard" and "soft" regions using computer statistical models.

So far, the models discussed primarily consider only the athermal or temperature-independent dislocation contribution to the flow stress. Mott [88], and Hirsch and Warrington [89] also considered the temperature dependent (thermal) part of the flow stress arising from the creation of jogs in screw dislocations cutting through the dislocation forest. They found that the flow stress due to the frictional drag of sessile jogs on moving screw dislocations is expressed as

$$\tau - \tau_o = \alpha Gbn_j \tag{2.10}$$

where $\alpha \cong 1/5$ and n_j is the number of sessile jogs per unit length of dislocation line which is proportional to the density of forest dislocations. Since sessile jogs move by thermally-activated climb and vacancy production, the flow stress given by eqn. (2.10) will be temperature dependent. The various long range stress and forest theories described thus far are schematically shown in Figure 2.7.

The mesh length theory of Kuhlmann-Wilsdorf [32-36] is in many respects quite similar to a forest hardening model, with the important difference that the flow stress is

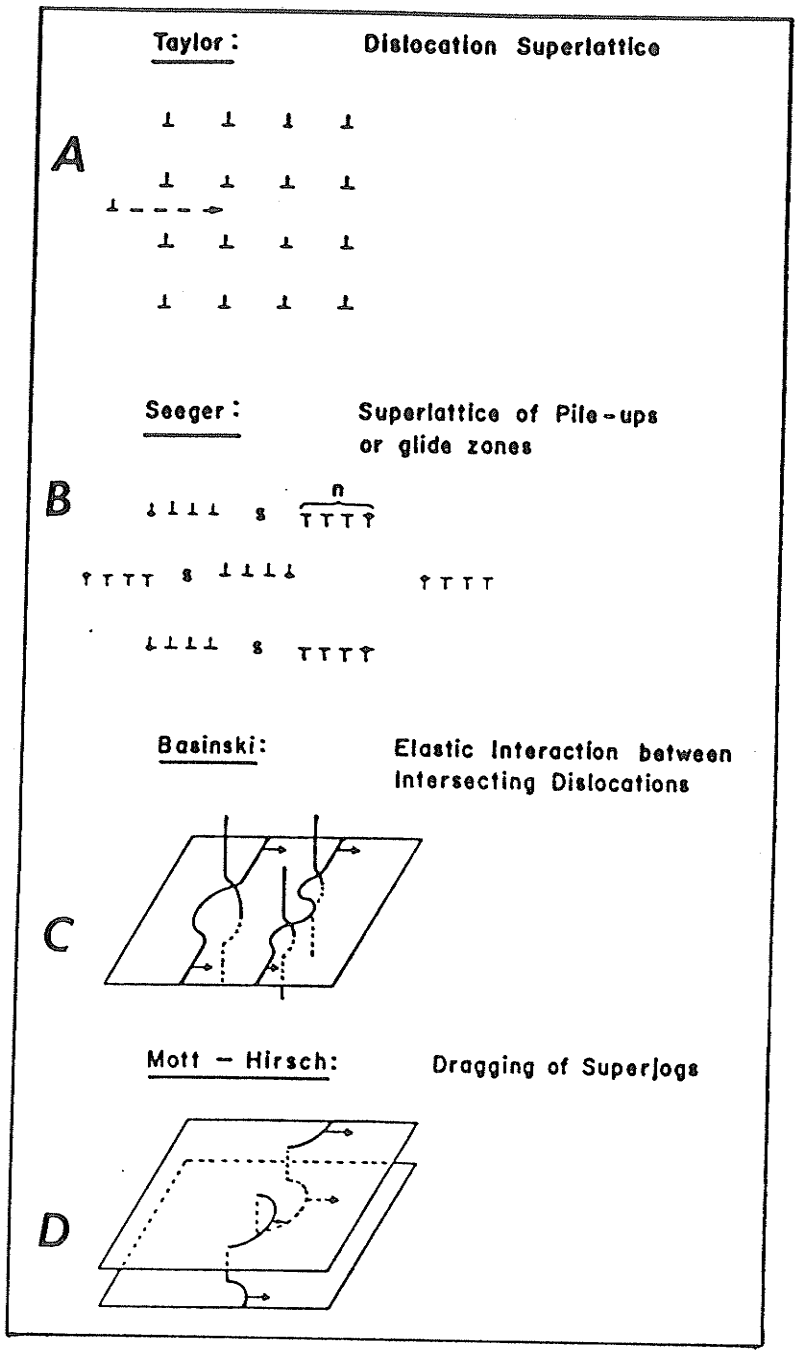

Figure 2.7 Schematic of four work hardening mechanisms: A,B, long range stress models; C,D, forest hardening models (after ref. 90)

assumed to be controlled by the stress required to bow-out dislocation segments pinned by forest dislocations. As the dislocation density increases, the free dislocation link lengths decrease and the flow stress increases. Owing to its relevance to the present study, the mesh length theory of work hardening is considered in greater detail in the next section.

2.7.2 Mesh Length Theory of Work Hardening

The work hardening theory of Kuhlmann-Wilsdorf [32-36] recognizes that the dislocation cell structures observed during the deformation of most metals must occur in response to a lowering of free energy. The total elastic strain energy, U_D, for a given density ρ of dislocations arranged in a tangled array can be written as [91]

$$U_D = \rho \frac{Gb^2}{4\pi} f(\nu) \ln\left(\frac{R}{r_o}\right) \tag{2.11}$$

where G is the shear modulus, b is the burgers vector, R is approximately equal to the average spacing of dislocations in the array, and $f(\nu)$ is a function of Poisson's ratio ν, equal to $1/(1-\nu)$ for edge dislocations and 1 for screw dislocations. The constant r_o is equal to the core radius of dislocations and is usually taken = b. Kuhlmann-Wilsdorf proposed that dislocations in a tangled substructure decrease their total strain energy by reducing their spacing (R) and "screening" one-another's stress fields. This is known as the "energy minimization principle". Thus, a lowering of strain energy and reduction in long range stresses becomes the driving force for the formation of low energy dislocation structures (LEDS) typified by dislocation cells.

According to the mesh length theory, work hardening arises from the stress required to super-critically bow-out free dislocation link lengths in the cell walls in the manner of a Frank-Read source. This mechanism is shown schematically in Figure 2.8, where expanding dislocation links propagate slip from one cell to the next. Such a cell

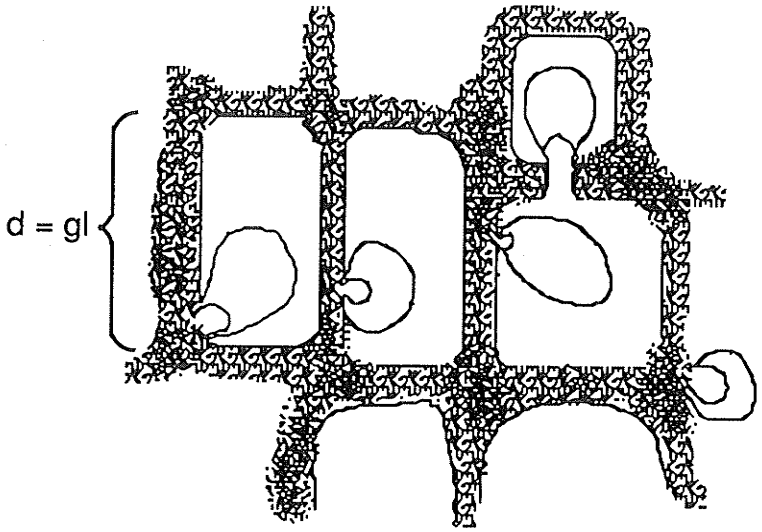

Figure 2.8 Propagation of slip through dislocation cell structure by the bowing-out of the longest dislocation links (after ref. 36)

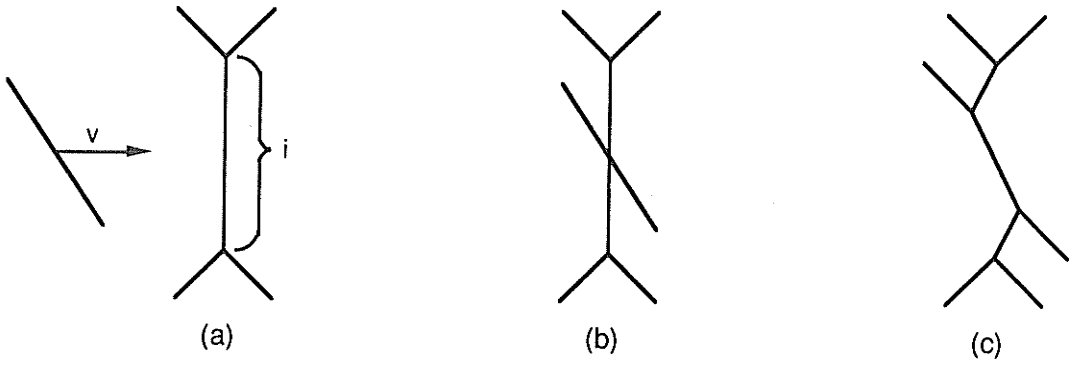

Figure 2.9 Subdivision of dislocation links through reactions with glide dislocations in cell walls (after ref. 36)

wall-source mechanism is experimentally supported by TEM observations of strained nickel [92]. As the dislocation density increases due to dislocation multiplication during straining, the free link length decreases and the flow stress required to activate the links increases, producing work hardening. Kuhlmann-Wilsdorf [33] has related the average free dislocation link length, $\overline{\ell}$, in cell walls to the total dislocation density by

$$(\overline{\ell})^2 = \frac{fm}{\rho} \tag{2.12}$$

where f is the volume fraction occupied by cell walls and m is a geometrical parameter relating the average link length to the dislocation density. Experimentally, f is found to be ~1/5 and m is estimated to be ~5 for dislocation arrangements in FCC metals [33]. Thus, the quantity mf is approximately equal to unity.

Kuhlmann-Wilsdorf has further supposed that longer link lengths than the average length are subdivided through reactions with glide dislocations in cell walls. This is depicted in Figure 2.9. Such subdivisions will on average, generate three links from one with length of about 1/3 the original length, as shown in the figure. Therefore, it is expected that the longest free dislocation link lengths, ℓ_s, which are the easiest (lowest stress) to activate are related to the average length by

$$\ell_s = n\overline{\ell} \cong 3\overline{\ell} \tag{2.13}$$

Direct measurements of link lengths by Kuhlmann-Wilsdorf [93] on TEM micrographs by Langford and Cohen [48] for drawn Fe wire determined a ratio of $\ell_s/\overline{\ell}$ = 3.3, which supports the above relationship.

The shear stress required to activate a dislocation source of length ℓ_s is given by

$$\tau_s = \frac{Gb}{2\pi\ell_s}\ln\left(\frac{\ell_s}{b}\right) \tag{2.14}$$

Combining eqn's. (2.12), (2.13), and (2.14) yields

$$\tau_s = \tau - \tau_o = \frac{Gb\sqrt{\rho}}{2\pi n\sqrt{mf}}\ln\left(\frac{n\sqrt{mf}}{b\sqrt{\rho}}\right) \tag{2.15}$$

This equation is similar to the expression between shear stress and dislocation density (eqn. (2.3)) given earlier. Assuming the parameters $n \cong 3$ and $mf \cong 1$, eqn. (2.15) can be rewritten as

$$\tau - \tau_o \cong \frac{Gb\sqrt{\rho}}{6\pi}\ln\left(\frac{3}{b\sqrt{\rho}}\right) = \alpha Gb\sqrt{\rho} \tag{2.16}$$

where α is predicted to be $\cong 0.5$, in good agreement with experimentally determined values [33].

Another important aspect of the mesh length theory of work hardening is the concept of "similitude"; namely that the size of the dislocation cell pattern decreases in proportion to the applied stress. This arises from the maintenance of equilibrium between the internal stresses due to the dislocations in the cell walls and the externally applied shear stress acting on them. Further, the cell configuration remains geometrically similar to itself as it shrinks with increasing stress, thus maintaining "similitude". Kuhlmann-Wilsdorf [33] predicted that the free dislocation link length, $\overline{\ell}$, should decrease proportionally with the cell size, d, as long as similitude prevails, i.e.,

$$\overline{\ell} = \frac{d}{g} \tag{2.17}$$

where g is a constant which varies considerably, depending on the material. Measurements of g for copper single crystals [33] and drawn Fe wire [93] gave values of 200 and 14, respectively. Kuhlmann-Wilsdorf has theorized that similitude breaks down when cell size changes become small, signaling the onset of a diminishing work hardening rate in stage III [33,34]. A series of investigations by Bassim and co-workers [45,47,94,95] have qualitatively verified the principle of similitude in copper and low alloy steel, and the attainment of a limiting cell size at the onset of stage III behaviour.

Combining eqns. (2.12) and (2.17) gives

$$d = \frac{g\sqrt{fm}}{\sqrt{\rho}} \cong \frac{g}{\sqrt{\rho}} \tag{2.18}$$

and substituting eqn. (2.18) into eqn. (2.16) produces

$$\tau - \tau_o = \alpha g G b (d)^{-1} \tag{2.19a}$$

or

$$\sigma - \sigma_o = M\alpha g G b (d)^{-1} = k G b (d)^{-1} \tag{2.19b}$$

where M is an orientation factor ($\cong 3$) and k is a material constant. This is the familiar relationship between flow stress and inverse cell size given by eqn. (2.5) and experimentally observed for a number of metals as mentioned earlier.

The mesh length theory of Kuhlmann-Wilsdorf has been criticized for containing too many unpredictable parameters (i.e., n,m,f, etc.) and for not accounting for dynamic recovery mechanisms in stage III [6,7]. However, it seems that the theory is in both qualitative and quantitative agreement with many of the features of substructural evolution experimentally observed. Later in this study, the validity of the theory for describing the behaviour of a complex steel alloy is presented.

2.8 Microstructural Aspects of Ductile Fracture

During the process of plastic deformation, localized strain at microstructural heterogeneities in the material leads to high, internal stresses. This causes the nucleation of voids or cavities at the microstructural sites, which grow and coalesce by localized plastic deformation leading to ductile fracture. Materials fracturing in this way exhibit fibrous fracture surfaces characterized by the presence of many "cuplets" or "dimples" when observed at high magnification.

The sites of localized plastic deformation where void nucleation takes place are typically associated with second phase particles and inclusions, as found in Al alloys by Broek [96], for example. It has been determined that voids initiate by either the fracturing of individual particles under localized stress, or by the decohesion of the particle-matrix interface. The onset of void initiation at the particle-matrix interface has been considered on the basis of various criteria, including the critical nucleation strain model of Goods and Brown [97], the critical interfacial stress model of Argon et. al. [98], and the energy criterion model of Fisher and Gurland [99].

Other investigators have modelled the processes controlling void growth and coalescence. Gurland and Plateau [100] considered the growth of voids by the necking of the ligaments between void-forming particles under the influence of triaxial stress. McClintock et. al. [101] theoretically related the growth of cylindrical voids by considering the strain distribution around the voids using continuum mechanics. Wilkinson and Vitek [102] have modelled the process of stable crack growth in ductile metals in terms of the nucleation and growth of voids in the crack tip stress field. Wilsdorf [103] has recently reviewed the various models of void initiation and growth, as well as a number of other microstructural aspects of ductile fracture.

Although the vast majority of ductile fracture studies have been microscopically correlated with void mechanisms at particles and inclusions, a number of studies have

shown that the presence of particles is not a prerequisite for void nucleation. For example, in metals with a low particle content, void nucleation has been observed at grain boundaries and grain boundary triple points [104]. Bauer and Wilsdorf [105] suggested that small voids could be initiated at vacancy clusters in AISI 304 stainless steel, based on the evidence of a measured void density 100 times larger than the average particle density. A series of investigations by Wilsdorf and co-workers [106-109] were the first to consider the role of well-developed dislocation structures in the process of crack propagation in ductile materials. They observed microcrack initiation and propagation along dislocation cell walls during in-situ HVEM (High Voltage Electron Microscopy) straining experiments of a number of pure metals. Wilsdorf has suggested that the local strain energy associated with the cell walls makes them energetically favourable as sites for void initiation in the absence of particles [106]. Amouzouvi and Bassim [110] have considered the ductile fracture process in terms of the energetics of crack tip blunting by dislocations. They found that the macroscopic fracture toughness of a low alloy steel was dependent on the density of mobile dislocations in the plastically-deformed region ahead of the crack tip. Bassim [111] extended this work to account for crack propagation in material containing well-developed dislocation cells.

These studies clearly show the importance of inhomogeneous dislocation arrangements, and in particular, cell structures, in the process of microcrack initiation and propagation which underlies the macroscopic fracture behaviour of ductile metals. The present study further investigates the strengthening mechanisms and fracture processes connected with the evolution of dislocation substructure during the plastic deformation of a ductile material.

Chapter III

EXPERIMENTAL PROCEDURE

This section outlines the materials, preparations, and testing methods utilized in the experimental portion of this study.

3.1 Materials and Heat Treatment

The material used in this investigation was a deep-hardening, low alloy steel designated "SPS" by the supplier (Atlas Alloys Co.). The chemical composition of the alloy steel closely conforms with that of AISI 4340 and is given in Table 3.1.

The material was received in the form of rolled bar stock of 25 mm x 64 mm cross section. The steel is characterized by a microstructure of mostly lamellar pearlite in a proeutectiod ferrite matrix and a high degree of "cleanliness", or a low inclusion content. The microstructure and inclusion distribution in the longitudinal, transverse, and through-thickness directions with respect to the axis of rolling of the bar are indicated in typical micrographs shown in Figures 3.1(a) and 3.1(b), respectively. A slight degree of banding of pearlite and ferrite into layers is evident in Fig. 3.1(a) due to the presence of Mn which causes segregation of C during solidification of steel [3]. Also noticeable is the elongation of inclusions along the rolling direction in Fig. 3.1(b).

Three different heat treatments schedules were performed in order to produce a variation in the initial proeutectoid ferrite grain size. The as-received bar was cut into smaller pieces of about 10 cm long and packed in carbon (graphite) to prevent decarburization during annealing. The three annealing schedules (referred to as A, D, and E) consisted of austenitization at different temperatures to vary the prior austenite grain size (and transformed ferrite grain size), followed by furnace cooling. The details of the annealing schedules are provided in Table 3.2. The last heat treatment included an

Table 3.1 : Chemical Composition of 4340 Steel

Element	C	Mn	Mo	Cr	Ni	P	S	Fe
Wt. %	0.40	0.75	0.15	0.60	1.25	0.02	0.02	balance

Table 3.2 : Heat Treatment Schedules of Sample Groups of 4340 Steel

Schedule	Temperature	Time	Cooling Treatment
A	840° C	1 hr	furnace cool to room temp
D	900° C	1 hr	furnace cool to room temp
E	a) 1100° C	1 hr	* cool to 670° C
	b) 670° C	1 hr	furnace cool to room temp

* cooling by rapid transfer to second furnace at 670° C

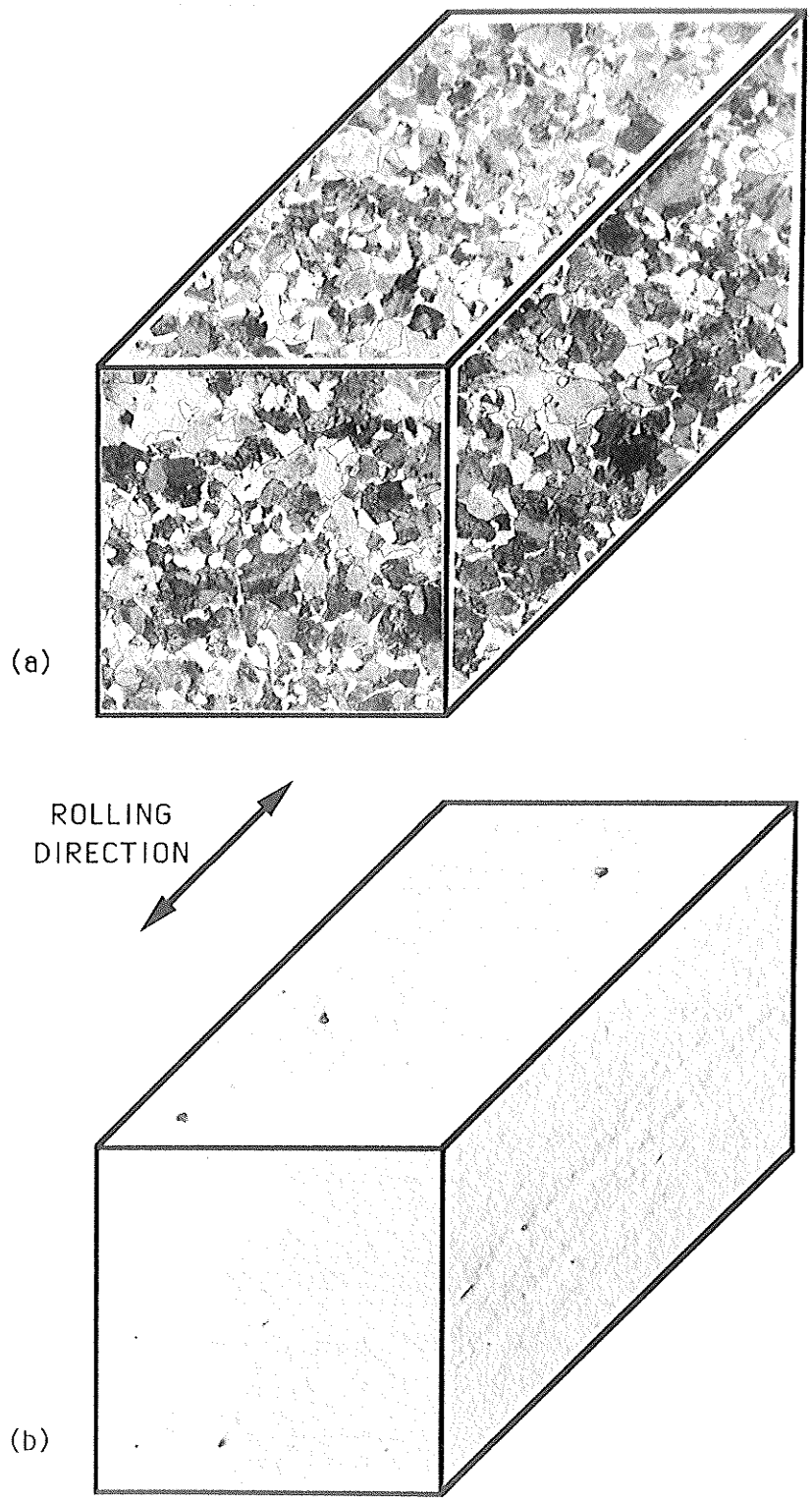

Figure 3.1 Microstructure of 4340 low alloy steel in three orientations relative to the direction of rolling;
(a) etched phases, 200x
(b) unetched inclusion content, 50x

additional isothermal treatment below the austenite phase region to promote further growth of ferrite grains.

3.2 Specimen Preparation

Specimens were prepared from the three annealed steel pieces corresponding to the three different initial ferrite grain sizes, hereafter referred to as samples "A", "D", and "E". Different specimen types were required for mechanical properties evaluation by tensile and microhardness testing, as well as for microstructural examination using optical, scanning electron, and transmission electron microscopy. All specimens were preserved in a moisture-free desiccator to prevent oxidation or contamination prior to testing.

3.2.1 Tensile Specimens

Tensile specimens were prepared from roughly square blanks cut along the longitudinal, or rolling direction from each metal group as shown in Figure 3.2. The specimens were of the cylindrical type as illustrated in Figure 3.3 and were machined to dimensions of 25.40 mm (1.0") gauge length and 6.35 mm (0.25") gauge diameter in accordance with ASTM Standard E8-86 [112].

All further specimens were obtained from sections cut from broken tensile specimens after testing. The sectioning of a tensile specimen to provide the various other specimens is illustrated in Figure 3.4.

3.2.2 Microhardness Specimens

A single broken tensile half was cut at the gauge mark (to provide a reference point) and then split longitudinally into two new halves using a BEUHLER Isomet slow-speed diamond saw. This procedure provided a flat, longitudinal section of varying transverse dimension as shown in Figure 3.4(a). This section was then mounted in bakelite and polished to 1μm surface roughness for microhardness testing. The advantage of this

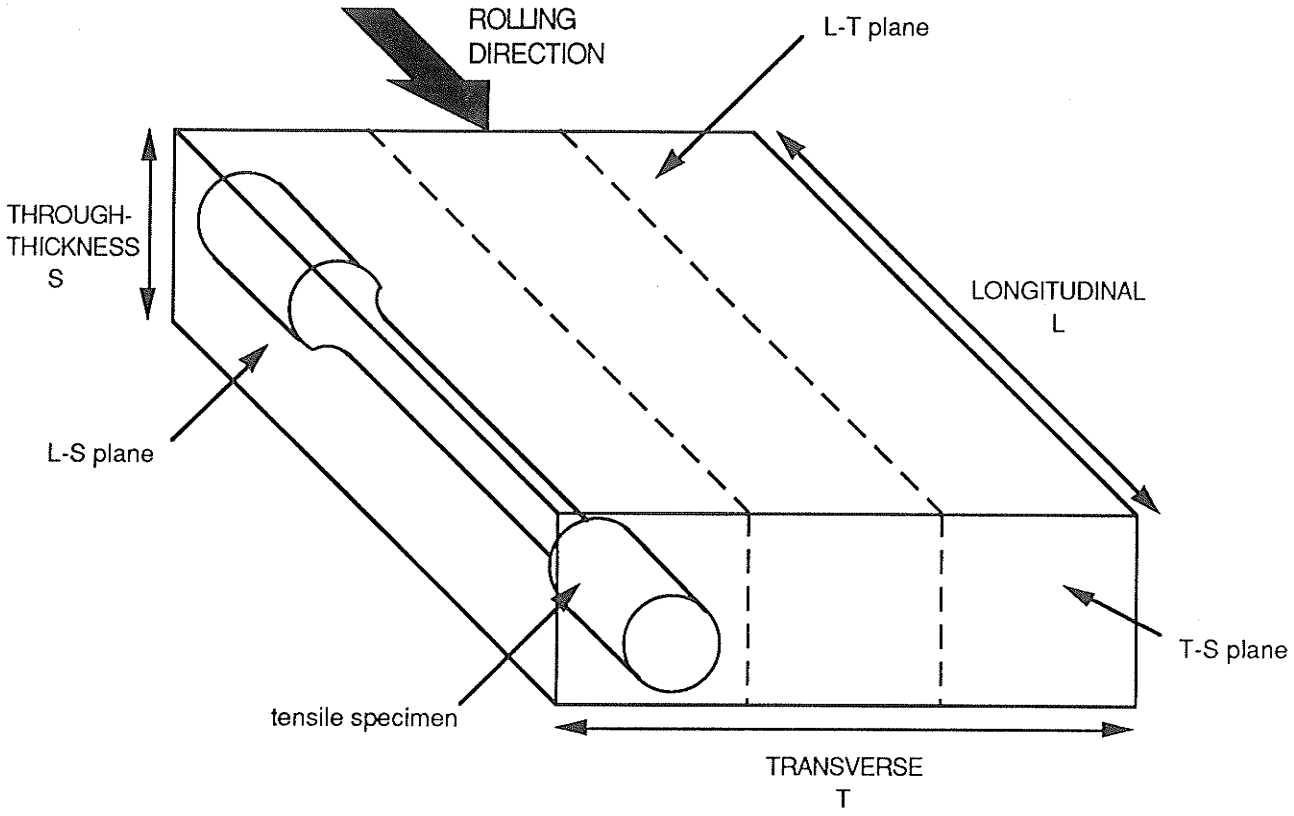

Figure 3.2 Orientation of tensile specimen relative to as-received bar

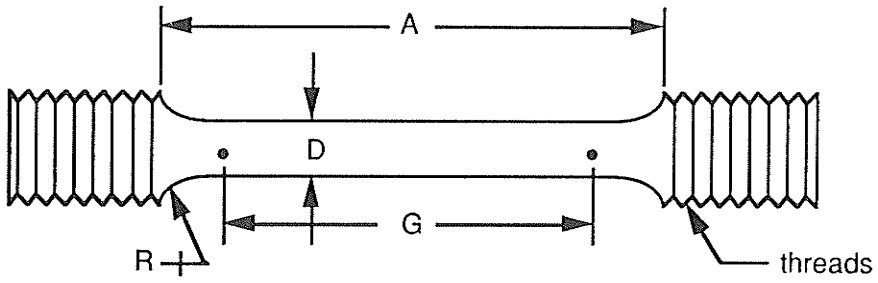

A = 32 mm
G = 25.4 +/- 0.10 mm
D = 6.35 +/- 0.12 mm
R = 5.0 mm
Threads = 11 mm UNF

Figure 3.3 Dimensions of Cylindrical Tensile Specimen

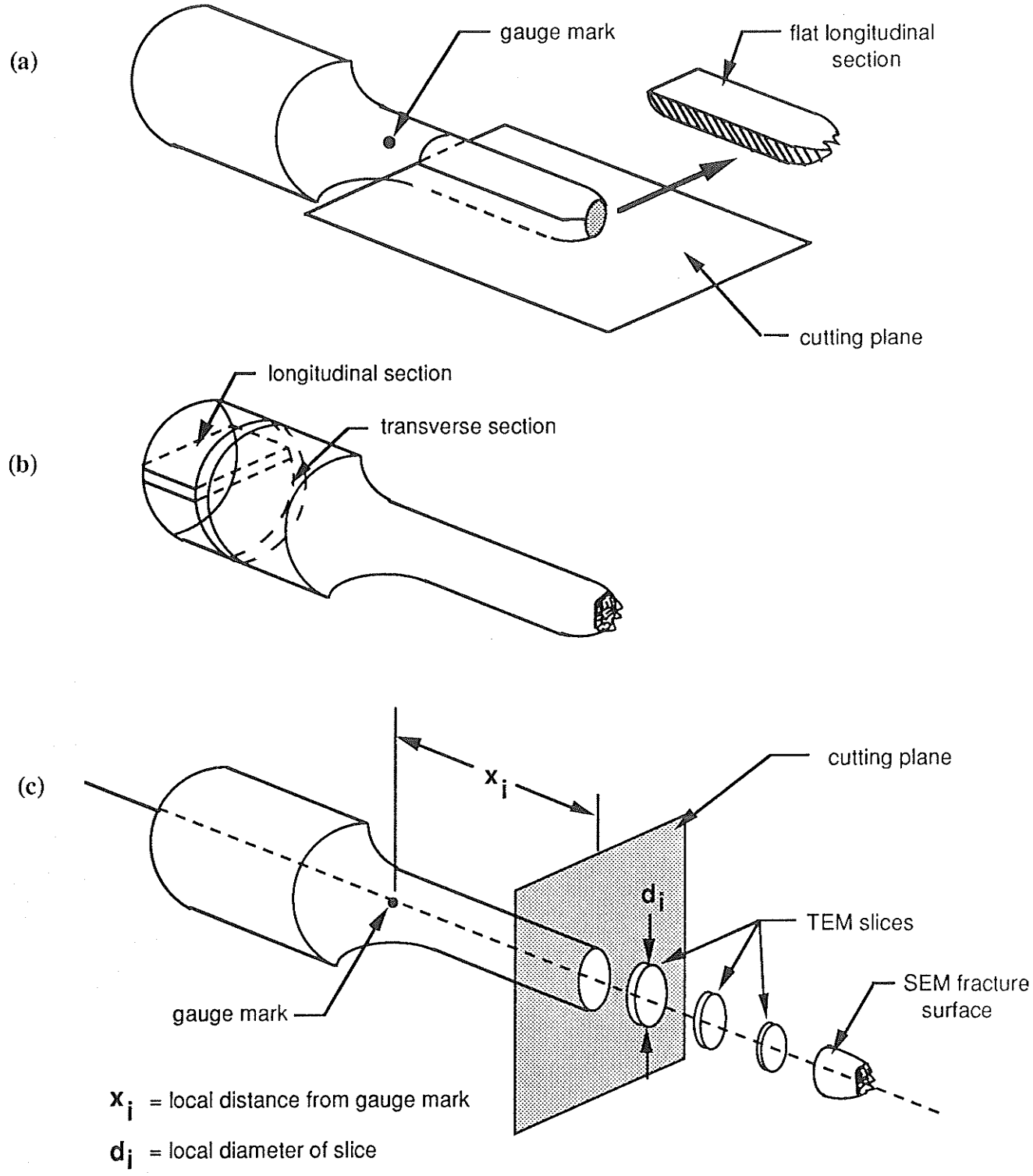

Figure 3.4 Specimen types sectioned from tensile halves;
a) microhardness specimen
b) optical microscopy specimens
c) TEM and SEM specimens

sectioning method was that the varying degrees of plastic deformation experienced by a tensile specimen could be evaluated by microhardness measurement with only a single specimen required.

3.2.3 Optical Metallography Specimens

Transverse and longitudinal sections were cut from the ends of undeformed tensile specimens from each metal group as illustrated in Figure 3.4(b). The sections were then mounted in bakelite and polished mechanically using SiC papers and AlO_2 powders to a final surface roughness of about 0.5 μm. Both unetched and etched samples were prepared for metallographic examination, with etching performed using a solution of 2% Nital (2 parts nitric acid in 98 parts methanol).

3.2.4 SEM Specimens

The fractured ends of broken tensile halves were cut using a slow-speed diamond saw as shown in Figure 3.4(c). The fracture surfaces were then washed ultrasonically and rinsed in methanol to remove any cutting fluid or oxide buildup. The specimens were next mounted on aluminum disc holders using a colloidal graphite paint, and stored in a desiccator to await examination in the SEM.

3.2.5 TEM Specimens

Specimens for transmission electron microscopy (TEM) were prepared from transverse sections cut normal to the longitudinal gauge length of tensile halves from each metal group. As depicted in Figure 3.4(c), slices of approximately constant diameter and initial thickness = 0.30 mm were removed from various locations along the gauge length using a slow-speed diamond saw. The distance from the gauge point (x_i), local diameter (d_i), and approximate local strain (expressed as either % reduction in area or % strain) were recorded for each slice. The advantage of this sectioning technique (first used by

Klassen [113]) lies in the fact that specimens with varying degrees of plastic strain can be obtained from a single tensile specimen, maximizing the use of material. On the other hand, fewer specimens of a given fixed degree of plastic strain are available which necessitates a high success rate in thin foil production.

The slices were mechanicallly thinned to a thickness of about 0.1 mm using 600 grit SiC paper. Discs of 3 mm diameter were removed from the thinned slices using electrical spark erosion machining to prevent any disturbance to the deformation structure contained within the material. These discs were lightly polished to remove any oxide layer and then electro-polished until perforation using a STRUERS Tenupol jet electro-polishing unit. The electro-polishing conditions were as follows:

Electrolyte:	5% perchloric acid ($HClO_4$) in 95% methanol
Voltage:	18 volts
Current:	80-100 mA
Temperature:	-50^{o} to -55^{o} C

Electro-polished foils were washed first in methanol, then in ethanol, and stored in an air-tight desiccator. TEM examination was usually carried out shortly after preparation of thin foils to avoid any undue contamination.

3.3 Mechanical Testing

Mechanical testing was carried out in order to characterize the tensile properties and flow curve behaviour of the three heat-treated groups of 4340 alloy. This was achieved through tensile and microhardenss tests.

3.3.1 Tensile Testing

Tensile tests were performed on 3 cylindrical specimens per steel group A, D, and E using an Instron model 1137 screw-driven testing machine interfaced to a computer-based data acquisition and analysis system. All nine tests were conducted in air at room temperature with a constant displacement rate of 0.5 mm/min, corresponding to an initial strain rate of 3.3×10^{-4} sec^{-1}. Load cell and extensometer readings were digitally sampled at a sampling rate of 2 per second.

Engineering stress-strain curves to fracture were automatically generated from the raw data collected during tensile tests of the three steel groups. However, it was necessary to convert the curves to true stress - true strain values, since the engineering curves do not account for the changing dimensions of the testpiece during deformation and therefore do not provide an accurate description of the flow process. The construction of the flow curves involved a number of steps.

The first step was to convert the engineering stress-strain (s-e) data to true stress-true strain (σ-ε) values using the following equations [2];

$$\sigma = s(1 + e) \tag{3.1}$$

$$\varepsilon = \ln(1 + e) \tag{3.2}$$

which are valid up to maximum load, or the point of tensile instability.

Next, the σ–ε data to maximum load was approximated by the well-known power law expression of the form

$$\sigma = K\varepsilon^n \tag{3.3}$$

where n and K are the constants in the equation of a straight line fitted through the points in a plot of log σ vs log ε. This expression was used to extrapolate the flow curves

to the point of fracture, with the true strain, ε, determined from the actual diameter of the necked specimen using

$$\varepsilon = 2\ln\left(\frac{d_o}{d_i}\right) \tag{3.4}$$

with d_o and d_i the initial and instantaneous diameters of the specimen, respectively.

Due to the triaxial stress state introduced by necking, the average longitudinal stress measured during a tensile test is greater than the stress required to maintain flow if simple tension was maintained. A mathematical analysis by Bridgman [114] corrects the average tensile stress based on the geometry of the neck, which can be related to the corresponding true strain. The empirical relation between the stress correction factor (σ/σ_{avg}) and the true strain in the neck is shown in Fig. 3.5. This relation has been shown to give close agreement with the actual stress in steel specimens [115], and was applied as a necking correction for eqn. (3.3) in the present work.

From the approximated flow curves, standard tensile flow properties such as the yield and ultimate stresses were determined for each steel group. All tensile testing and analysis was conducted according to the methods outlined in ASTM Standard E8-86 [112].

3.3.2 Microhardness Testing

Microhardness tests were performed as an alternative means of determining the flow curve characteristics of 4340 alloy up to fracture for comparison with the power law flow curve approximation used in tension testing. The use of hardness tests for evaluating flow properties in tension/compresssion has been discussed by Tabor [116]. Microhardness tests were conducted on a longitudinal section of a broken tensile specimen from sample group A sectioned in the manner described in section 3.2.2. Prior to sectioning however, a profile of the diameter of the piece from the gauge point to the

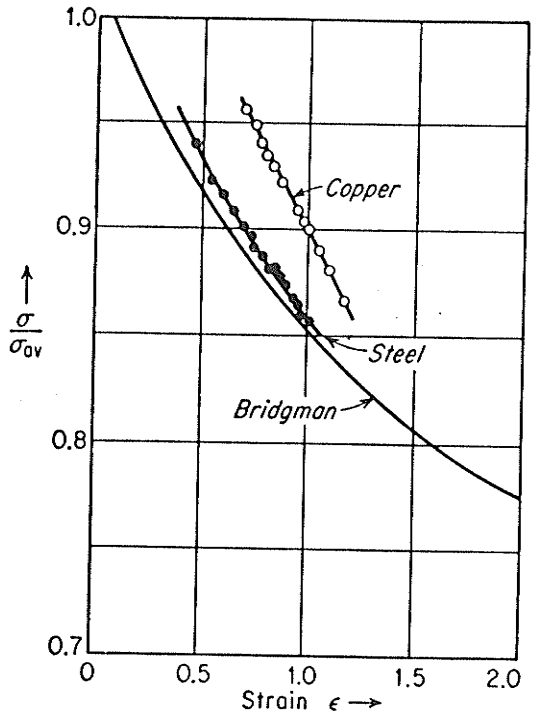

Figure 3.5 Relationship between Bridgman correction factor (σ/σ_{avg}) and true tensile strain (ε) (after ref. 115)

fracture surface was obtained by manual measurement of the diameter at fixed increments along the gauge length using a transmitted light optical microscope fitted with a calibrated stage. From the variation in diameter with distance from the gauge point, the variation in plastic strain with distance could also be determined. This information enabled the construction of a "microhardness flow curve" where the microhardness reading was matched with the plastic strain at the same distance from the gauge point at which the reading was made.

Vickers hardness or diamond-pyramid hardness (DPH) profile measurements were performed on the polished tensile section using a Leitz Wetzlar Miniload tester operating at a magnification of 400x. Indentations were made with a 300 g load applied for 10 seconds, with an average of 6 measurements recorded at each increment along the gauge length.

3.4 Microstructural Examination

Microstructural characterization of the three groups of low alloy steel was carried out using the tools of optical, scanning electron, and transmission electron microscopy.

3.4.1 Optical Microscopy

Optical microscopy was performed to determine the distribution and morphology of phases and inclusions present in each of the three steel groups. Specifically, the size and distribution of inclusions were measured on unetched samples, and the volume fractions of ferrite and pearlite and the sizes of the proeutectoid ferrite grains produced by the three heat treatment schedules were measured on specimens etched in 2% Nital. The microstructure of transverse sections was of primary interest in this study, although longitudinal sections were also examined for the sake of completeness. All metallographic sections were prepared as stated in section 3.2.3 and examined under reflected light at objective magnifications from 50x to 1000x using a Nikon Epiphot optical microscope equipped with

a 35 mm camera. Polarized light was sometimes exploited to enhance the image comtrast when studying inclusions. Image analysis was performed on etched and unetched specimens using standard quantitative metallographic techniques which are outlined in section 3.5.

3.4.2 Scanning Electron Microscopy

Scanning electron microscopy (SEM) was used for high resolution observation of the surface topography of the tensile fracture surfaces in each of the three metal groups. The fracture surfaces were prepared as described in section 3.2.4 and examined with a JEOL JXA-840 scanning microanalyser operating at 25 kV. Micrographs of random areas containing voids or "dimples" were obtained at 4000x magnification for quantitative measurement as will be discussed in section 3.5. Areas on the surfaces exhibiting inclusions or other "unusual" features were also photographed.

3.4.3 Transmission Electron Microscopy

Transmission electron microscopy (TEM) of thin foils prepared from annealed and tensile-strained specimens was performed on a JEOL 2000FX STEM microscope operating at 200 kV accelerating potential. The main objective of this work was to study the formation and evolution of dislocation cell structures with plastic strain and the role of microstructural elements in that process for each of the three groups of 4340 steel. Bright field TEM micrographs of dislocation cell structures were taken at magnifications in the range of 15,000x to 30,000x for later measuremment. To ensure a proper two-dimensional representation of the three-dimensional cell patterns, goniometer stage tilting and selected area diffraction patterns were employed to determine the optimum conditions for diffraction contrast of dislocations in the cells.

Regions in the thin foils containing pearlite were also photographed, primarily for determination of the mean interlamellar spacing. The methods for quantitative measurement of dislocation cell size and pearlite interlamellar spacing are presented in the next section.

3.5 Quantitative Metallography

Quantitative metallography was used to numerically describe the microstructural features observed by optical microscopy, SEM, and TEM, as discussed in the previous sections. All image analysis was performed using a LEITZ/TASIC automated image analyser interfaced to a DEC (PDP-11) computer. Custom software programs were employed to measure specific parameters and their statistical distributions, and to record the results in tabular or graphical form. The programs adopted standard quantitative metallographic techniques as described in Vanderdoort's "Metallography: Principles and Practice" [117] and elsewhere. Where possible, image analysis was performed directly on the metallographic specimen of interest, or else on images traced onto clear plastic (acetate) slides from photo micrograph originals.

3.5.1 Inclusion Size and Distribution

Analysis of the volume fraction, size, and spacing of non-metallic inclusions was carried out at 520x magnification on polished, unetched transverse sections prepared from each of the metals groups of the low-alloy steel. The volume fraction of inclusions was found using a two-dimensional systematic point counting method as described by Hilliard and Cahn [118]. In this procedure, all inclusions intercepted by a 576 point grid (24x24 points) were counted and summed over 60 different regions of a bulk sample from each of the groups A,D, and E. The volume fraction of inclusions was then calculated using the formula

$$V_i = \frac{\Sigma P_i}{n P_o} \tag{3.5}$$

where V_i = vol. fraction of inclusions

ΣP_i = sum of points intersecting inclusions

P_o = number of grid points per field

n = number of measured fields

The size of inclusions intersected by the point-grid was determined by mean chord length measurements. This parameter is determined from the average of the inclusion lengths projected at 0°, 120°, and 240° to a horizontal line, as depicted in Figure 3.6. This method is not sensitive to variations in particle shape.

A measure of the spacing between inclusions was determined by calculating the mean free path (λ_i), or distance between surfaces of random particles from the size and volume fraction measurements. According to Corti et. al. [119], the mean free path for a random distribution of particles is given by

$$\lambda_i = L_i(V_i^{-1} - 1) \tag{3.6}$$

where λ_i = mean free path

L_i = mean partice size

V_i = volume fraction of particles

This calculation was made to determine any variation in particle spacings amongst the three metal groups.

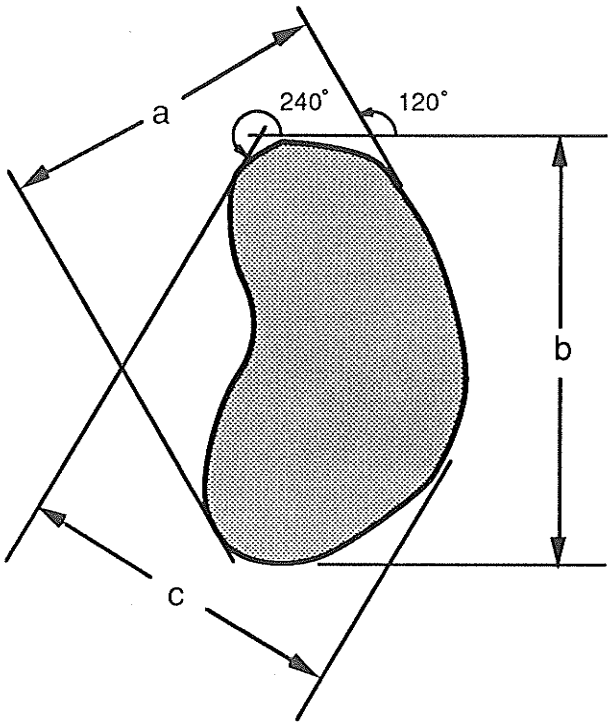

$$MCL = \frac{a + b + c}{3}$$

Figure 3.6 Determination of the mean chord length (MCL) parameter

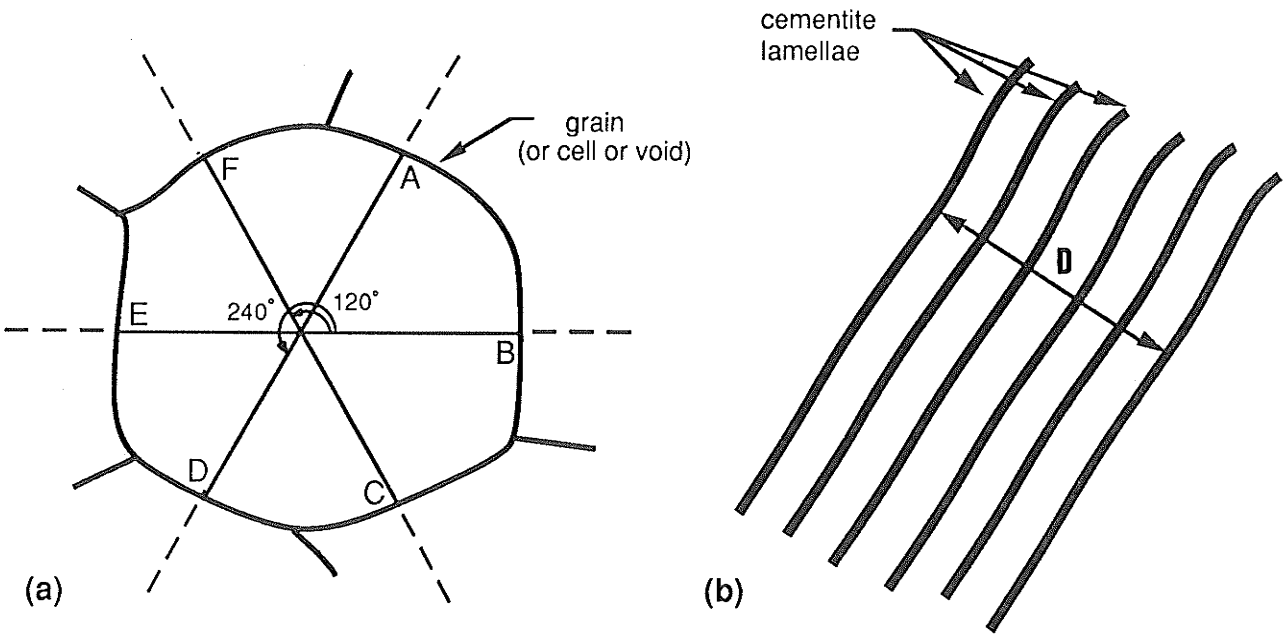

$$size = \frac{\overline{AD}+\overline{BE}+\overline{CF}}{3}$$

$$spacing = \frac{D}{NM}$$

Figure 3.7 a) Linear intercept method used to determine ferrite grain size (or cell or void size)
b) Directed spacing method used to determine pearlite spacing

3.5.2 Volume Fractions of Ferrite and Pearlite

The volume fractions of the two major microstructural constituents, ferrite and pearlite, were determined by systematic point counting similar to the method used for measurement of inclusion volume fraction. About 500 to 600 sample points were counted from polished and etched samples from each group, viewed at 1000x magnification.

3.5.3 Proeutectoid Ferrite Grain Size

In order to verify the effect of the different heat treatment schedules, the mean, initial proeutectoid ferrite grain size was determined on etched, transverse sections prepared according to section 3.2.3 for each of the metal groups. An additional etching treatment in 4% Picral (4 g picric acid in 100 ml ethanol) was used to uniformly darken the pearlite to give better image contrast. The planar ferrite grain size was determined using a mean linear intercept method [117] over 20 randomly selected areas examined at 1000x magnification. The mean intercept length is found by taking the average of lines intersecting ferrite grains at angles of 0°, 120°, and 240°, as depicted in Figure 3.7(a). The mean size and statistical distribution of sizes were calculated by computer.

It should be noted that various relationships between the planar grain intercept length and the volumetric grain diameter have been proposed for particular grain shapes [120]. However, no attempt at such a conversion has been made here due to the nature of the varying ferrite grain shape, thus all further references to grain size are in terms of the mean intercept length. Also, all additional size measurements were made using a similar intercept method for ease of comparison.

3.5.4 Pearlite Interlamellar Spacing

The mean pearlite interlamellar spacing was determined from an average of manual measurements made directly on about 25-30 micrographs obtained from TEM examination.

Approximately 2-3 measurements were performed on each pearlite colony using a mean directed spacing method [117], shown in Figure 3.7(b). The spacing is found as :

$$S_m = \frac{D}{NM} \tag{3.7}$$

where S_m = mean directed spacing

D = perpendicular distance from centre to centre of cementite layers

N = number of lamellae intersected

M = magnification

The mean pearlite interlamellar spacing and distribution of spacings was determined in each of the 3 metal groups investigated.

3.5.5 Dislocation Cell Size

Measurement of dislocation cell size was carried out on photomicrograph images traced by hand onto clear acetate slides. Approximately 50-150 cells were measured at 20,000x magnification to determine the cell size distribution at a given degree of plastic strain (expressed as either % RA or % ε). This measurement was repeated for cells formed at different amounts of plastic strain in order to find the variation in cell size against strain for each of the sample groups A, D, and E. A random, linear intercept method, as illustrated for grain size determination in Figure 3.7(a) was used for the measurement of cell sizes.

3.5.6 Void Size Measurement

The average size and distribution of voids or "dimples" was determined from SEM micrographs of the tensile fracture surfaces traced onto clear acetate for image analysis. A

number of micrographs taken at 4000x magnification from randomly selected areas on the specimen were used to get a representative sampling of dimples sizes in each metal group. The linear intercept method used for grain size and cell size measurement and shown in Figure 3.7(a) was employed for the void size analysis.

Chapter IV

EXPERIMENTAL RESULTS

4.1 Microstructural Examination

This section outlines the results of the optical microscopy examination of the three material groups. This investigation was undertaken to characterize, both qualitatively and quantitatively, the effect of the different heat treatment schedules on certain microstructural parameters, including specifically the proeutectoid ferrite grain size. The subsequent influence of these parameters on the process of work hardening and substructure evolution in the three metal groups will be discussed in later sections.

4.1.1 Effect of Heat Treatments on Morphology of Phases

Typical micrographs taken from transverse sections with respect to the rolling direction are illustrated in Figure 4.1(a-c) for steels A, D, and E, respectively. These micrographs show the etched microstructure consisting of a fairly uniform distribution of eutectoid pearlite within a proeutectoid ferrite matrix. Analysis of the distribution of these constituents found the volume fraction occupied by proeutectoid ferrite to be about 40%, with the remainder being pearlite in all three materials.

The proeutectoid ferrite grains depicted in Fig. 4.1 exhibit a wide distribution of sizes and shapes deviating from an equiaxed morphology. However, there is a noticeable coarsening of the ferrite grains in steel E compared with steel A as a result of the different heat treatment schedules. This observation was confirmed by an analysis of the ferrite grain sizes using mean intercept length measurements. The results shown in Figure 4.2(a-c) give the distributions of grain sizes for each steel group. The mean (planar) grain intercept sizes determined from each histogram increase in the order 3.8, 6.1, and 10.8 micrometers for steels A, D, and E, respectively.

a)

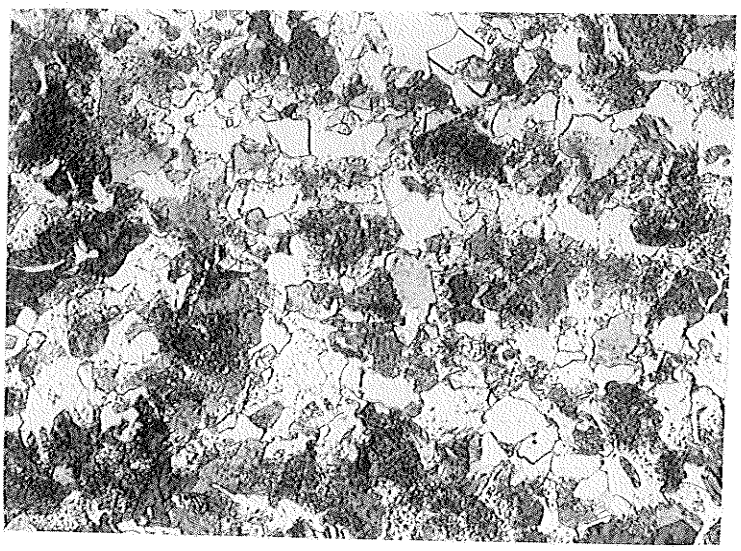

b)

c)

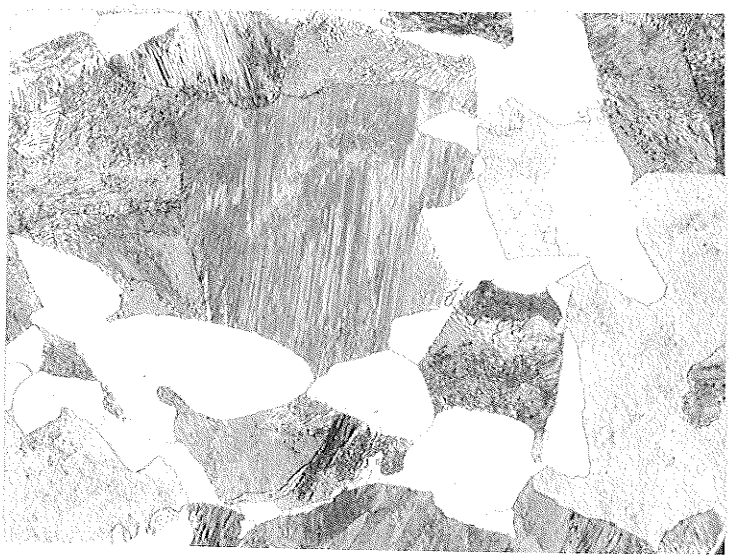

Figure 4.1 Etched microstructures: (a) steel A (b) steel D (c) steel E (400x)

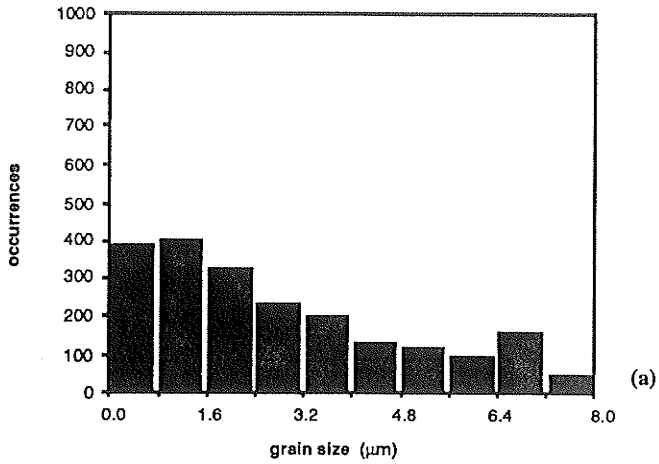

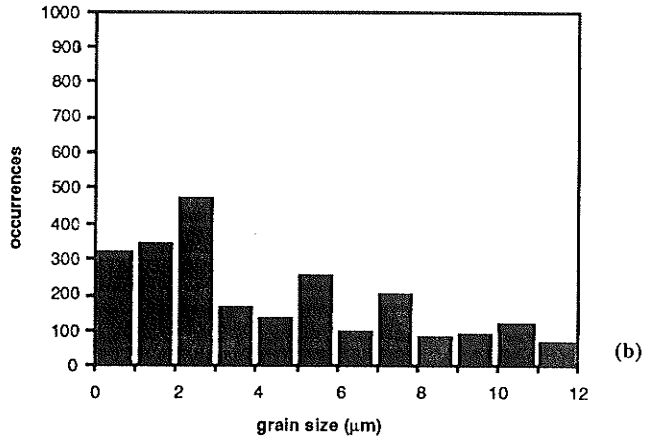

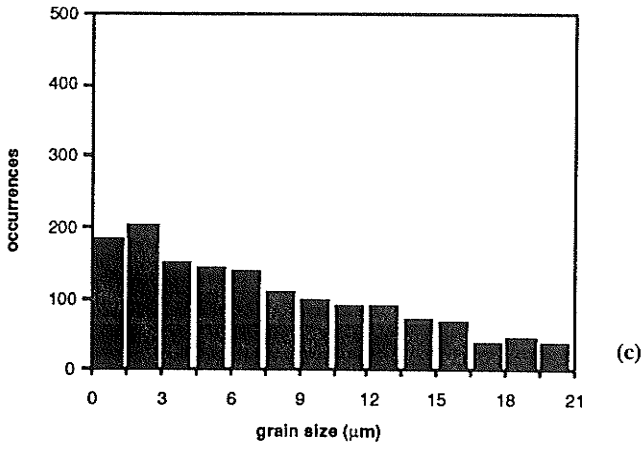

Figure 4.2 Proeutectoid grain size distributions: (a) steel A (b) steel D (c) steel E

The pearlite constituent in Fig. 4.1(a-c) generally consists of a randomly-oriented, lamellar structure of ferrite and cementite (Fe_3C) in all materials. Steel A in Fig. 4.1(a) shows a slight degree of spherodization of Fe_3C phase into neighboring ferrite grains. The pearlite also exhibits a coarsening effect similar to the ferrite grains, increasing in colony size from steel A to steel E as a result of the increasing austenitization temperatures. The apparent interlamellar spacing of pearlite in these micrographs varies from coarse to fine sizes. The distributions of interlamellar spacings were determined using the directed spacing method (outlined in section 3.5.4) on various TEM micrographs taken in each group, and the results are presented in histogram format in Figure 4.3(a-c). The mean interlamellar spacings determined from each histogram are 0.29, 0.28, and 0.32 μm for steels A, D, and E, respectively.

Table 4.1 summarizes the microstructural parameters in each of the steels along with the statistical error associated with each measurement. The results clearly show an increasing proeutectoid ferrite grain size, with relatively constant pearlite interlamellar spacing and volume fraction of proeutectoid ferrite in the three metals. These results are not surprising, considering the nature of the heat treatment schedules. The effect of the different ferrite grain sizes on various mechanical and substructural parameters is presented later on.

4.1.2 Size and Distribution of Non-Metallic Inclusions

An analysis of the distribution and morphology of non-metallic inclusions was performed to determine possible variations due to the progressively higher austenitization temperatures used in the heat treatment of the three sample groups.

As shown in Figure 3.1(b) in sec. 3.1. , the inclusion content is generally quite low in all sample groups. This produces a large degree of uncertainty in measuring their volume fraction. Computerized image analysis carried out on unetched, transverse sections

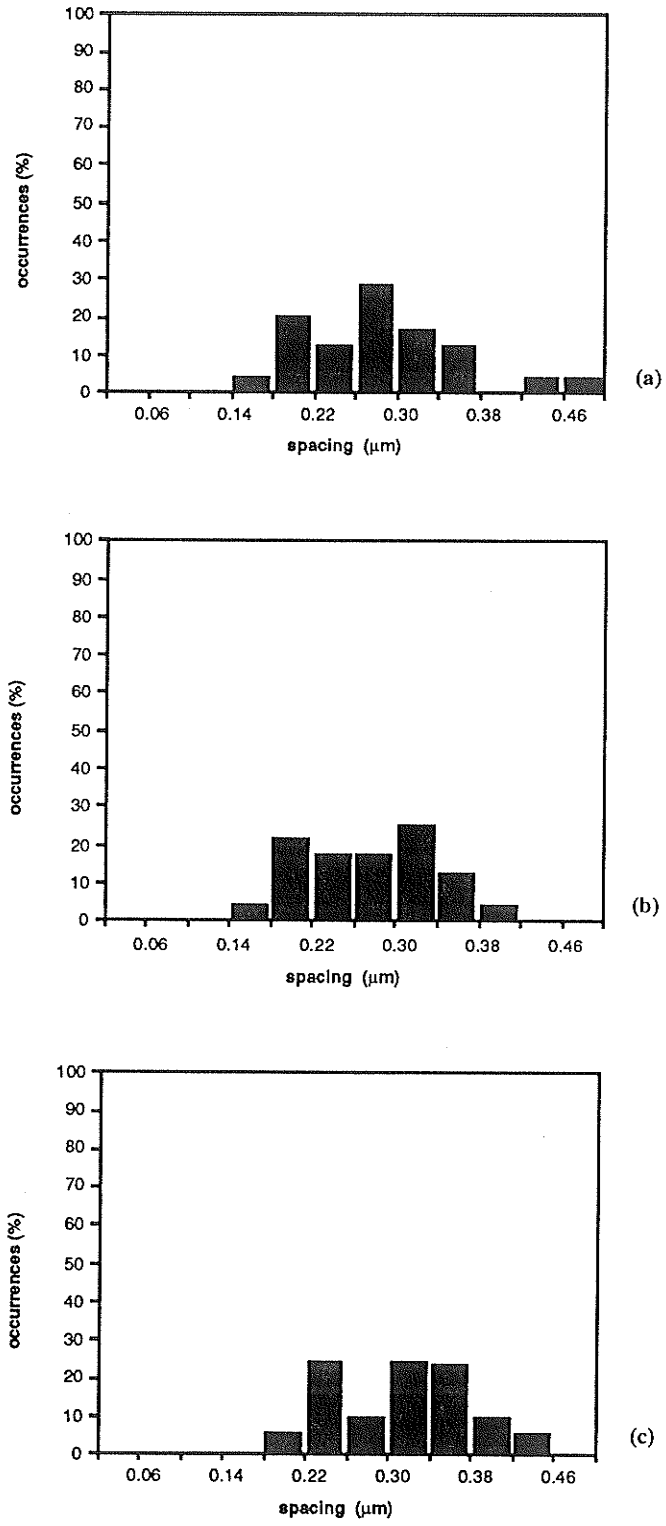

Figure 4.3 Pearlite interlamellar spacing distributions: (a) steel A b) steel D (c) steel E

Table 4.1 Microstructural Parameters of Sample Groups of 4340 Steel

Heat Treatment Schedules	Ferrite Grain Intercept Size L_α (μm)	Rel. Error (%)	Mean Pearlite Interlamellar Spacing, S_p (μm)	Rel. Error (%)	Vol. Fr. Ferrite (%)	Vol. Fr. Pearlite (%)	Rel. Error (%)
A	3.8±0.2	5.3	0.29±0.03	9.3	41.0	59.0	6.1
D	6.1±0.3	5.0	0.28±0.03	8.8	39.5	60.5	5.6
E	10.8±0.5	4.6	0.32±0.03	9.0	36.4	63.6	7.0

Table 4.2 Inclusion Size and Distribution of Sample Groups of 4340 Steel

Heat Treatment Schedule	Volume Fraction V_i (%)	Rel. Error (%)	Mean Chord Length L_i (μm)	Rel. Error (%)	Mean Free Path λ_i (mm)	Rel. Error (%)
A	0.10±0.04	39	2.2±0.2	9.1	2.7±1.3	47
D	0.08±0.03	38	2.6±0.3	11	3.9±1.8	46
E	0.12±0.03	27	2.3±0.2	8.7	2.1±0.7	33

determined the volume fractions occupied by non-metallic inclusions as 0.10, 0.08, and 0.12 % in steel groups A, D, and E, respectively.

The particular types and morphologies of inclusions observed in the steels by optical microscopy are illustrated in the micrographs in Figure 4.4(a-c). The most commonly occurring inclusion type were the grayish, elongated stringers in Fig. 4.4(a). These were identified as manganese sulfide (MnS) inclusions and are quite common in steels. The other main inclusion types often found in steels are silicates, oxides, nitrides, and carbides [3]. In Fig. 4.4(b), silicates appear dark and globular, while nitrides have a bright, angular appearance in Fig. 4.4(c). Oxide and nitride particles arise from the small additions of Al and Ti used to control the oxygen and nitrogen levels in "killed" steels. Ti is also known to form carbides and carbonitrides [3].

The distribution of inclusion sizes determined by mean chord length measurements ranged from 1 to 5 μm, with mean sizes of 2.2, 2.6, and 2.3 μm for steels A, D, and E, respectively. A measure of the linear spacing between non-metallic inclusions was determined by calculating the mean free path, λ_i, using the measured particle size and volume fraction in the relationship given by eqn. (3.6). The interparticle spacing can be an important parameter in correlations with void mechanisms of ductile fracture, as will be discussed later on. The mean free path between inclusions was calculated to be 2.7, 3.9, and 2.1 mm in steels A, D, and E, respectively. However, there is a high uncertainty attached to the values due to the very low volume fraction of inclusions present in this steel.

The values for the inclusion volume fraction, mean inclusion size, and mean free path are summarized in Table 4.2 along with the statistical error in the measurements. The small degree of variation in these parameters amongst the three steel groups indicates that the different heat treatments had little or no influence as far as inclusions are concerned.

a)

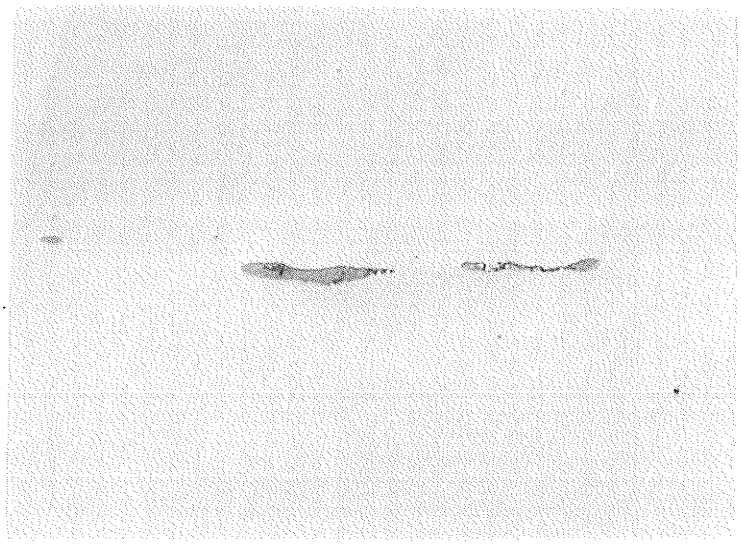

b)

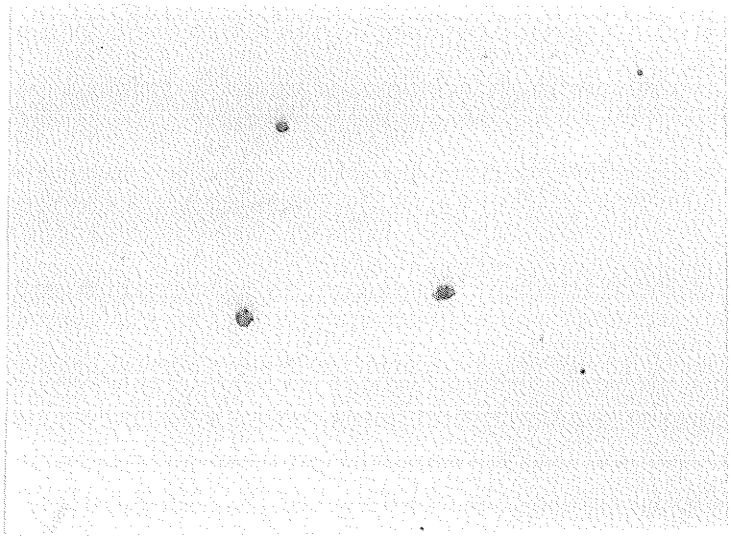

c)

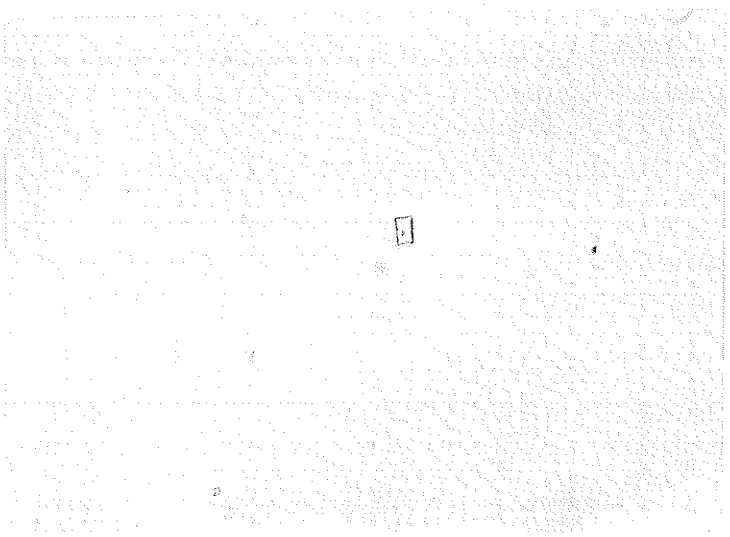

Figure 4.4 Inclusion types in 4340 steel: (a) manganese sulfides, (b) silicates, and (c) nitrides (400 x)

4.2 Flow Properties of 4340 Steel

Evaluation of the tensile flow properties was undertaken to characterize the work hardening behaviour of the groups of 4340 alloy steel. This information is important for later correlations between mechanical properties and microstructural and substructural parameters during tensile deformation.

4.2.1 Flow Curve Results

True stress-true strain (or flow) curves were constructed from engineering stress-strain data following the procedure outlined in section 3.3.1. Representative curves from each steel group are superimposed on a single graph in Figure 4.5 for comparative purposes. It is immediately apparent that all three flow curves lie closely together, exhibiting an initial high work hardening rate (slope of curve = $d\sigma/d\varepsilon$) up to about 10% true strain, with the work hardening rate rapidly decreasing to a low, near-constant value at larger strains. The general shape of the curves is suggestive of the parabolic, stage III work hardening behaviour typical of polycrystals [1]. However, some uncertainty in the actual behaviour of the flow curves arises due to the simple approximations used in extrapolating the curves beyond the onset of necking in tension. To verify the tensile results, microhardness testing was employed as an alternative means for determining the general shape of the flow curves without the complexities due to necking.

Measurements of true strain (based on local diameter) and Vickers diamond pyramid hardness were recorded at fixed increments along the gauge length of a broken tensile half from steel A. Combining the plastic strain and hardness readings resulted in a microhardness versus strain "flow curve" as depicted in Figure 4.6. As shown, the microhardness rises from a base value of 208 kg/mm^2 for unstrained material to a maximum of about 300 kg/mm^2 at strains in excess of ~ 60%. The data is closely approximated by a parabola (indicated by a solid line through the data points) which is

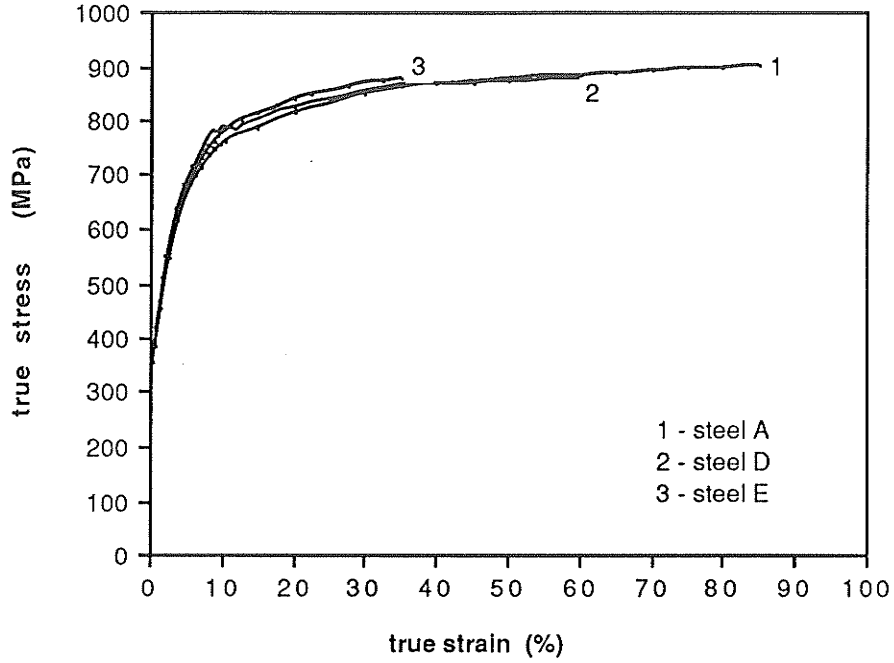

Figure 4.5 Flow curves of sample groups of 4340 steel

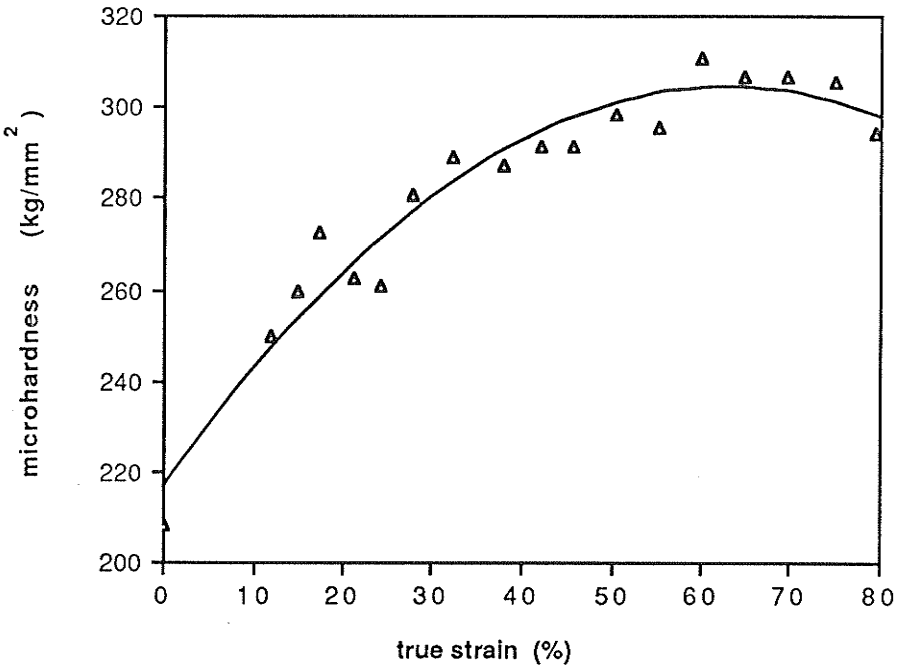

Figure 4.6 Microhardness vs true strain flow curve

Table 4.3 Flow Properties of 4340 Steel

Steel Group	Yield Stress (MPa)	Ultimate Stress (MPa)	Fracture Stress (MPa)	Fracture Strain (%)	Luders Strain (%)	Reduction in Area (%)	Modulus of Elasticity (GPa)	Hardening Exponent n	Strength Coefficient K (MPa)
A	410	783	902	88.9	1.16	58.9	211	0.17	1109
D	383	790	877	59.6	0.72	44.9	193	0.15	1089
E	356	773	884	37.4	<0.10	31.2	216	0.16	1121

similar to the shape exhibited by the tensile flow curves in Fig. 4.5. This result tends to justify the approximations used in constructing the true stress-true strain curves.

4.2.2 Dependence of Tensile Properties on Grain Size

Standard tensile properties were determined from the flow curves of Fig 4.5. The averaged results are presented in Table 4.3 for each steel group. As expected from Fig. 4.5, the flow properties of the three steels are quite similar, with the ultimate true stress σ_{UTS} varying between 773-790 MPa and the true fracture stress σ_F ranging from 887-902 MPa. The nearly constant values for the strain hardening and strength coefficients (n and K) reinforces the similar work hardening behaviour of the three steels. The average values of n = 0.16 and K = 1105 MPa compare well with literature values for annealed 4340 steel [121]. The modulus of elasticity, E, varies from 193-216 GPa (28-31 x 10^6 psi) which is in agreement with accepted values for steel.

The influence of the proeutectoid ferrite grain size variation is apparent in the values for yield stress, yield-point elongation (or Luders strain), and the total ductility (expressed as either reduction in area or fracture strain) for the steel categories. The yield stress, σ_{ys}, ranges from 410 MPa in steel A to 356 MPa in steel E, decreasing with increasing ferrite grain size. The true strain to fracture, ε_F, and the reduction in area, RA, follow a similar trend with grain size. The values of ε_F and RA vary from 88.9% and 58.9% respectively for the finer-grained steel A, to 37.4% and 31.2% respectively for the coarser-grained steel E.

It was found that both the yield strength (σ_{ys}) and fracture strain (ε_F) appear to obey a linear dependence on the inverse square root of ferrite grain size $(L_\alpha)^{-1/2}$ as shown in Fig. 4.7 for the three grain sizes evaluated in the study. This is, of course, the well-documented Hall-Petch relationship [10,11] which has been found to hold for nearly all metals.

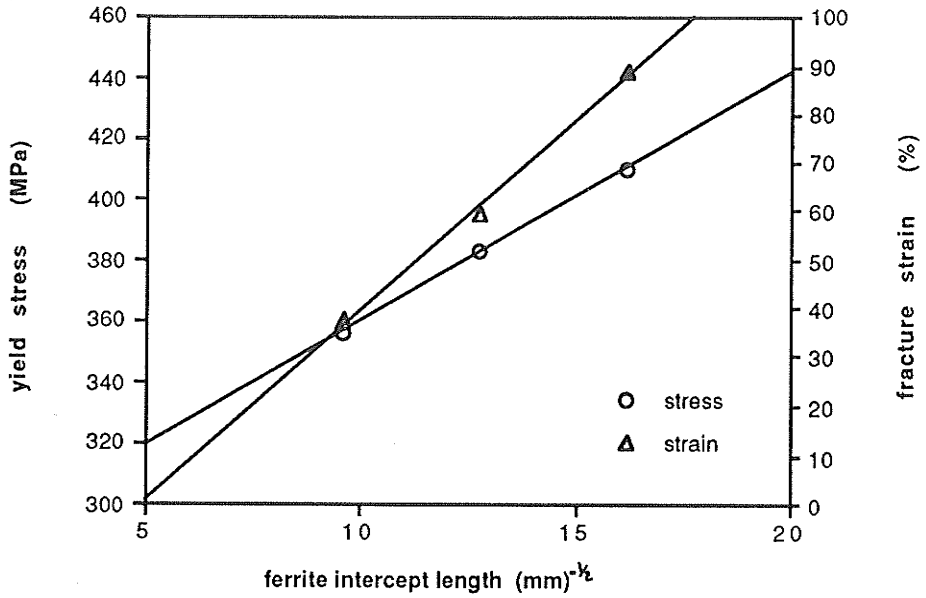

Figure 4.7 Variation in yield strength (σ_{ys}) and ductility (ε_F) with proeutectoid ferrite grain size ($L_\alpha^{-1/2}$)

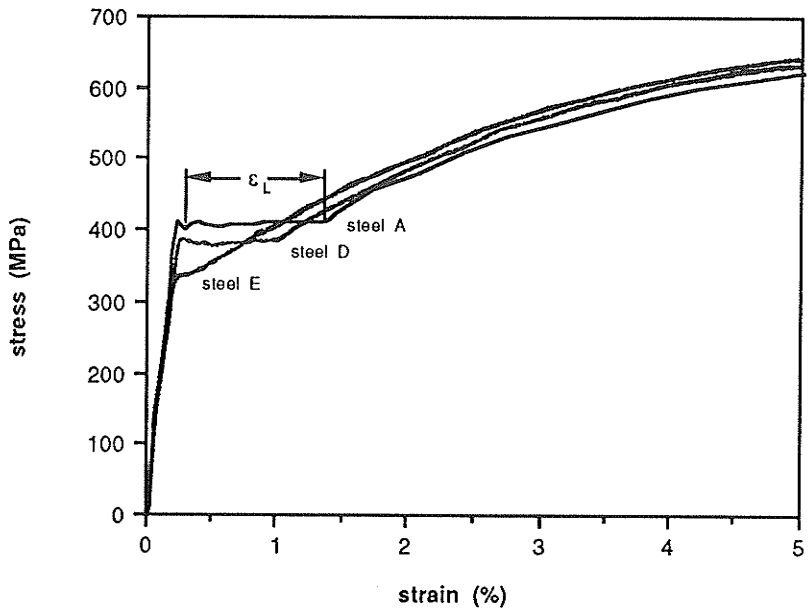

Figure 4.8 Variation in Luders strain (ε_L) of each steel group

The effect of grain size on the yield-point elongation phenomenon, or Luders strain, is graphically depicted in Fig. 4.8. The Luders strain decreases from about 1.2% in steel A to a negligible value (<0.1%) in steel E as the ferrite grain size increases.

In summary, the yielding properties and total ductility are dependent on the proeutectoid ferrite grain size whereas the work hardening and flow properties seem relatively unaffected in the three steel categories of this study.

4.3 Results of TEM Investigation

This section outlines the TEM observations of the substructural changes occurring during the tensile straining of 4340 steel in a qualitative manner. A quantitative description of the variation in substructural size with true strain and flow stress is also given.

4.3.1 Undeformed Microstructure of 4340 Steel

Typical micrographs of foils prepared from annealed material are shown in Figures 4.9 and 4.10, illustrating the undeformed structure of the proeutectoid ferrite grains and eutectoid pearlite. In Fig. 4.9, there is generally a very low dislocation content in ferrite grains, with individual dislocations distributed in a uniform manner. There is also evidence of tiny sub-micron particles (possibly carbides, oxides, or nitrides) located within ferrite grains. The inherent dislocations are mostly individual segments with a wavy nature typical of the many operative slip systems in BCC metals [4]. The spotty appearance of some dislocations may be attributed to an oscillatory contrast effect at dislocations running through the foil and observed near the Bragg condition [122].

The structure of undeformed pearlite in Fig. 4.10 shows thin, fairly straight cementite platelets which are relatively opaque to the electron beam and thus appear dark in the bright-field image. The interlamellar ferrite regions contain very few dislocations, although a higher dislocation content is observed at pearlite growth faults where dislocations emanate from the broken cementite plates.

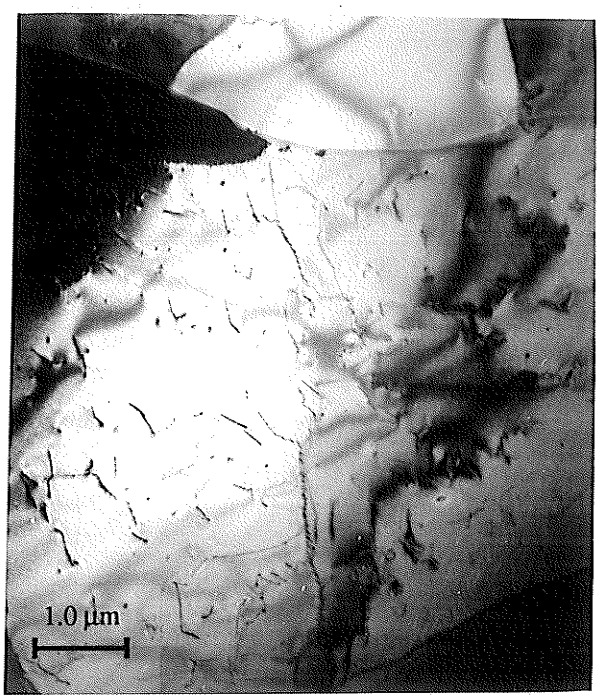

Figure 4.9 TEM micrograph of unstrained proeutectoid ferrite (12,000x)

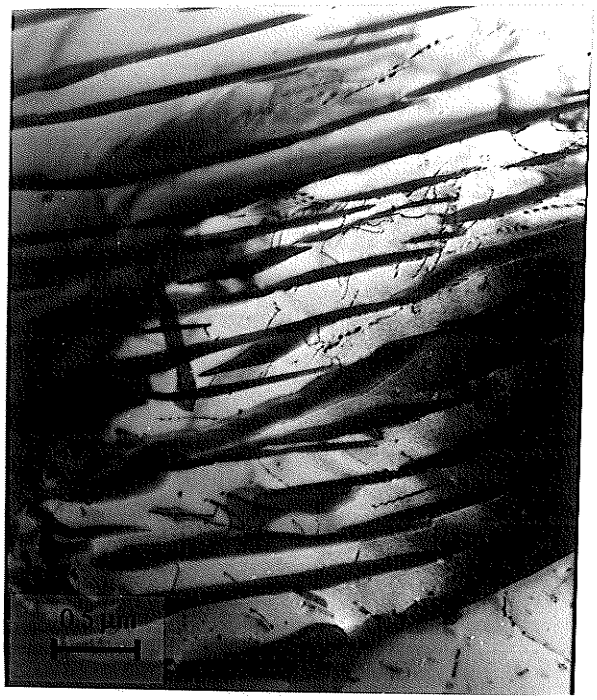

Figure 4.10 TEM micrograph of unstrained pearlite (12,000x)

4.3.2 Cell Evolution in Proeutectoid Ferrite Grains

TEM micrographs of thin foils prepared from samples of increasing levels of plastic deformation reveal the development and refinement of a dislocation substructure in ferrite grains, characterized by high dislocation density regions surrounding volumes of relatively low dislocation content. A similar sequence of cell formation was observed in all three sample groups and is depicted in the series of micrographs in Figures 4.11 to 4.13.

The process of cell formation can be followed with reference to the micrographs of Fig. 4.11(a-d) for steel A. At relatively low strains ($\varepsilon \cong 0.12$ in Fig 4.11(a)), the structure consists of dislocation tangles, loops, and dipoles produced by the interactions of long dislocation segments. Small particles are often associated with the tangled regions. At strains of about $\varepsilon = 0.18$ in Fig. 4.11(b), dense tangles have linked up to form the basis of an "incipient" cell structure. The tangled walls are quite ragged in appearance, with a considerable amount of dislocation activity within the cell interiors at this stage. As shown in Fig. 4.11(c) and (d), the cellular substructure becomes more well-defined and prevalent in ferrite grains throughout the structure as the macroscopic strain increases. Adjacent cells have become increasingly misoriented as evident in the abrupt changes in diffraction contrast, and cell walls are more closely spaced. At any given strain, a certain degree of size and shape variation in the cells is noticeable, due to the local inhomogeneity of internal stress produced by neighboring grains, grain boundaries, and pearlite colonies. A similar evolution and refinement of dislocation cells can be seen in Figure 4.12(a-d) and Figure 4.13(a-d) for steels D and E, respectively.

4.3.3 Special Observations

The micrographs shown in Figures 4.14-4.16 illustrate some interesting aspects pertaining to cells observed in ferrite grains in these steels. The composite micrograph in Fig. 4.14 shows the influence of the initial ferrite grain boundaries on cell formation. Dislocation cells are distributed along the grain boundaries, incorporating parts of the

(a) ε = 0.12

(b) ε = 0.18

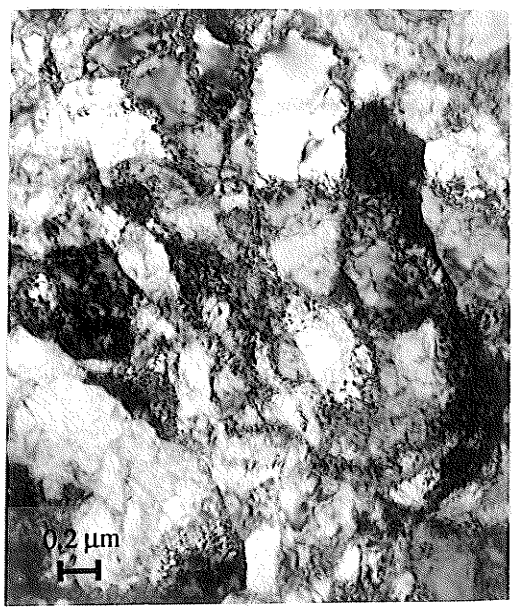

(c) ε = 0.30

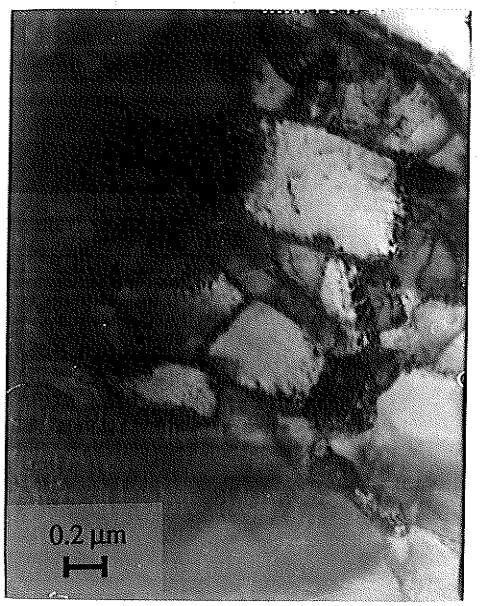

(d) ε = 0.40

Figure 4.11 Evolution of dislocation substructure in steel A (25,000x)

(a) ε = 0.05

(b) ε = 0.16

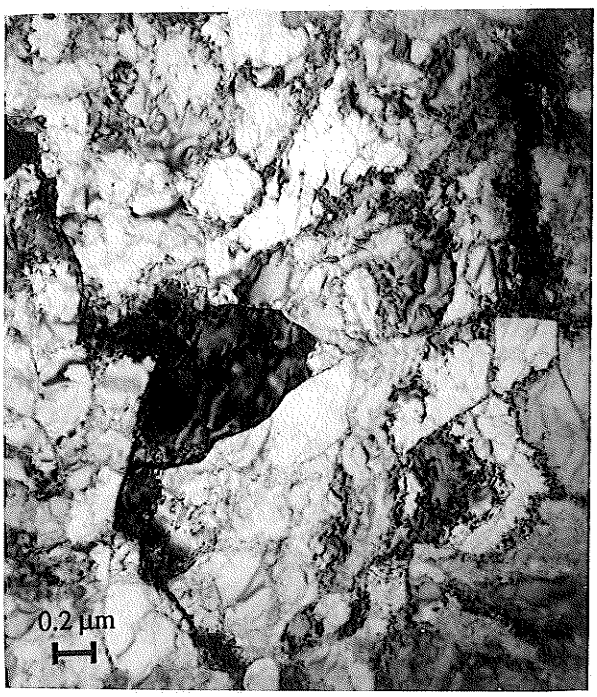

(c) ε = 0.27

(d) ε = 0.37

Figure 4.12 Evolution of dislocation substructure in steel D (25,000x)

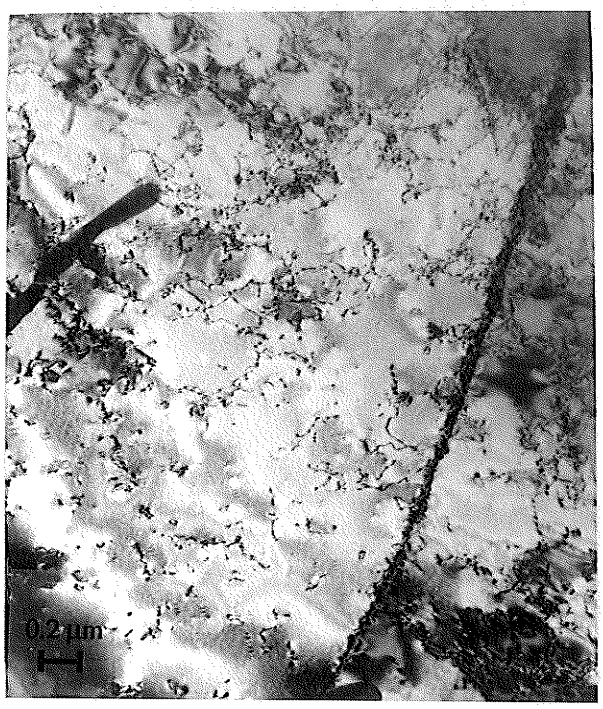

(a) ε = 0.08

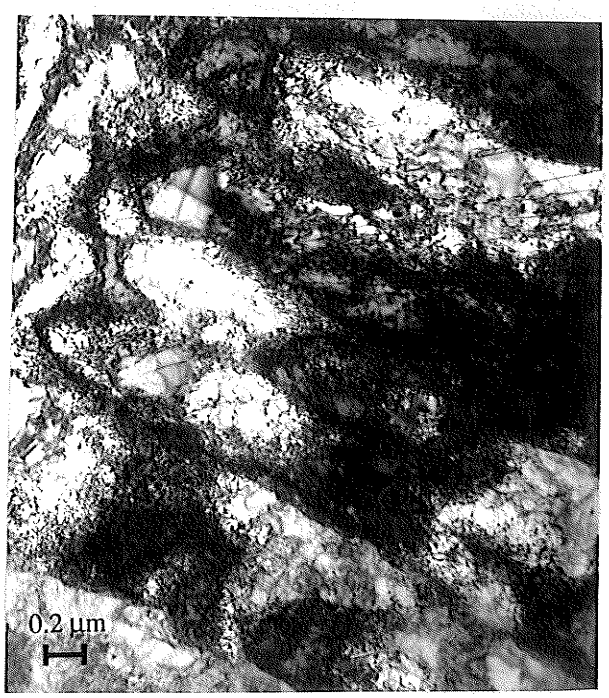

(b) ε = 0.15

(c) ε = 0.22

(d) ε = 0.26

Figure 4.13 Evolution of dislocation substructure in steel E (25,000x)

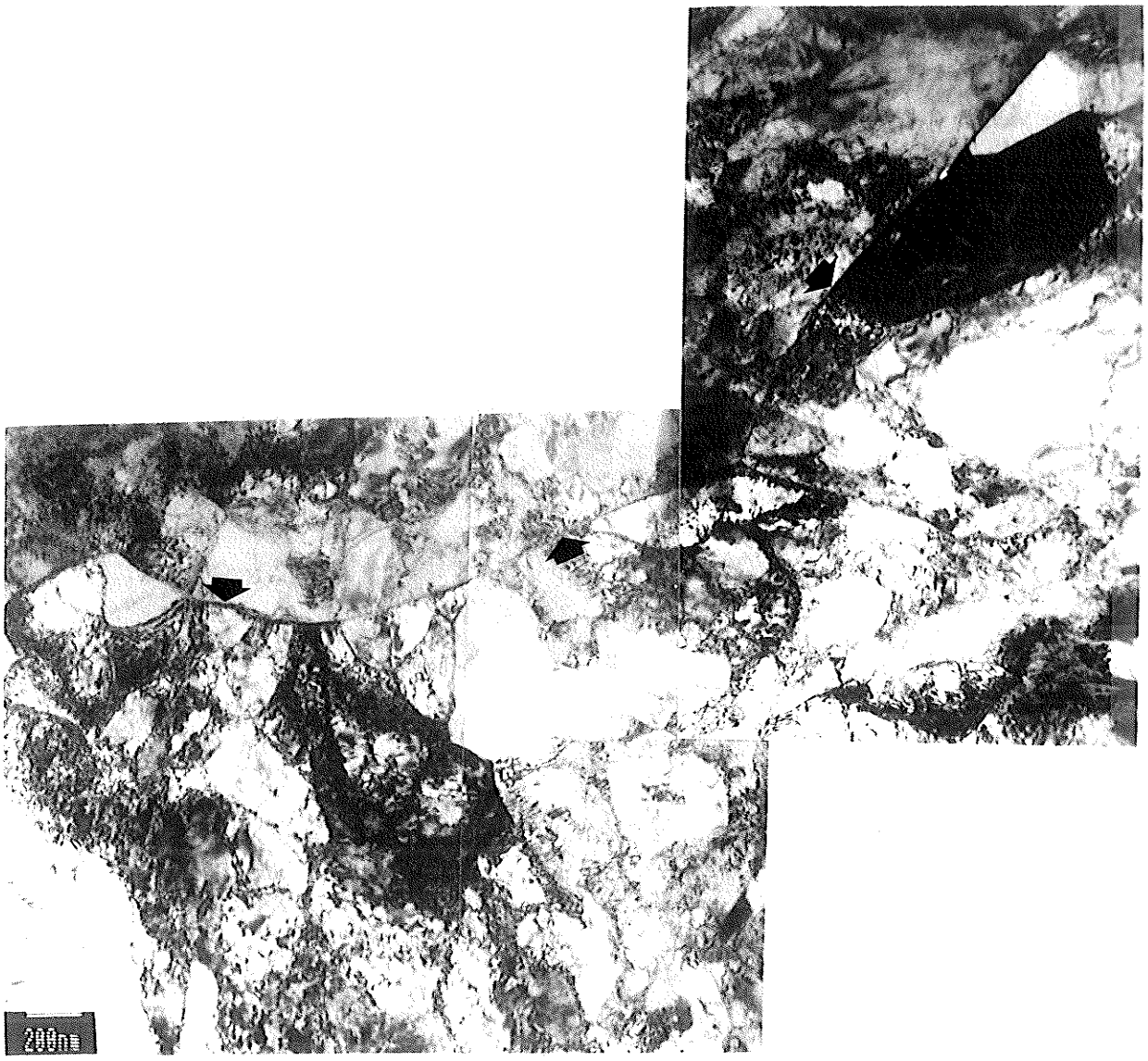

Figure 4.14 Influence of ferrite grain boundaries on cell formation (40,000x)

Figure 4.15 Hierarchical cell formation in ferrite grains (25,000x)

Figure 4.16 Subgrains in ferrite grains in 4340 steel (50,000x)

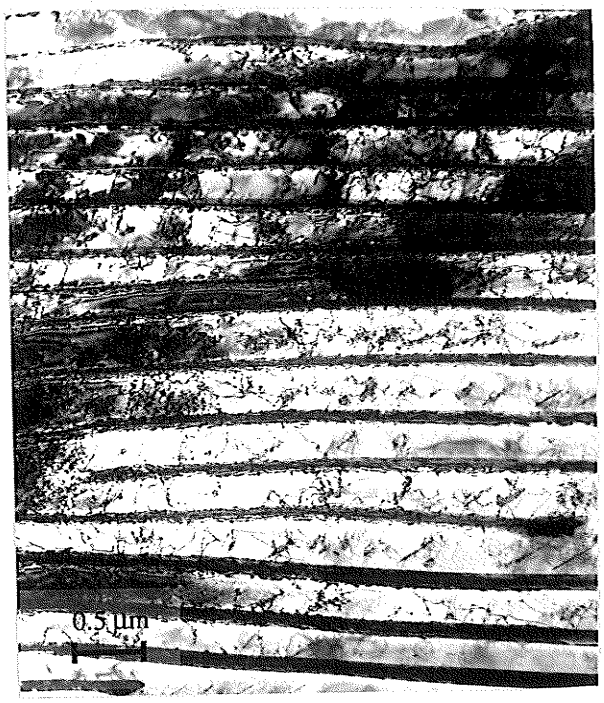

(a) ε = 0.08, 18,000x

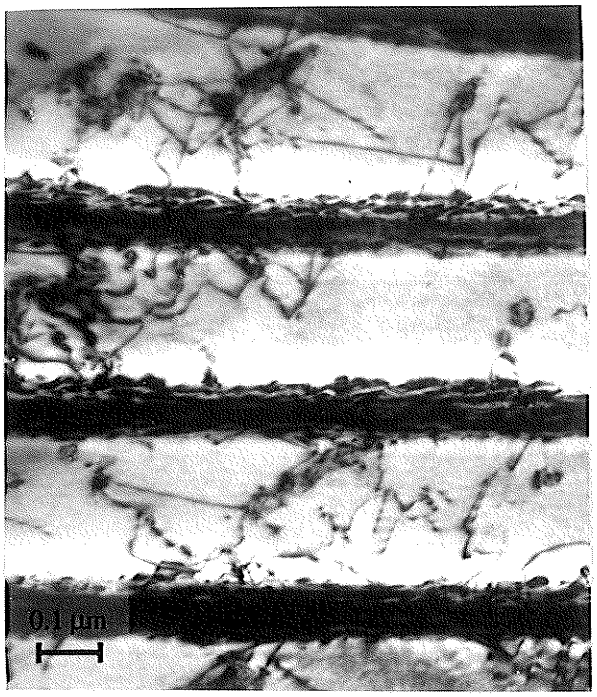

(b) detail of (a), 80,000x

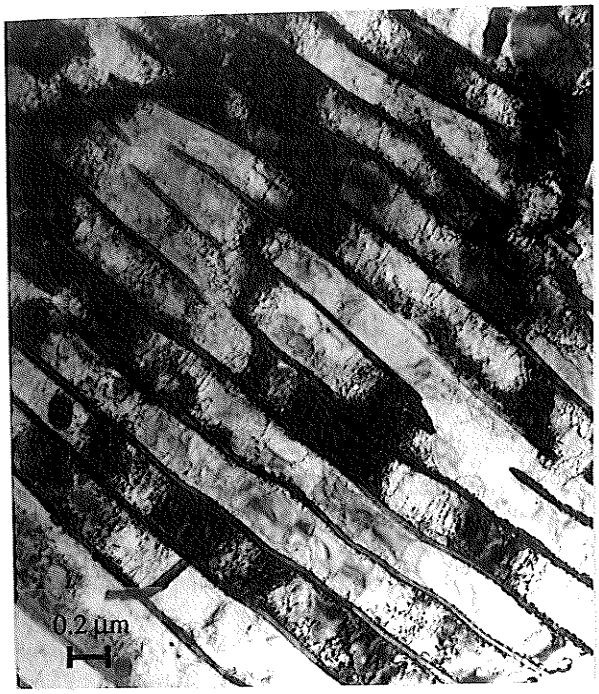

(c) ε = 0.15, 25,000x

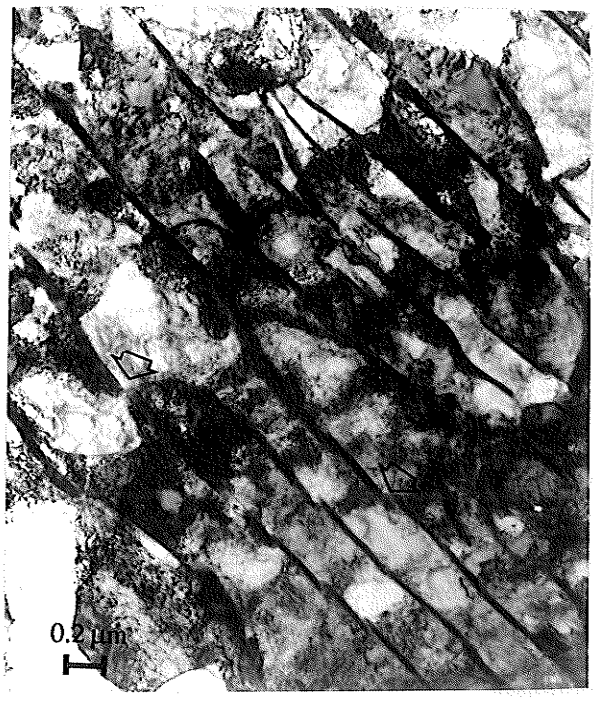

(d) ε = 0.30, 25,000x

Figure 4.17 Deformation structure in pearlite

boundary into the cell wall structure. The grain boundaries (indicated by arrows), however, remain intact and continuous, even after substantial plastic deformation. The importance of the ferrite grain boundaries in the yielding and flow of metals is well-known and will be discussed in the context of these results in later sections.

A second characteristic feature is the formation of "new" cell walls of lower dislocation density within pre-existing cells, as indicated by arrows in Fig. 4.15. This suggests a mechanism of cell multiplication whereby large cells are subdivided into "new", smaller cells so as to define a cell "hierarchy". Observations of a hierarchical cell structure have been reported and discussed by others [46,123].

A last striking feature observed at high strains of greater than $\varepsilon \cong 0.50$ in steel groups A and D is the localized appearance of a new cell morphology characterized by sharp, tight boundaries with an increased misorientation similar to the subgrain structure observed in recovered metals. Figure 4.16 illustrates elongated subgrains grouped into similar orientations so as to form what have been termed "microbands" [68]. Subgrain and microband formation at large plastic strains have been reported elsewhere [61-63, 68-71].

4.3.4 Deformation of Pearlite

As the morphology and interlamellar spacing of pearlite were shown to be quite similar in all three steels, the results of the TEM examination of this constituent are presented together.

The sequence of micrographs in Figure 4.17(a-d) shows that the substructural changes during the deformation of pearlite are quite different from that occurring in the ferrite grains. At small levels of deformation, $\varepsilon \cong 0.08$ in Fig. 4.17(a), profuse dislocation activity in the interlamellar ferrite phase is constrained by the neighboring cementite platelets which act as rigid, planar barriers to the movement of dislocations. A magnified view of the interlamellar ferrite regions in Fig. 4.17(b) shows a dislocation morphology of

dipoles, loops and tangles similar to the dislocation structures observed in ferrite grains at low strains. At larger plastic strains, $\varepsilon = 0.15$ in Fig. 4.17(c), deformation of the cementite phase is evident as Fe_3C platelets have begun to bend and fragment in areas. Also, dislocations in the ferrite phase have started to segregate into dense tangles, leaving regions of a relatively low dislocation density (i.e., an incipient cell structure). At high strains of $\varepsilon > 0.25$, cementite plates show evidence of localized shearing and large-scale bending as indicated by arrows in Fig. 4.17(d). Dislocation cells have formed in the interlamellar ferrite with an initial size roughly defined by the pearlite interlamellar spacing.

These features of pearlite deformation generally conform to observations made by other investigators [78-80]. It should be noted however, that the aforementioned deformation characteristics strongly depend on variations in both the orientation of pearlite colonies with respect to the tensile axis as well as the interlamellar spacing [78,81].

4.3.5 Variation in Cell Size with Flow Stress and Strain

Measurements of the average cell size in the proeutectoid ferrite using the linear intercept method were made in the range of plastic strain where well-developed substructures could easily be discerned. A similar measurement on cells formed in pearlite was not made since there was little observed change in the cell sizes there. However, it was noticed that cells found in pearlite were generally equivalent in size to the cells in ferrite grains at the same macroscopic strain level.

The mean cell size and standard deviation were determined from the distribution of intercept lengths at a given strain in all steels. In the histograms shown in Fig. 4.18(a-c) for three levels of plastic strain in steel A, it can be seen that the cell size distribution becomes narrower with increasing strain. This indicates that the cell sizes become more uniform at larger deformations. The average cell sizes (d) are tabulated along with the corresponding values of reduction in area (RA), true strain (ε), and true stress (σ) in Table 4.4 for each of the respective steel groups. Reduction in area and true strain were found

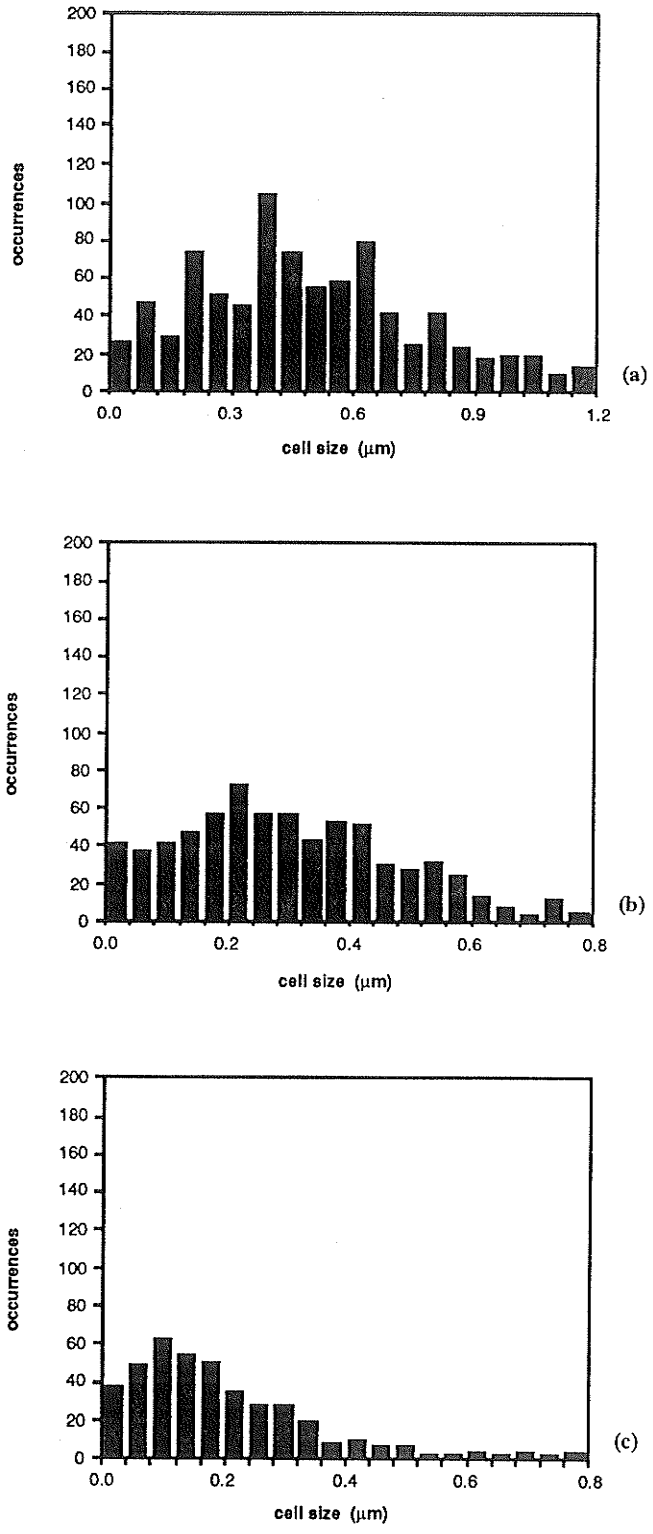

Figure 4.18 Cell intercept length distributions for steel A
(a) $\varepsilon = 0.15$ (b) $\varepsilon = 0.27$ (c) $\varepsilon = 0.47$

Table 4.4 Cell Size and Flow Data Results for Sample Groups of 4340 Steel

Steel Group	Reduction in area RA (%)	True Strain ε	True Stress σ (MPa)	Mean Cell Size, d (μm)	Relative Error (%)
A	14.0	0.15	788	0.57±0.08	13.6
	16.2	0.18	802	0.41±0.05	12.6
	19.0	0.21	817	0.46±0.07	16.2
	23.6	0.27	843	0.33±0.04	12.9
	26.0	0.30	851	0.23±0.02	7.6
	33.7	0.41	868	0.25±0.03	13.8
	37.5	0.47	878	0.20±0.05	23.9
	50.8	0.71	895	0.20±0.02	9.3
D	14.7	0.16	810	0.48±0.09	19.6
	19.8	0.22	834	0.44±0.08	18.0
	22.0	0.25	840	0.39±0.06	16.1
	26.9	0.31	856	0.34±0.04	12.0
	31.0	0.37	864	0.30±0.04	13.3
	35.0	0.43	874	0.28±0.03	11.5
	40.1	0.51	877	0.30±0.05	15.4
E	14.2	0.15	818	0.40±0.06	16.0
	16.2	0.18	829	0.43±0.07	16.4
	19.9	0.22	850	0.33±0.05	15.4
	22.7	0.26	860	0.35±0.06	15.7
	24.8	0.29	865	0.29±0.04	13.4
	29.7	0.35	880	0.24±0.04	15.2

from the measured foil diameter, d_i, using $RA=1-(d_i/d_o)^2$ and $\varepsilon=2\ln(d_o/d_i)$, respectively. True stress, σ, was determined from the flow curves obtained for each steel in Fig. 4.5.

The variation in cell size when plotted against plastic strain is as illustrated in Fig. 4.19(a-c) for each steel group. Referring to Fig 4.19(a), it is apparent that the cell size decreases rapidly with increasing strain up to about $\varepsilon = 0.40$, whereupon the cell size remains nearly constant with further straining to fracture. This trend is echoed in the other steels, although the plateau in the curve is diminished in steel D and non-existent in steel E. When the respective data for each steel is superimposed on a single graph as in Fig. 4.20, it seems apparent that the cell size variation with strain can be represented by a single curve, showing little influence of the different proeutectoid ferrite grain sizes. The cell size decreases to a near-constant value of 0.2-0.3 μm for plastic strains of $\varepsilon \cong 0.40$ and greater, regardless of the initial grain size.

The variation in both the cell size and flow stress with plastic strain is illustrated in Figure 4.21(a-c) for each of the steels. The flow curves seems to "mirror" the cell size curves, suggesting that a linear relationship between flow stress (σ) and inverse cell size $(d)^{-1}$ may be applicable in these steels. This is substantiated in the plots of flow stress versus inverse cell size depicted in Figure 4.22(a-c) for the three steels. The figures show that the relationship between flow stress and cell size may be described by an equation of the form

$$\sigma = \sigma_o + C(d)^{-1} \qquad (4.1)$$

where the constants σ_o and C correspond to the intercept and slope, respectively, of a straight line through the data. These constants, determined by regression analysis, are given in Table 4.5 along with the correlation coefficients for each steel. From the table, σ_o varies from 735-756 MPa and C varies between 27.8-40.2 MPa.μm, indicating a similar behaviour for all of the steels investigated in this study.

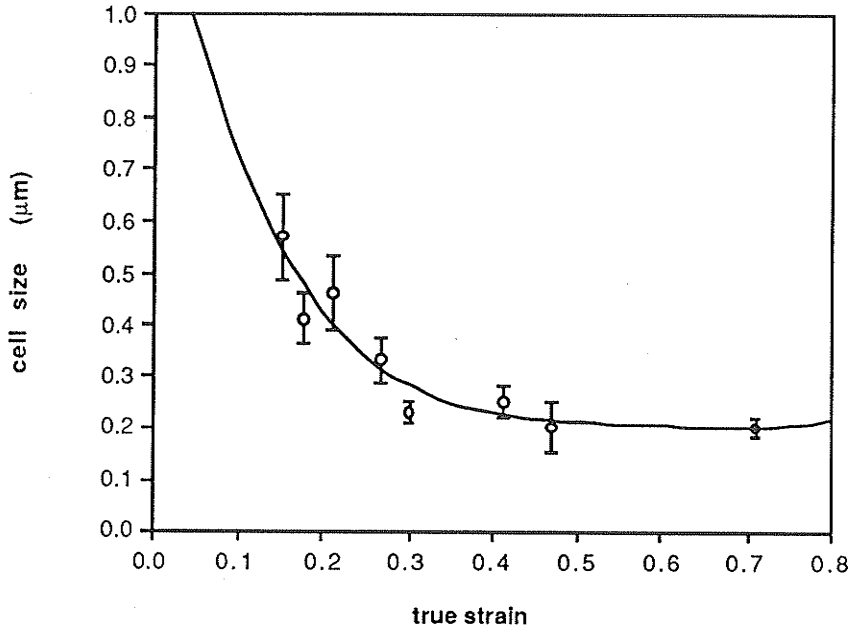

Figure 4.19 (a) Variation in dislocation cell size with plastic strain for steel A, ferrite grain size = 3.8 μm

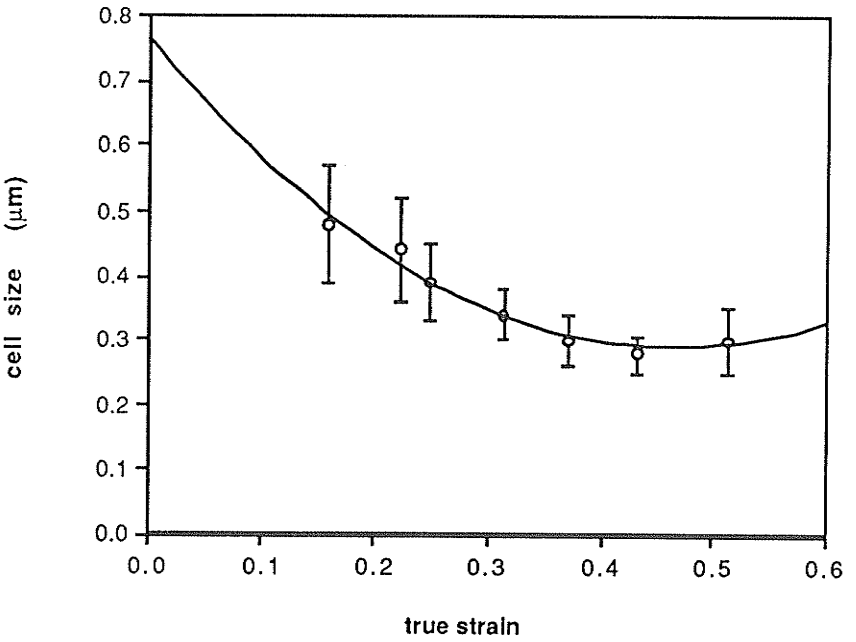

Figure 4.19 (b) Variation in dislocation cell size with plastic strain for steel D, ferrite grain size = 6.1 μm

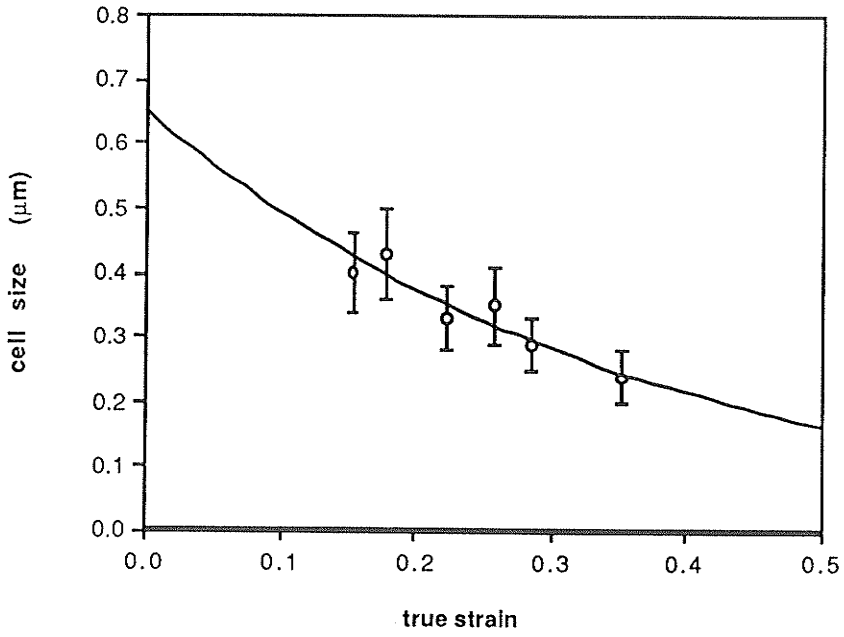

Figure 4.19 (c) Variation in dislocation cell size with plastic strain for steel E, ferrite grain size = 10.8 μm

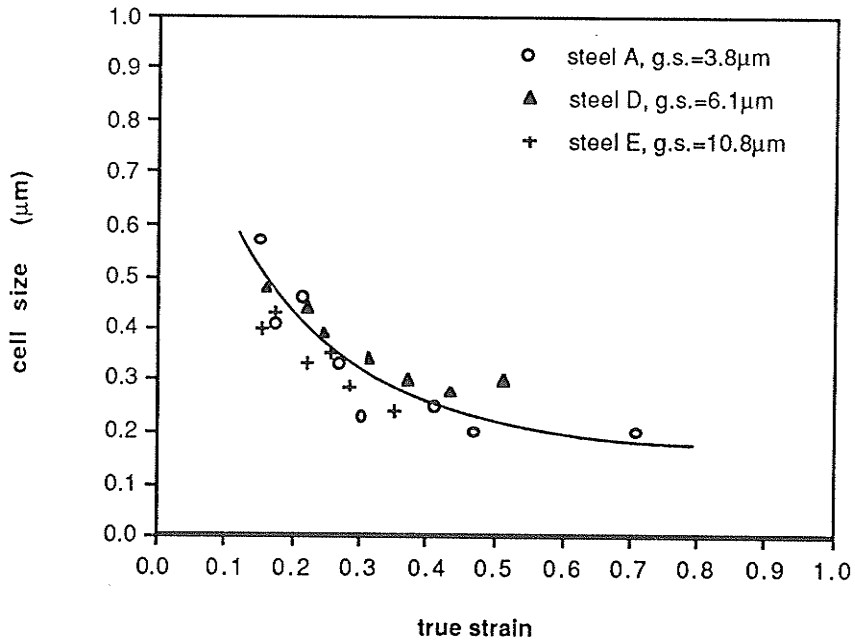

Figure 4.20 Variation in Cell Size with Plastic strain for combined data from all steel groups

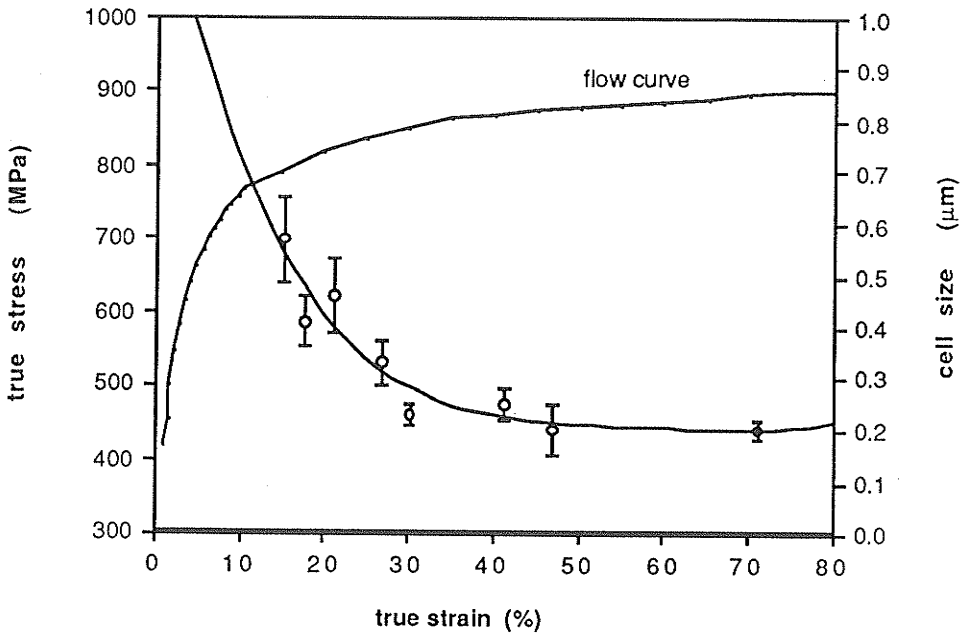

Figure 4.21 (a) Variation in cell size and flow stress with plastic strain for steel A, ferrite grain size = 3.8 μm

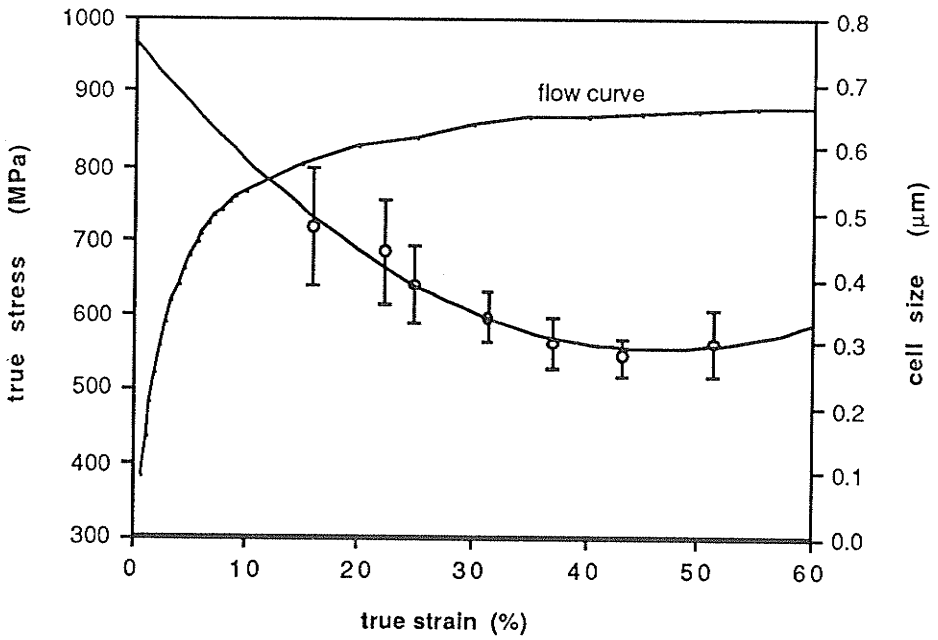

Figure 4.21 (b) Variation in cell size and flow stress with plastic strain for steel D, ferrite grain size = 6.1 μm

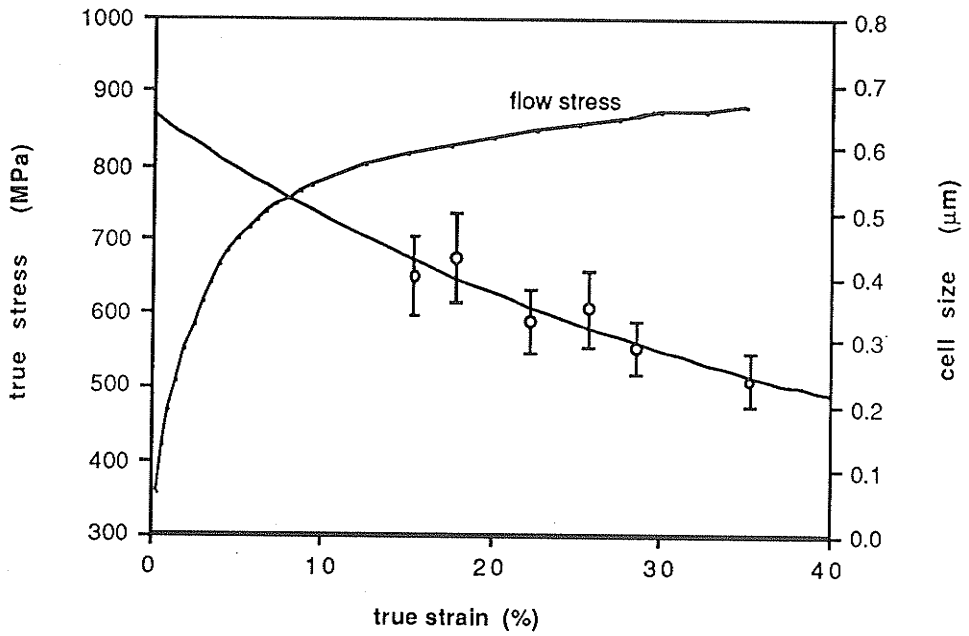

Figure 4.21 (c) Variation in cell size and flow stress with plastic strain for steel E, ferrite grain size = 10.8 μm

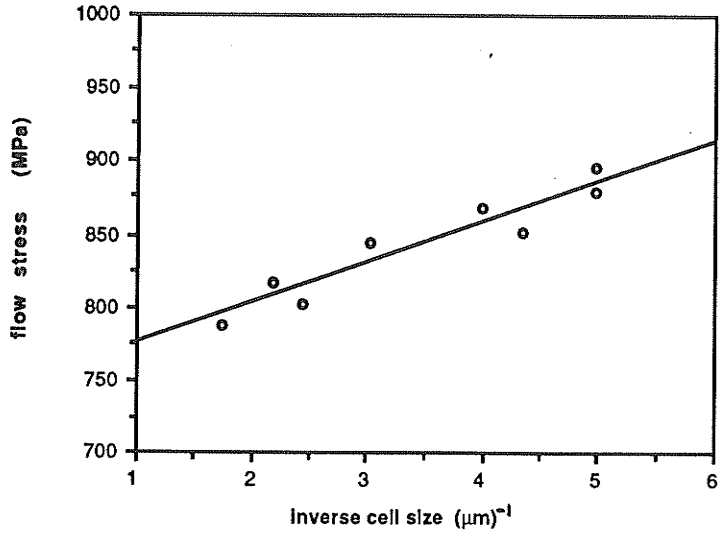

Figure 4.22 (a) Dependence between flow stress and inverse cell size for steel A, ferrite grain size = 3.8 μm

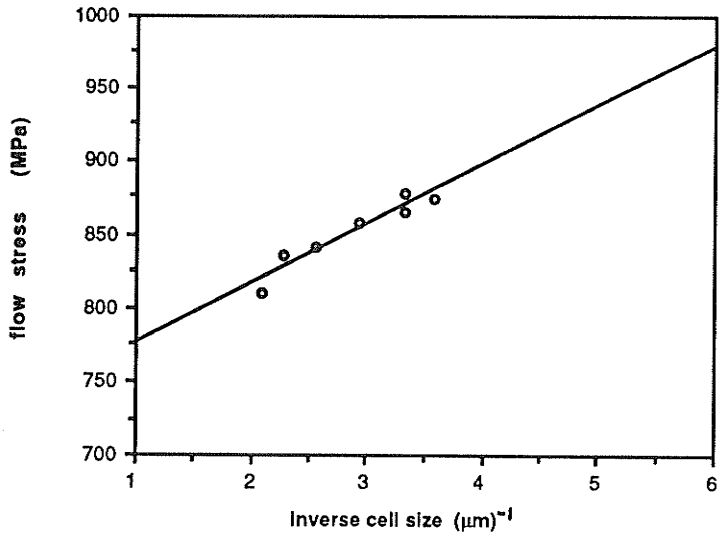

Figure 4.22 (b) Dependence between flow stress and inverse cell size for steel D, ferrite grain size = 6.1 μm

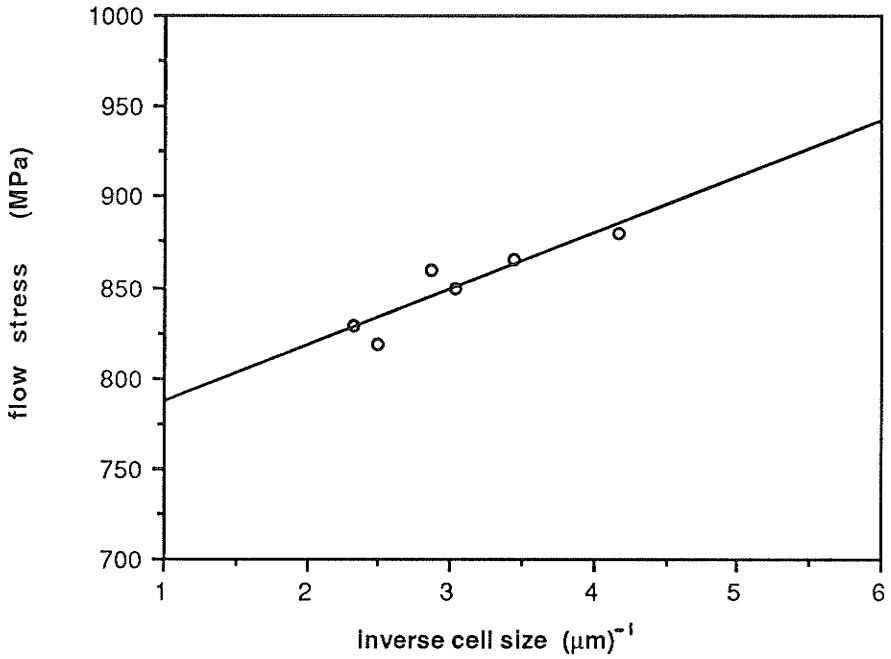

Figure 4.22 (c) Dependence between flow stress and inverse cell size for steel E, ferrite grain size = 10.8 μm

Table 4.5 Results of Linear Regression Analysis of Cell Size/Flow Stress Data

Steel Group	Intercept σ_0 (MPa)	Slope C (MPa.μm)	Correlation Coefficient
A	746	27.8	0.95
D	735	40.2	0.96
E	756	31.0	0.90

Overall, these results indicate that a similar process of work hardening and deformation occurs in all the steel groups, with little apparent influence from the different proeutectoid ferrite grain sizes. This aspect is to be developed in the discussion of the results.

4.4 Results of SEM Examination

Scanning Electron Microscopy, or SEM, was conducted on broken tensile specimens in order to characterize the microscopic fracture process in 4340 steel. The results presented include qualitative observations of the surface topography as well as a quantitative analysis of voids or "dimples" located in the fracture surfaces. In later sections, a correlation of the SEM and TEM results will be made in order to develop an understanding of the link between the fracture process and the micro-mechanisms of plastic deformation preceding it.

4.4.1 Void Size Distribution

The 4340 alloy steel was found to fail by a "cup and cone" fracture process common in many ductile metals [2]. The central fibrous region in Figure 4.23 shows a fine distribution of dimples characteristic of ductile fracture by void initiation, growth, and coalescence. The irregular surface topography shows that microscopic crack propagation by void coalescence deviated frequently from a plane normal to the tensile axis of the specimen.

Typical SEM micrographs in Figure 4.24(a-c) indicate the morphology of voids present in each of the respective metal groups. The voids in these micrographs exhibit a fairly wide variation in size and shape. Although most voids appear circular, the presence of elongated voids may indicate the occurrence of localized shear stresses in addition to tensile stresses during their formation [124]. It is also noticeable that many of the larger voids present are actually composed of smaller, shallow voids.

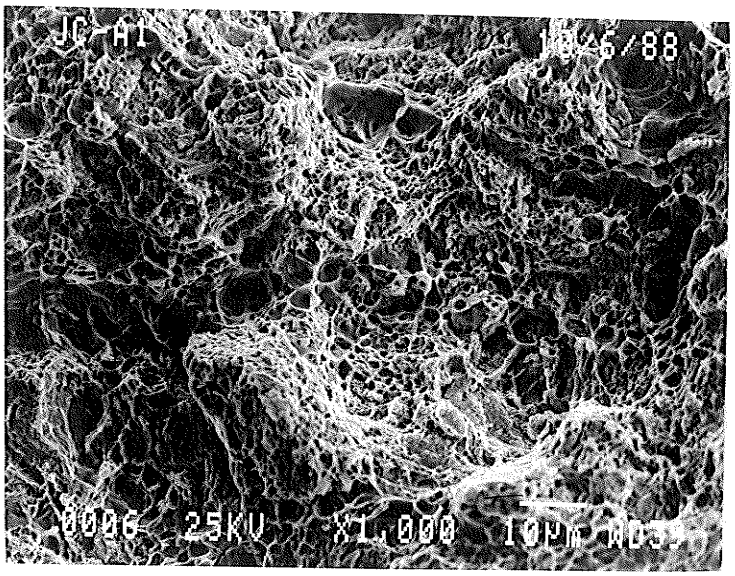

Figure 4.23 Fracture surface topography of 4340 steel tensile sample

(a)

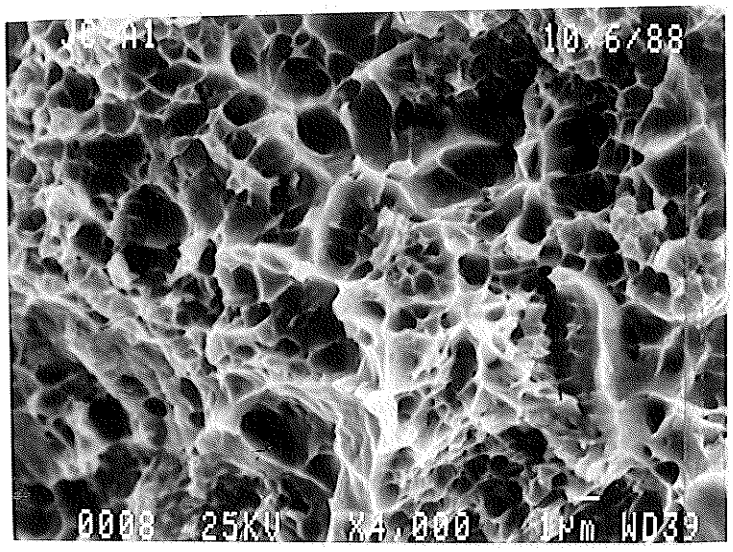

(b)

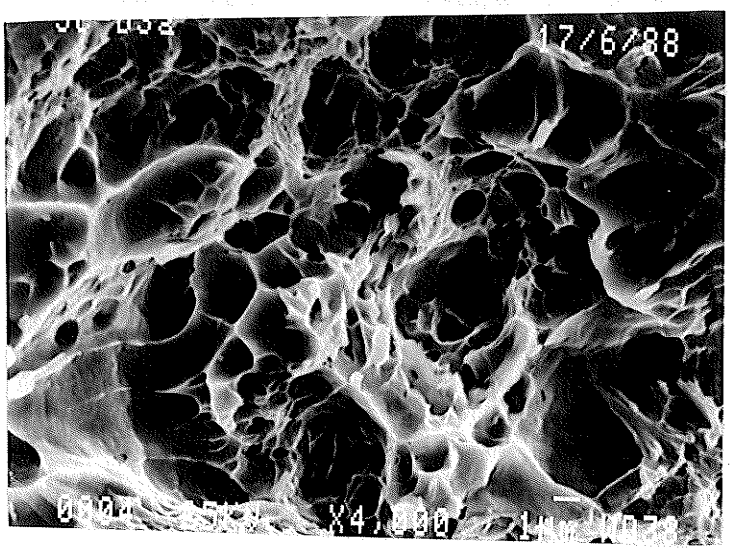

(c)

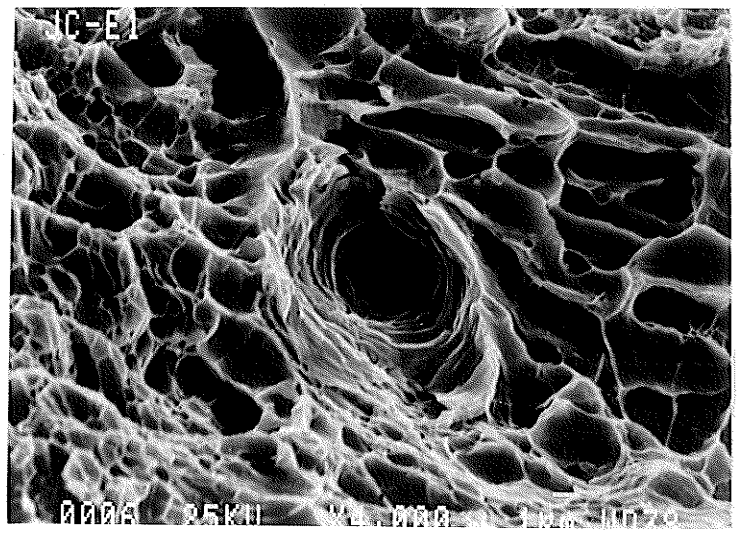

Figure 4.24 Morphology of voids (dimples) on tensile fracture surfaces
(a) steel A (b) steel D (c) steel E

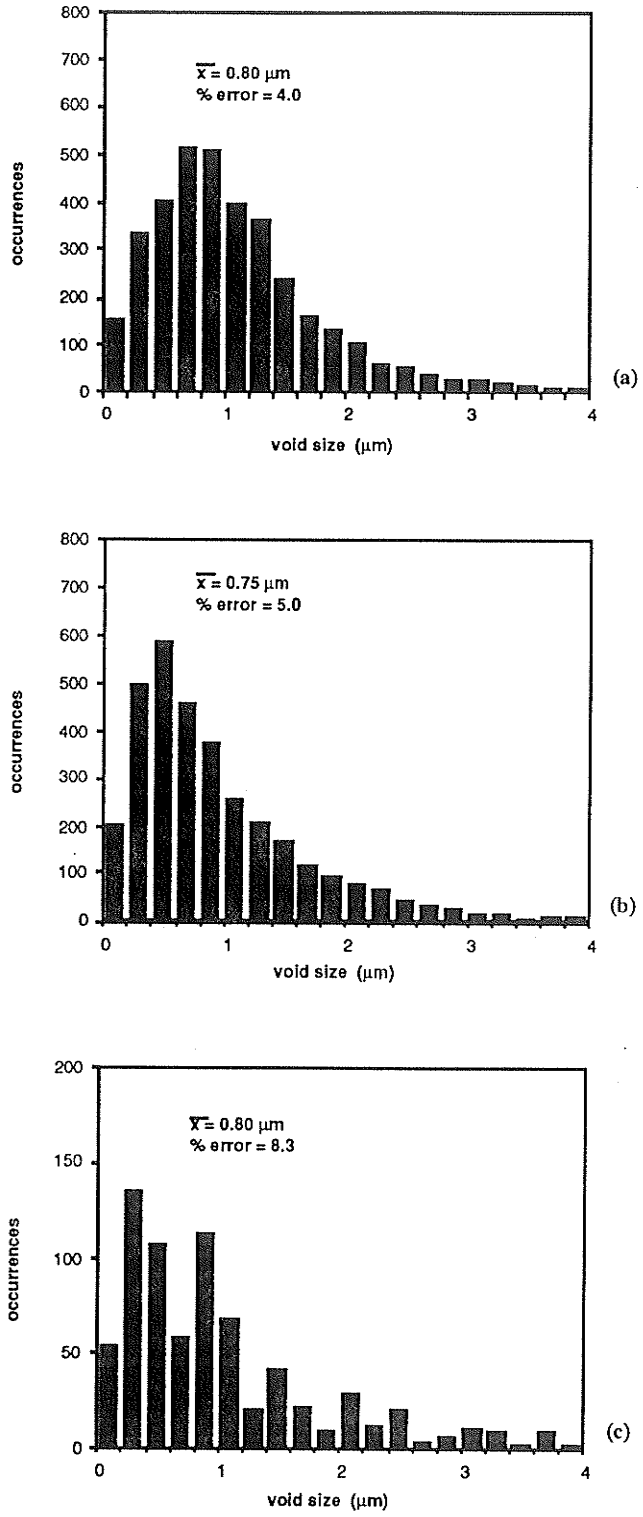

Figure 4.25 Void size distributions: (a) steel A (b) steel D (c) steel E

(a)

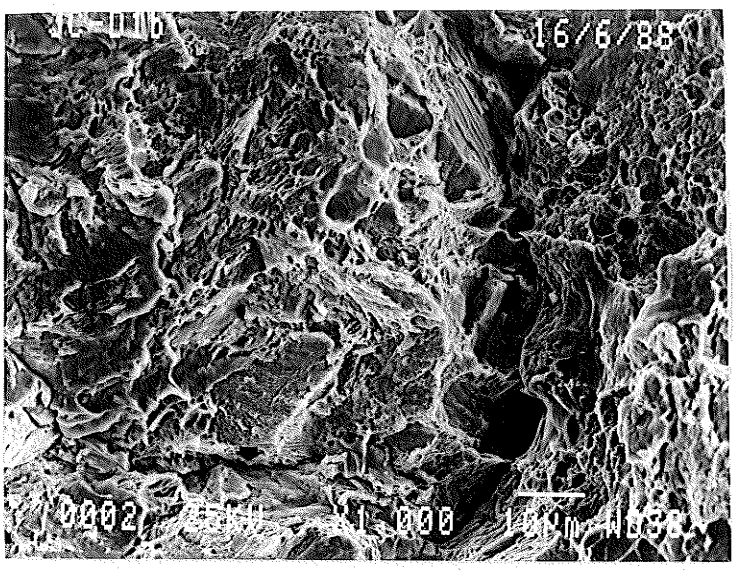

(b)

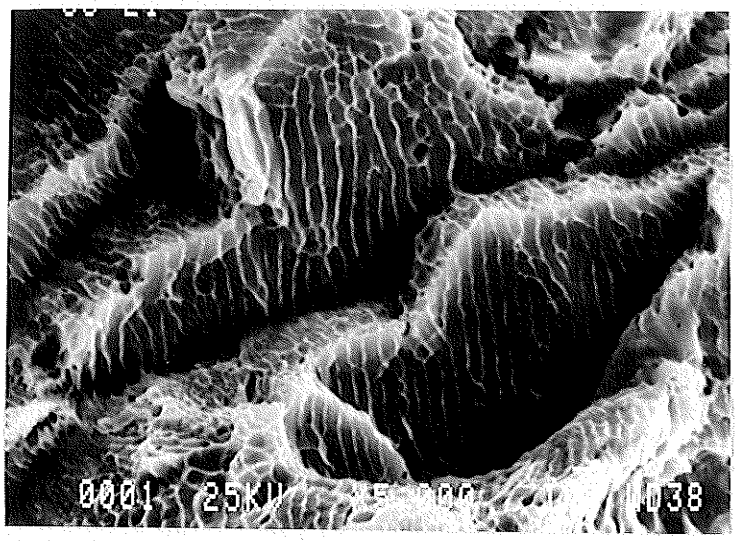

(c)

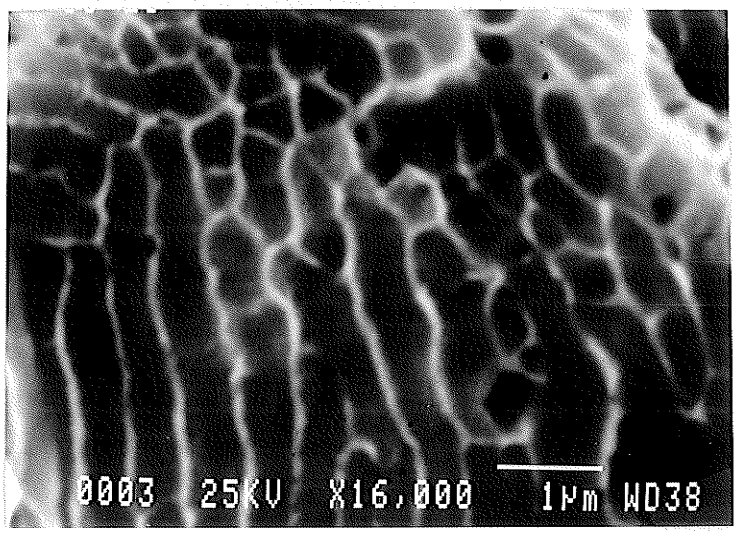

Figure 4.26 Fracture surface regions associated with pearlite
(a) evidence of cleavage and microcracks
(b) and (c) evidence of microvoids in interlamellar ferrite

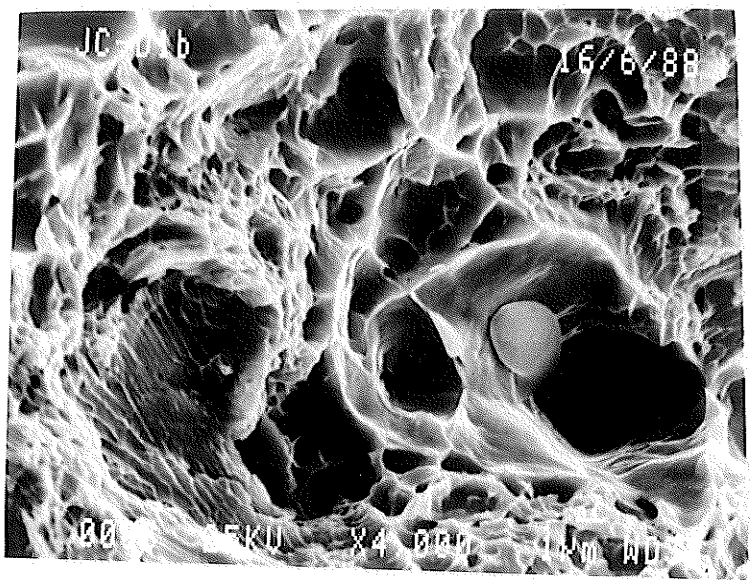

Figure 4.27 Location of inclusion within void on fracture surface

A statistical analysis of the distribution and mean size of voids is presented in Fig. 4.25(a-c) for each steel group. The histograms illustrate the wide range of void sizes, although the mean size is nearly equal to 0.8 μm in all of the steels.

4.4.2 Additional Observations

In addition to the void topography observed in the steels, some other interesting features deserve mention. The first concerns the observation of localized cleavage and microcracks associated with the pearlite constituent of 4340. In Figure 4.26(a), cleavage facets and microcracks running along the boundaries of pearlite colonies can be seen (as indicated by arrows). On closer inspection in Fig. 4.26(b) and (c), shallow "microvoids" are visible in the interlamellar regions between cementite platelets, which appear as bright, parallel ridges in the micrograph. This indicates that a void mechanism of fracture is applicable to the pearlite colonies as well as the proeutectoid ferrite grains.

A second observation involves the presence of inclusions and particles, which are generally accepted to be preferential sites for void nucleation during ductile fracture. In the micrographs of Fig. 4.24(a-c) however, there is a general lack of inclusions or particles associated with voids in the tensile fracture surface, which is in accordance with the low volume fraction of inclusions determined by metallography (section 4.1.2). It should be noted though, that particles as small as 50 Å, which are not easily detected by SEM, have been shown to nucleate voids [103]. A rare micrograph in Figure 4.27 shows a particle of a few microns in size situated inside a void of a much larger size than surrounding voids. This indicates that inclusions in 4340 steel do contribute to void formation, but the majority of voids are nucleated by a mechanism which is not related to inclusions.

Chapter V

DISCUSSION

5.1 Application of the Mesh Length Theory to Plastic Deformation in 4340 Steel

5.1.1 Introduction

In this section of the discussion, the salient features of the substructural evolution in 4340 low alloy steel revealed by the TEM investigation are reviewed. As stated earlier, the "mesh length" theory of work hardening proposed by Kuhlmann-Wilsdorf has been successfully used to explain the deformation behaviour of single crystals and mostly pure, single phase metals. The validity and limitations of the theory as applied to the plastic deformation process in a material with a more complex material are shown.

5.1.2 Cell Evolution during Deformation

The TEM investigation of this study reveals the formation and evolution of a dislocation substructure as a result of continued tensile deformation in the steel. The micrographs in Figures 4.11-4.13 show that the structure progresses from an irregular assembly of loosely tangled dislocations to a well-defined cell boundary structure enclosing misoriented volumes relatively free of dislocations.

This structure is presumably an example of LEDS (Low Energy Dislocation Structure) in that it represents the configuration of lowest strain energy available to glide dislocations under a given applied stress. This is, of course, subject to restrictions to the mobility of dislocations arising from the available slip systems, stacking fault energy, the temperature and strain rate of deformation, and microstructural barriers in the material. Given the availability of slip systems and the three-dimensional mobility of dislocations by cross slip in this ductile material, cell formation is inevitable.

According to the theory proposed by Kuhlmann-Wilsdorf [32-36], dislocations in a cell wall arrangement mutually "screen" each other's stress fields to the distance between neighbouring dislocations, so that long range stresses are nearly eliminated and the energy of the configuration is minimized. Computer modelling and analysis by Bassim [37,38] have confirmed the low strain energy associated with various cell structure models and have shown that a further reduction in energy is attained if neighboring cells have an alternating sense of misorientation, sometimes referred to as the "checkerboard pattern"[34]. The occurrence of cells in favor of higher energy arrangements such as dislocation pile-ups supports the principle of energy minimization for this material. However, the cells in the material tested in the present study appear to be more or less randomly orientated and do not exhibit a "checkerboard" arrangement.

As mentioned earlier, the flow curves and accompanying cell sizes were found to vary in a similar manner with plastic deformation for the different metal groups studied. The graphs in Figures 4.21(a-c) illustrate the sequence of cell development in relation to the state of plastic deformation for each grain size. From the figures, well developed dislocation cells are present in proeutectoid ferrite grains after strains of ~ 0.15 and decrease in size with further straining until about $\varepsilon = 0.50$, whereupon the cell size remains virtually constant at 0.2-0.3 μm. Cells in steel E do not reach a limiting size as fracture occurs at a lower strain of $\varepsilon \cong 0.35$. The shrinking of cells to a limiting value has been reported previously for this alloy [94,95] as well as for an HSLA steel [47] and Cu [45].

It is evident from Fig. 4.21(a-c) that the cell size decreases with increasing flow stress, which is expected from mesh length hardening if one assumes that the average link length in the cell walls decreases proportionately to the cell size. However, the flow stress in the strain range where cells are formed exhibits a curved, parabolic shape suggestive of stage III behaviour with a decreasing work hardening rate. In contrast, at lower strains ($\varepsilon < 0.10$) where cells have yet to form, the flow stress rises almost linearly with a much higher work hardening rate. These observations conflict with experimental observations of

cell multiplication associated with the higher, near-linear work hardening range (i.e., stage II) which is theoretically expected from mesh length principles. The differences in work hardening behaviour lie in the relative contribution from cell mechanisms to the overall strengthening behaviour of this two-phase material.

Cell formation in pearlitic ferrite occurs later than in proeutectoid ferrite. At strains of $\varepsilon \cong 0.25$, cells in the ferrite lamellae are observed with an initial size about equal to the interlamellar spacing of pearlite, or about 0.3 μm. This finding is in agreement with other studies of substructure evolution in pearlite [78-80]. As shown in Fig. 4.17(d), the onset of cells coincides with large scale deformation of the cementite (Fe_3C) which implies that Fe_3C platelets serve as barriers to dislocation motion and inhibit cell formation at lower strains. As seen later on, the Fe_3C phase plays an important role in the formation of cells and the strengthening of 4340 steel.

5.1.3 Similitude

One of the key facets of the mesh length work hardening theory is the concept of "similitude" introduced in sec. 2.7.2. The basic principle, restated, is that the dimensions of the dislocation cell pattern decrease as the applied stress and strain increase, but the pattern remains geometrically similar to itself, i.e., it maintains "similitude" [33]. Furthermore, it follows from energy minimization principles that a proportionality between the average cell size d and the applied shear stress τ (or the applied nominal stress, assuming $\sigma = M\tau$ where M is the average orientation factor) acting on the dislocations should exist.

The results of this study on 4340 steel support these contentions. A shrinking of the average dislocation cell size with increasing applied strain is seen in Figures 4.21(a-c) in all the steels. A quantitative description of the relationship between cell size d and flow stress σ in Fig. 4.22(a-c) shows that an inverse dependence is also obeyed, namely

$$d = \frac{C}{(\sigma-\sigma_0)} \qquad (5.1)$$

The constants C and σ_0 are given in Table 4.5 and vary only slightly amongst the steels, allowing for experimental error. It is apparent from Fig. 4.22(a-c) that the different proeutectoid ferrite grain size of the three steels has little influence on the flow stress, and therefore in accordance with eqn. (5.1), has little effect on the average cell size.

It thus seems that the principle of similitude, which is found to apply to a wide range of pure, single phase metals, is also obeyed in a complex, two phase steel. However, similitude seems to fall apart for large strains in this material, as the cell size reaches a near constant value in Fig. 4.21(a-c) despite further increases in stress. It has been theoretically suggested by Kuhlmann-Wilsdorf [32-34] that the break-down of similitude when cell subdivision ceases is related to the initiation of mechanical instability of the cell structure and a transition to a new stage of hardening at higher stress levels. This is experimentally supported by the observations of a limiting cell size at the onset of stage III work hardening in aluminum [46] and an HSLA steel [47]. The attainment of a nearly constant cell size along with the start of substructural changes in the steel presently studied are also in general agreement with the theoretical explanation. In the studies of aluminum and steel, the limiting cell sizes were found to be 1.8 μm and 0.4 μm, respectively, compared with the value of 0.2-0.3 μm found for the steel in the present study. According to eqn. (5.1), the smaller limiting cell size in this steel is likely due to the attainment of a higher flow stress during deformation.

5.1.4 Hierarchical Cell Formation

In considering the problem of how an existing dislocation cell pattern could shrink in response to an increasing applied stress, it was suggested that cells subdivide by a tangling of glide dislocations within existing cells to nucleate new cell walls [34]. In this

way, the cell pattern decreases in scale but remains otherwise geometrically similar to itself. This results in a "cell hierarchy" as older cells are replaced by newer ones through subdivision. This mechanism of cell subdivision in 4340 steel is clearly illustrated in Fig. 4.15 where an existing large cell is being subdivided into at least four new cells, thereby decreasing its size by a factor of two. The new cell walls are thinner and presumably of lower dislocation density, but a definite misorientation (inferred from the change in contrast) across the walls indicates that the structure maintains its LEDS character in accordance with energy minimization principles. These observations are in general agreement with the hierarchical cell structure discussed by Hansen and Kuhlmann-Wilsdorf [123] and experimentally reported by others [46,125].

Interestingly, Kuhlmann-Wilsdorf suggests that when cells become so small that chance encounters between glide dislocations in cell interiors are rare, no new cell walls can be nucleated and cell subdivision ceases [34]. This would account for the observation of a limiting cell size and a general lack of dislocations in cell interiors at larger strains. In the steel of the present study, a limiting cell size at larger strains coincides with changes in substructural evolution and work hardening behaviour. These aspects are further discussed in the next section.

5.1.5 Large Strain Behaviour

At large strains in excess of $\varepsilon \cong 0.50$, the microstructural observations made by TEM and the general appearance of the flow curve suggest a transitional work hardening behaviour in 4340 steel. In localized regions of some TEM samples, subgrains and microbands are interspersed with the usual cell structure as shown, for example, in Fig. 4.16. The morphology of subgrains is characterized by very sharp, tight boundaries enclosing elongated, nearly dislocation-free interiors, strikingly different from the more equiaxed, thicker-walled cell structure. The elongated morphology of the subgrains, similar to that observed in drawn iron wire [48], may be a direct consequence of the

geometrical constraints imposed on the deforming material by necking. Subgrains are normally associated with higher misorientations across their boundaries than in cells.

The initial occurrence of subgrains, observed only for $\varepsilon>0.50$ in steels A and D, coincides with the attainment of a limiting cell size in these steels which as previously shown is related to the break down of similitude. Macroscopically, the flow curves shown in Fig. 4.21(a,b) level off, indicating a lower work hardening rate in association with the mixed dislocation cell-subgrain microstructure. These observations concur with other experimental studies which indicate a transition from cells to subgrains with increasing plastic strain during rolling [50,52,61], tensile straining [62], torsion [63], and wear [58].

Theoretically, it has been suggested that the conversion of cells to subgrains is related to the attainment of a high or critical dislocation density in the cell walls at which a dynamic recovery mechanism becomes dominant [6,45,66]. By this mechanism, a rearrangement and annihilation of dislocations reduces the internal stress and strain energy associated with the walls, converting them to the more sharply defined sub-boundaries typical of recovered structures. As mentioned earlier, this softening mechanism has been correlated with a lower rate of work hardening rate in both stage III [5] and stage IV [65,67]. In the material presently studied, the observations of a mixed cell-subgrain structure, a very low work hardening rate, and the cessation of similitude strongly suggest a transition to a new work hardening stage at large strains. However, a determination of the exact nature of this stage is precluded by the onset of tensile fracture in this investigation.

In summary, it appears that many of the aspects of the mesh length hardening theory, including cell evolution, similitude, and hierarchical cell division, are applicable to the complex alloy steel presently studied. However, mesh length theory is seemingly unable to account for the majority of hardening which occurs at lower strains in the material. It is now apparent that a complete description of the strength and work hardening

properties of this material requires an understanding of the relative contributions from all of the microstructural constituents involved in the strengthening process. This aspect is considered in the next section of this discussion.

5.2 Strengthening Mechanisms in 4340 Steel

5.2.1 Introduction

In this section, an attempt is made to characterize the strengthening mechanisms in 4340 steel from a microstructural viewpoint. At the most fundamental level, the strength of metals is inversely proportional to the mobility of dislocations during deformation. In multi-phase steels, however, the dislocation mobility is affected by solid solution alloy additions, the size and distribution of ferrite grains and pearlite colonies, the distribution and morphology of particles and inclusions, and the presence of well-developed dislocation substructures, altogether adding considerable complexity to the overall strengthening effect. A complete characterization of the microstructural factors contributing to the mechanical properties of the material is an onerous task, well beyond the scope of the present study. The approach taken here is to relate the key microstructural parameters characterized by optical and electron microscopy to the mechanical properties of 4340 steel indicated by tensile and microhardness tests.

A useful, quantitative measure of the dislocation mobility is given by the mean free path in the ferrite, or λ_α. This parameter has been related to the flow stress in two-phase steels by the empirical relationship

$$\sigma = \sigma_o + k(\lambda_\alpha)^{-c} \tag{5.2}$$

where σ represents the yield or flow stress, λ_α can be related to grain size, pearlite interlamellar spacing, dislocation cell size, etc., and σ_o, k, and c are constants which depend on the material and type of structural boundary. This type of equation has been

used to predict the yield and flow stresses for a variety of steel microstructures [126-128] and will prove helpful in later discussions of the structure-property relationship in 4340 steel.

5.2.2 Overview of Work Hardening Characteristics

As mentioned earlier, the flow properties of the three steels were found to be quite similar as evident in the true stress-true strain curves in Fig. 4.5. Hence, for the sake of simplicity , the three flow curves have been averaged and plotted as a single curve in Figure 5.1, with the corresponding fracture points labelled for each steel. With the addition of the characteristic substructural features recorded by TEM, the figure illustrates that the flow curve of the steel may be separated into two distinct stages of work hardening.

The first stage (1) represents the portion of the curve from yielding until a plastic strain of 0.10-0.15, which roughly corresponds to the true tensile strength σ_{UTS}. "Stage 1" is characterized by a rapid increase in flow stress due to a high, nearly linear work hardening rate. This corresponds with substructural observations of large numbers of dislocation loops, dipoles, and tangles in the ferrite phase reflecting an increasing rate of dislocation generation and interaction. The observation that the Fe_3C (cementite) platelets remain visibly undeformed suggests that the lack of cells in this stage is attributed to the reduction of dislocation mobility (and thus plastic strain) by the rigid platelets, which is supported by the micrograph in Fig. 4.17(b).

The second part of the flow curve in Fig. 5.1 from strains of 0.10-0.15 up to fracture represents a stage of decreasing work hardening rate as the flow stress tends towards an upper, limiting value. This "stage 2" is microscopically characterized by the rapid formation and refinement of a dislocation cell structure in the ferrite phase. The onset of well defined cells in ferrite grains coincides with initial evidence for the deformation of the cementite phase at about the ultimate tensile strength, whereas cells in pearlitic ferrite are associated with a larger scale deformation and separation of Fe_3C platelets at higher strains

of 0.25-0.30 in the material. Examples of the cell structures found in the different ferrite regions in stage 2 are shown in Figures 4.11-4.13 and 4.17(d).

At higher strains greater than about 0.50, a transitional behaviour within stage 2 is suggested by the observations of a non-varying cell size and localized subgrain and microband formation. These substructural changes may be associated with a mechanically activated recovery process occurring at higher stresses.

It is apparent that the two work hardening stages in Fig. 5.1 reflect the individual strengthening contributions from a two-phase composite of ferrite and cementite. Stage 1 is controlled by strengthening due to the cementite phase in pearlite, while stage 2 strengthening is largely due to cell mechanisms in the ferrite phase. This is more clearly understood by considering the mechanical behaviour of the individual phases during uniaxial deformation.

During a tensile test, the crosshead moves at a constant rate, so the displacement (or strain) is imposed on the specimen. Since the two phases are closely intermeshed, the plastic strain will be about the same in each phase, differing only in the elastic strain. However, the stress (σ_1) in the harder, less ductile Fe_3C will be much higher than the stress (σ_2) in the softer ferrite for the same strain as illustrated in Figure 5.2. The nominal stress (σ_{avg}) in the alloy will be some weighted average of the two stresses assuming constant strain,

$$\sigma_{avg} = f_1\sigma_1 + f_2\sigma_2 \qquad (5.3)$$

where f_1 and f_2 are functions of the volume fractions of the two phases. Thus, pearlite, strengthened by the cementite phase and occupying ~ 60% of the total volume fraction will largely dictate the overall stress in the material in stage 1. When the Fe_3C platelets begin to break at the onset of stage 2, the redistribution of load from cementite to the softer ferrite phase increases the stress in this phase (σ_2-->σ_{avg} in Fig. 5.2). This

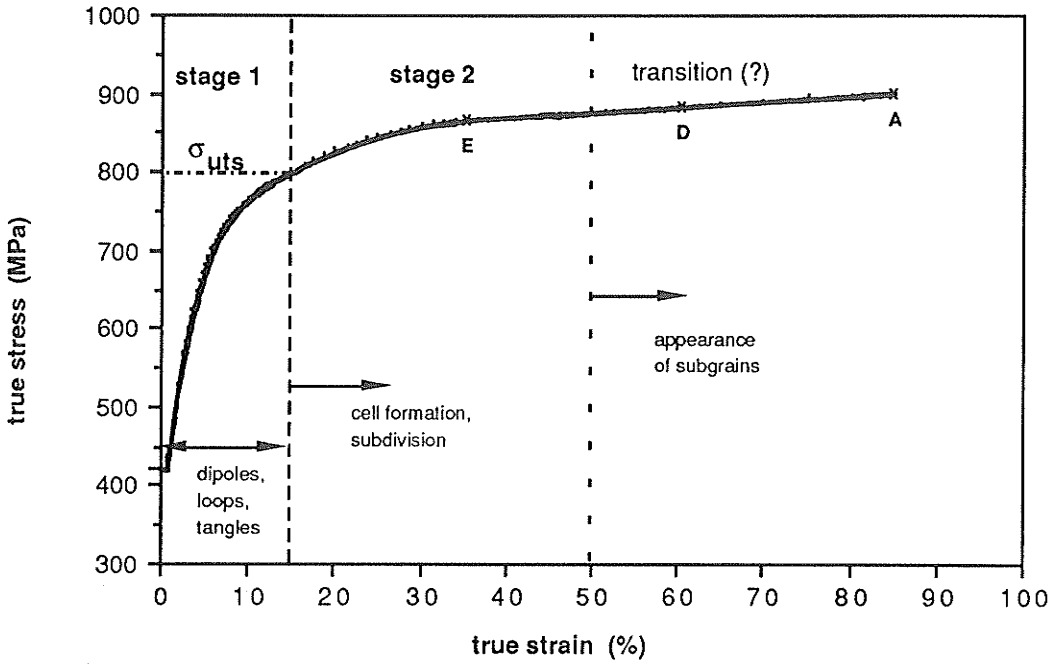

Figure 5.1 Stages of work hardening in 4340 steel

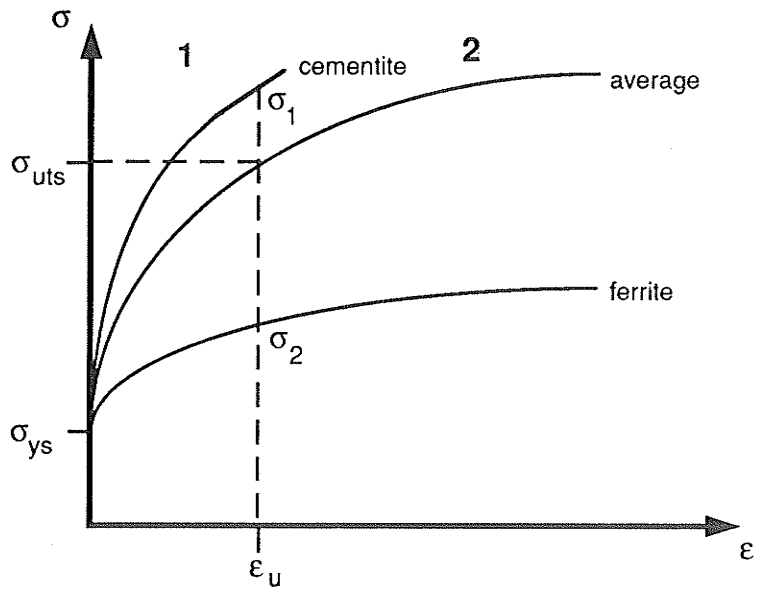

Figure 5.2 Stress-strain distribution in a two-phase material assuming constant strain

results in large increases in plastic strain which cause cell evolution in the necked region of the tensile specimen. The increase in flow stress in stage 2 will be largely due to dislocation interactions associated with the well-developed cell structure in ferrite.

Thus it appears that the overall work hardening behaviour of this material reflects the relative contributions from three microstructural components, which vary in importance as deformation proceeds. In a simplified functional form;

$$\sigma_{tot} = f_1(\varepsilon)\sigma_p + f_2(\varepsilon)\sigma_\alpha + f_3(\varepsilon)\sigma_{gb} \qquad (5.4)$$

where $f_1(\varepsilon)$, $f_2(\varepsilon)$, and $f_3(\varepsilon)$ are functions of the applied strain, and σ_p, σ_α, and σ_{gb} represent the strength contributions from pearlite, ferrite, and ferrite grain boundaries, respectively. In the following sections, a more quantitative assessment of the three strengthening components in eqn. (5.4) is made in light of the two stage flow curve presented here. The relationship between the mean free path in ferrite and flow stress given by eqn. (5.2) is used to relate the strengthening effect to dislocation mobility.

5.2.3 Stage 1 Strengthening Controlled by Pearlite

As mentioned earlier, stage 1 refers to the hardening range from the yield point up to strains of 0.10-0.15 as shown in Fig. 5.1. TEM micrographs taken in this range of plastic strain show that deformation of the steel is accomodated by multiple slip in both the proeutectoid ferrite grains and the ferrite lamellae in pearlite. The interaction of glide dislocations with cementite platelets and grain boundaries, as well as with particles and other dislocations, causes tangling and dipole formation and gives rise to the large increase in flow stress observed in this stage. Elastic stresses due to the fiber loading component in Fe_3C also contribute somewhat to the overall stress in the material. According to eqn. (5.2), the largest flow stress contribution derives from the structural unit associated with the smallest mean free ferrite path, which is presently determined by the interlamellar

spacing in pearlite. The dependence of flow stress on the pearlite interlamellar spacing (S_p) can be expressed by eqn (5.2), replacing λ_α with S_p to give

$$\sigma = \sigma_o + k(S_p)^{-c} \tag{5.5}$$

where σ_o and k are constants for a given strain. The value of c is usually found as either 1/2 [129] or 1 [81] and is theoretically explained in terms of either dislocation pile-up or dislocation source models of the ferrite-cementite interfaces. In the present study, the pearlite interlamellar spacing was found to be invariant in the three steels (refer to Table 4.1), and in accordance with eqn. (5.5), the flow curves are nearly identical as evident in Fig. 4.5.

The point of transition from stage 1 to stage 2 coincides macroscopically with the true tensile strength (775-790 MPa) and microscopically with the initiation of shear of the Fe_3C lamellae in the material. As shown in Fig. 4.17(c), the structure of pearlite at this point shows localized bending and fragmentation of Fe_3C plates as well as an inhomogeneous arrangement of dislocations into slip bands in ferrite. From these observations, it is suggested that at stresses near the tensile strength of the material (σ_{UTS}), localized shear in the ferrite initiates separation of the adjacent Fe_3C plates which allows the propagation of slip through this phase. This is supported by other experimental studies which showed that the deformation of Fe_3C is microscopically correlated with inhomogeneous shear in the ferrite lamellae [78,79,81]. The resultant increase in dislocation mobility in the ferrite brings about the larger plastic strain and cell evolution associated with stage 2.

Dollar et. al. [81] have modelled the cracking of a Fe_3C plate in terms of the shear stress generated by dislocations piled-up against the plate, assuming that the pile-up length is approximately equal to the pearlite interlamellar spacing, S_p. From their analysis, the effective cracking shear stress is given by

$$\tau_E = \frac{4.55}{\sqrt{S_p}} \text{ MPa} \qquad (5.6)$$

Assuming an orientation factor M = 3.0 for BCC polycrystals, eqn. (5.6) is equivalent to a macroscopic tensile stress of

$$\sigma_E = \frac{13.65}{\sqrt{S_p}} \text{ MPa} \qquad (5.7)$$

with S_p given in mm. For the average value of S_p = 0.3 μm determined for steels in this study, σ_E = 788 MPa which corresponds quite closely with the experimentally determined value of σ_{UTS} = 773-790 MPa. This good agreement may be coincidental, but when coupled with the TEM observations it tends to support the notion that the ultimate tensile strength, and thus the onset of stage 2 in the material, is controlled by the pearlite interlamellar spacing which determines the stress required to shear the Fe_3C platelets in pearlite.

5.2.4 Stage 2 Strengthening Controlled by Cell Mechanisms in Ferrite

Stage 2 is the work hardening range extending from the ultimate tensile strength to fracture and characterized by a decreasing rate of strain hardening, as shown in Fig 5.1. Necking in this stage causes high, localized plastic strain as well as the rapid development of dislocation cells in the ferrite phase. Well-developed cells in ferrite grains mark the onset of stage 2 at strains of $\varepsilon \cong 0.10\text{-}0.15$, while cell formation in interlamellar ferrite is delayed until larger strains of $\varepsilon \cong 0.25\text{-}0.30$. This may be attributed to the smaller initial cells restricted by Fe_3C plates in pearlite, and the inverse dependence of cell size on flow stress. Since the flow stress associated with the smaller cell size in pearlite is higher than for the larger cells initially formed in ferrite grains, the cells in pearlite form at a later stage.

The observation that the initial cells in pearlite are equivalent in size to cells in ferrite grains indicates that the stress becomes uniformly distributed throughout the ferrite phase.

Quantitative measurements in stage 2 indicate that dislocation cells are the substructural units determining the mean free path in ferrite and thus controlling strengthening in the material. An inverse dependence of flow stress on dislocation cell size was found and is empirically expressed by eqn. (5.2), replacing λ_α with d and setting c = 1 to give

$$\sigma = \sigma_o + C(d)^{-1} \tag{5.8}$$

The constants σ_o and C, as determined from regression analysis in Table 4.5, varied from 735-756 (MPa) and 28-40 (MPa.μm), respectively, for the steel groups in this study. An inverse dependence between flow stress and substructural size is supported by a number of investigations on iron-based alloys compiled by Young and Sherby [83] as well as studies on non-ferrous metals [44-46].

A comparison of the relative strengthening effect from cells in 4340 steel and in drawn iron wire investigated by Langford and Cohen [48] is revealing at this point. To facilitate comparison of the results, eqn. (5.8) may be rewritten in a form comparable with eqn (2.5) (refer to sec. 2.6) by replacing the constant C with the quantity kGb to obtain

$$\sigma = \sigma_o + kGb(d)^{-1} \quad \text{MPa} \tag{5.9}$$

With the shear modulus G = 75,800 MPa and the burgers vector b = 2.48×10^{-4} μm, the dimensionless constant k (related to the sub-boundary strength) varies from 1.5 to 2.1 for this steel. The cell size-flow stress data of the present study has been plotted along with the data from Langford and Cohen's study in Figure 5.3. Both data sets show the linear dependence between flow stress and inverse cell size as given by eqn. (5.9), but both

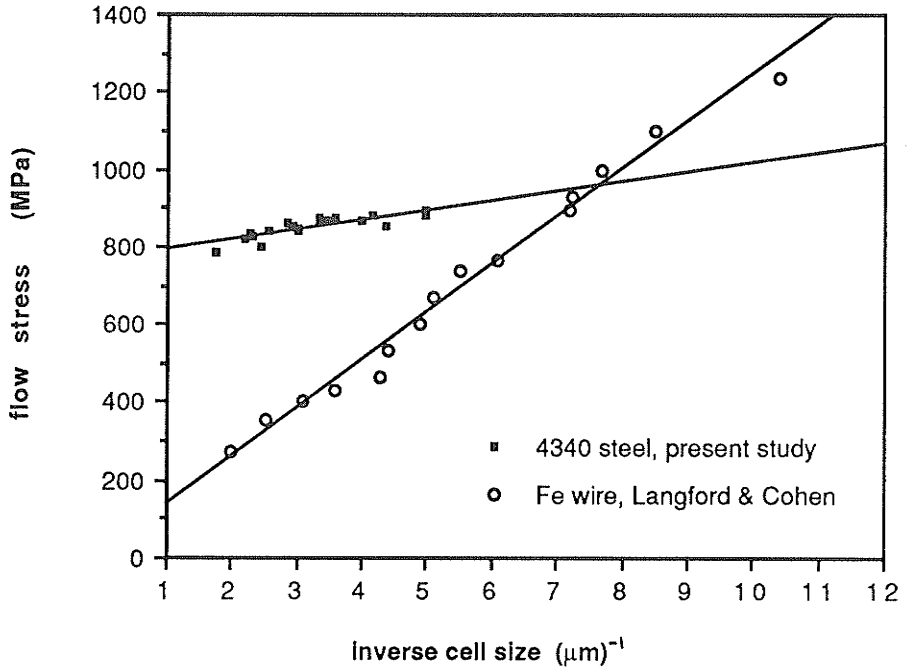

Figure 5.3 Combined plot of flow stress vs inverse cell size for data for 4340 steel and data for drawn Fe-wire (from ref. 48)

the intercept (σ_0) and the slope (proportional to k) are quite different for the two cases. The low alloy steel has a high initial stress, σ_0 = 735-756 MPa (corresponding to the stress at which cells first become established), and shows only a mild dependence on cell size (k = 1.5-2.1). The high-purity drawn iron on the other hand, has a lower initial stress of σ_0 = 33 MPa and exhibits a stronger flow stress dependence with k = 5.9. A lower value of k = 2.7 has been reported for drawn Fe-Ti alloy by Rack and Cohen [49] with the suggestion that k is strongly influenced by the alloy content. However, it is likely that the small value of k and large value of σ_0 reflect the dominant contribution from pearlite to the overall flow stress in the material. As shown in Fig. 5.2, the flow stress in the ferrite would have increased from a much lower value at the start of stage 2 cell formation, as compared with the average measured flow stress. Thus for 4340 steel, eqn. (5.9) does not express the flow stress dependence of cells in ferrite as such (since the true variation in flow stress in the ferrite is unknown), and therefore does not allow for a meaningful comparison to be made with the results for drawn high-purity iron. This emphasizes the secondary importance of cell mechanisms to the overall strengthening characteristics of 4340 steel.

As mentioned earlier, at larger strains of $\sim\varepsilon > 0.50$, a transitional behaviour arises when the cell size reaches a nearly constant value and the inverse dependence of cell size on flow stress given by eqn. (5.8) breaks down. This transition was related to the onset of subgrain formation by a cell wall "recovery mechanism" activated at higher stresses. Many investigators have reported a transitional strengthening behaviour associated with the onset of subgrain formation, whereby the dependence of flow stress on substructural size follows eqn. (5.8) but with the exponent changing from 1 to 1/2 [6,83,84]. The rationale behind this argument is that the increased misorientation and boundary perfection of subgrains are characteristic of high angle grains. Such a change in the exponent in eqn. (5.8) could not verified in this work due to the onset of tensile instability and fracture associated with the transition point.

5.2.5 Role of the Proeutectoid Ferrite Grain Size

The results of the present investigation show that the size of the proeutectoid ferrite grains affects the yielding and ductility properties, but has no apparent influence in the work hardening characteristics of 4340 alloy.

In terms of the yield properties, a Hall-Petch dependence of the yield stress, σ_{ys}, on the ferrite grain size, L_α, was observed as given by eqn. (5.2) with the mean free ferrite path λ_α replaced with L_α and the exponent c = 1/2 as shown in Fig. 4.7. This dependence did not extend beyond yielding however, as reflected in the similar flow curves for the three steels shown in Fig. 4.5. As mentioned in previous sections, work hardening during stages 1 and 2 is associated with dislocation activity in the ferrite phase, with the cementite lamellae and the dislocation cells acting as the smallest structural units controlling the mean slip distance in ferrite ($\sim\lambda_\alpha$) and thereby contributing the most to strengthening according to eqn. (5.2).

In terms of the increased dislocation activity associated with grain boundaries as discussed in section 2.3, it was expected that a smaller proeutectoid ferrite grain size (and therefore a larger grain boundary area) would contribute to a higher dislocation density at a given plastic strain, resulting in smaller cell sizes in stage 2. Such a dependence of cell size on grain size has been reported elsewhere for polycrystalline copper [62] and aluminum [51]. However, as shown in Fig. 4.20, there is no apparent grain size dependence of cells for the steel groups investigated in this study. This is likely due to the relatively mild variation in the proeutectoid ferrite grain size amongst the sample groups (L_α = 3.8-10.8 μm in Table 4.1), as well as the influence of the pearlite constituent, which comprises 60 % of the material, in the process of cell evolution.

It should be noted that the TEM observations in this study indicate that the ferrite grain boundaries appear to be preferential sites for cell nucleation, as illustrated in the micrograph of Fig. 4.14, for example. Similar observations of preferential cell formation along existing grain boundaries have been recorded by Bay and Hansen for rolled

aluminum [51]. From an energetic viewpoint, it would seem that it is more favourable to form cells in this manner due to the high internal stresses and strain energy associated with grain boundaries during deformation. It is expected that this argument would also apply to the pearlite colony boundaries, although no direct TEM evidence of preferred cell formation along these boundaries was found.

5.3 Ductile Fracture Mechanisms in 4340 Steel

5.3.1 Introduction

As stated in an earlier section, ductile fracture occurs by a process of void initiation, growth, and coalescence, generally after an appreciable degree of plastic deformation. Void nucleation is associated with sites of highly localized deformation, such as second phase particles and inclusions. Thus, the ductility of metals has often been found to correlate well with the volume fraction of particles. In metals with a low particle content though, voids can form solely as a result of inhomogeneous arrangements of dislocations as typified by shear bands and dislocation cells.

In this section, the fracture surface observations recorded by SEM are related to the possible microstructural sites, as characterized by optical and electron microscopy, of localized deformation and void initiation in 4340 steel. The fracture mechanisms occurring in ferrite grains and pearlite colonies are considered separately due to the composite nature of the microstructure as shown earlier.

5.3.2 Void Initiation in Ferrite Grains

Results of the SEM analysis of tensile fracture surfaces show that a fine distribution of voids form in ferrite grains, as illustrated in the micrographs in Fig. 4.24(a-c). The general absence of void-nucleating particles or inclusions in these micrographs follows from the very low volume fraction of inclusions determined for this steel by metallography

(refer to Table 4.2). The similar distribution of void sizes in Fig 4.25(a-c) indicates that voids formed by the same mechanism in the three steels. The majority of voids are less than 1 μm in size, which is three orders of magnitude smaller than the interparticle spacing (λ_i) given in Table 4.2. The voids associated with the few particles observed were much larger than the average void size, as illustrated in Fig. 4.27 for example. From these results, it can be concluded that inclusions are not sites for microcrack propagation by void coalescence in this steel. Inclusions and particles may contribute to a lower overall ductility by initiating voids at lower strains, but they do not participate in the final fracture process.

Eliminating inclusions from the microscopic fracture picture, it becomes evident that dislocation cell walls are the preferred paths for microcrack propagation by void mechanisms. A close correlation is found between the average dislocation cell size at large strains close to fracture and the distribution of void sizes on the tensile fracture surfaces. The minimum size attained by cells before the onset of fracture is about 0.2-0.3 μm, which is within the same order of magnitude of the void sizes, which are concentrated in the range of 0.5-1.0 μm. Similar correlations between void distributions and dislocation cell sizes have been found in another low carbon steel [130], and in an HSLA steel [131]. This is further supported by a series of in-situ HVEM (High Voltage Electron Microscopy) experiments by Wilsdorf and co-workers [106-109] which dynamically recorded microcrack propagation along existing cell wall structures in a number of pure metals. Wilsdorf has suggested that cell walls are preferred sites (in the absence of particles) for void initiation since the strain energy associated with a wall aids in overcoming the surface energy required to nucleate a void [106].

There is some evidence in the present work that void nucleation may be controlled by the dislocation density in the cell walls. It is possible that as deformation proceeds, the dislocation density in the walls reaches a critical value for which the associated strain energy is high enough to nucleate voids in accordance with Wilsdorf's model. Since the dislocation density can be related to flow stress according to eqn. 2.3 (refer to sec. 2.6),

this would explain the similar fracture stress observed for all the three steels (as indicated in Table 4.3).

5.3.3 The Fracture Process in Pearlite

It has been shown earlier that the fracture of pearlite is microscopically associated with cracks running normal to cementite lamellae and shallow microvoids in the interlamellar ferrite as typified by the SEM micrographs of Fig. 4.26(a-c). The fracture topography reflects the inhomogeneous plastic deformation mechanisms occurring in pearlite, as was revealed by the TEM investigation. There, it was observed that the separation of hard cementite plates is associated with localized shear in the ferrite, as shown in Fig. 4.17(c). However, this event is macroscopically correlated with the ultimate tensile strength of the alloy and does not signal the onset of void formation and fracture. Instead, the fragmentation of Fe_3C platelets is accomodated by increased deformation and cell formation in the ferrite lamellae.

Based on a detailed study of a series of steels containing pearlite, Miller and Smith [132] have suggested a mechanism for the fracture of pearlite which helps to explain the observations recorded in the present work. In their model, as depicted in Fig. 5.4 (a-d), cracking occurs at a cementite plate under the combined influence of applied tensile stress and localized shear in the ferrite lamellae (Fig. 5.4a). Deformation becomes concentrated in a shear band (Fig. 5.4b), causing cracking of adjacent Fe_3C plates and leading to void growth and coalescence (Fig. 5.4 c,d). The final ductile fracture surface then consists of shallow dimples between the broken cementite plates. This is strikingly similar to the fracture topography of a pearlite colony in the steel of the present study as shown in Fig. 4.26(c). It is thus expected that void formation and microcracking are initiated in pearlite colonies which are most closely aligned with the tensile axis of the specimen. In those colonies oriented such that the tensile stresses on the Fe_3C plates are low, the tendency for void formation is reduced and the fracture process will be delayed even though the plates

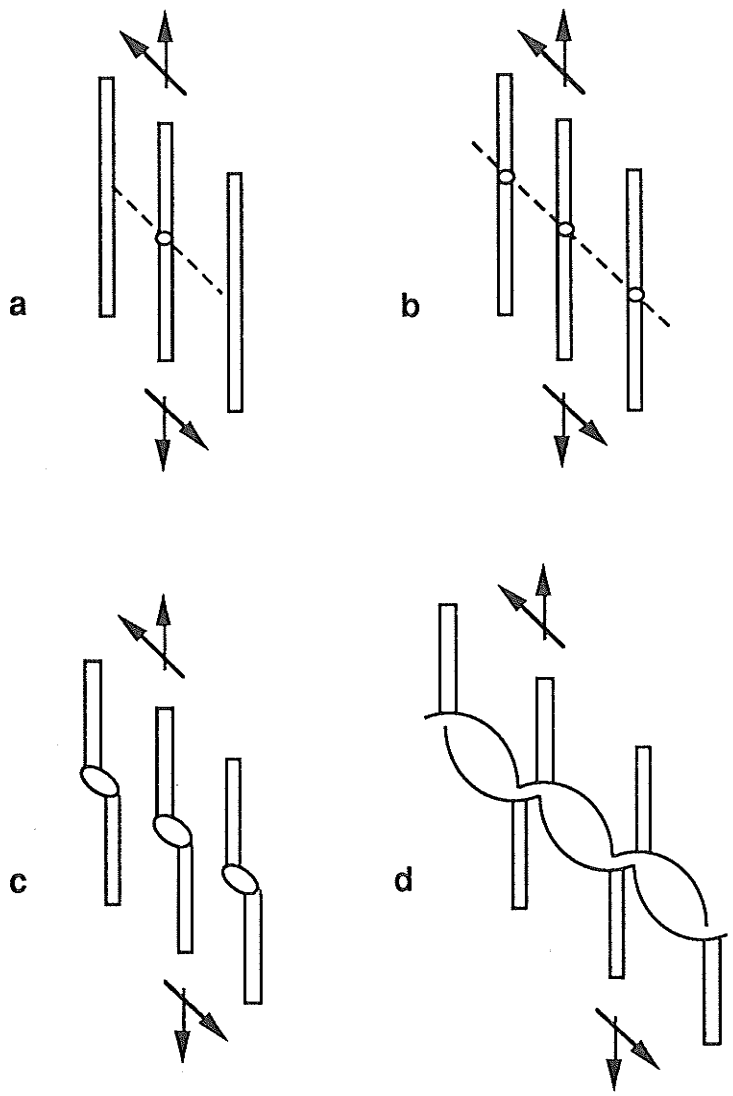

Figure 5.4 Fracture mechanism for pearlite: (a) cracking of a cementite plate, (b) shear zone developing in ferrite causing cracking of adjacent plates, (c) and (d) void formation and coalescence (after ref. 132)

may be fragmented due to shear processes in ferrite. This emphasizes the requirement of both applied tensile stress and localized shear to initiate void formation by the cracking of Fe_3C plates.

These results form a picture of the ductile fracture process in 4340 steel. Microcracks nucleated in pearlite by the mechanism just described propagate through the colonies and encounter softer ferrite grains. Crack propagation through the ferrite grains occurs by void initiation and coalescence at the dislocation cell walls, leading to the ductile fracture of the material. The present investigation thus shows the importance of inhomogeneous plastic deformation processes to the initiation of ductile fracture. As well, the combined use of SEM and TEM techniques is necessary for a full understanding of the micro-mechanisms of ductile fracture in materials.

Chapter VI

CONCLUSIONS

The strengthening mechanisms arising from the development of a dislocation substructure in annealed AISI 4340 steel during uniaxial deformation have been investigated. Also, the influence of a well-developed substructure and the role of microstructure in the ductile fracture process were studied.

The results of macroscopic tensile testing show that the yielding behaviour of this steel is sensitive to the proeutectoid ferrite grain size. In particular, it was found that the dependence of yield strength on grain size can be expressed by a Hall-Petch type of relationship for grain sizes in the range of 4-11 μm. In contrast, the work hardening and flow properties of the steel are not influenced by the ferrite grain size.

Based on the flow behaviour determined by mechanical testing and the substructural changes revealed by TEM, the flow curve of the steel can be divided into two distinct stages. The first stage (1) comprises the largest part of the strength of the material, extending from the yield stress to the ultimate stress. Microscopically, it was found that the work hardening behaviour in this stage is largely controlled by strengthening mechanisms in pearlite, where the cementite platelets act as rigid barriers to dislocation motion in the ferrite lamellae. The transition to stage 2 occurs when the platelets begin to shear by dislocation activity in the ferrite lamellae at stresses near the ultimate tensile strength. Using a relationship proposed previously for the nominal stress required to shear Fe_3C platelets of a given spacing, it was determined that for a pearlite interlamellar spacing of 0.3 μm in the steel of this study, the nominal stress is 788 MPa, which is in close agreement with the experimentally measured values of the tensile strength. This result indicates that the ultimate tensile strength and the onset of stage 2 flow behaviour is controlled by the pearlite interlamellar spacing in the steel.

The increased dislocation mobility due to the shearing of Fe_3C platelets results in larger plastic strains, and the formation and refinement of dislocation cells in the ferrite phase during stage 2. Many aspects of this cell evolution, such as hierarchical cell formation and similitude, were observed to be in agreement with the "mesh length" theory of work hardening which provides a theoretical basis for the occurrence of cells during plastic deformation. It was found that an inverse, linear strengthening relationship between cell size and flow stress is obeyed during stage 2, although the strengthening contribution from cells is small relative to the overall strength of the material. The occurrence of subgrains in conjunction with a very low rate of work hardening at large strains indicate a possible transition to a new stage of plastic deformation, although the exact nature of this stage could not be evaluated due to the onset of fracture in the material.

The combined TEM and SEM results suggest that the ductile fracture process is associated with microcrack initiation at cementite platelets in pearlite under the combined influence of tensile loading and localized shear in the adjacent ferrite. The distribution of void sizes measured from SEM micrographs indicate that microcracks propagate through the ferrite grains by the nucleation and coalescence of voids along well-developed dislocation cell walls.

This work has extended the study of substructural strengthening to a commercially-important, low alloy steel. The result is a greater understanding of the role of both microstructure and dislocation substructure in the processes of plastic deformation and fracture.

REFERENCES

1. D. McLean, "Mechanical Properties of Metals", 2nd ed., J. Wiley and Sons, Inc., New York, 1977.

2. G.E. Dieter, "Mechanical Metallurgy", 2nd ed., McGraw-Hill Inc., New York, 1976.

3. R.E. Smallman, "Modern Physical Metallurgy", 4th ed., Butterworth and Co. Ltd., London, 1985.

4. D. Hull and D.J. Bacon, "Introduction to Dislocations", 3rd ed., Pergamon Press Ltd., Oxford, 1984.

5. K. Lucke and H. Mecking, "The Inhomogeneity of Plastic Deformation", ASM, Metals Park, Ohio, 1973, p. 223.

6. J. Gil Sevillano, P. van Houtte, and E. Aernoudt, Prog. Mater. Sci., 25 (1980) 69.

7. J. Gil Sevillano and E. Aernoudt, Mater. Sci. Eng., 86 (1987) 35.

8. A.D. Rollett, U.F. Kocks, J.D. Embury, M.G. Stout, and R.D. Doherty, in P.O. Kettunen, T.K. Lepisto, and M.E. Lehtonen (eds.), "Proc. 8th Int. Conf. on the Strength of Metals and Alloys, Tampere, August 22-26, 1988", Pergamon, Oxford, 1988, p. 433.

9. U.F. Kocks, Acta Metall., 6 (1958) 85.

10. E.O. Hall, Proc. Phys. Soc. B., 643 (1951) 747.

11. N.J. Petch, J. Iron Steel Inst., 173 (1953) 25.

12. R.W. Armstrong, Metall. Trans., 1 (1970) 1169.

13. J.P. Hirth, Metall. Trans., 3 (1972) 3047.

14. J.C.M. Li and Y.T. Chou, Metall. Trans., 1 (1970) 1145.

15. J.C.M. Li, Trans. Metall. Soc. AIME, 227 (1963) 239.

16. A.W. Thompson, M.F. Baskes, and W.F. Flanagan, Acta Metall., 21 (1973) 1017.

17. A.W. Thompson, in A.W. Thompson (ed.), "Work Hardening In Tension and Fatigue", Trans. Metall. Soc. AIME, New York, 1977, p. 89.

18. H. Mecking,in A. Horsewell, T. Leffers, and H. Lilholt (eds.), "Deformation of Polycrystals: Mechanisms and Microstructures, Proc. 2nd Riso Int. Symp. on Metallurgy and Materials Science, September 14-18, 1981", Riso National Laboratory, Riso, 1981, p. 73.

19. M.F. Ashby, Phil. Mag., 21 (1970) 399.

20. S. Sangal and K. Tangri, Metall. Trans. A, (1989) in press.

21. N. Hansen and B. Ralph, Acta Metall., 30 (1982) 411.

22. B.P. Kashyap, K. McTaggart, and K. Tangri, Phil. Mag. A, 57 (1988) 97.

23. F.R.N. Nabarro, Z.S. Basinski, and D.B. Holt, Adv. Phys., 13 (1964) 193.

24. P.B. Hirsch and T.E. Mitchell, Can. J. Phys., 45 (1967) 663.

25. A.S. Keh and S. Weissmann, in G. Thomas and J. Washburn (eds.), "Electron Microscopy and Strength of Crystals", Wiley-Interscience, New York, 1963, p. 231.

26. W. Carrington, K.F. Hale, and D. McLean, Proc. Roy. Soc. A, 259 (1960) 203.

27. P.R. Swann, in G. Thomas and J. Washburn (eds.), "Electron Microscopy and Strength of Crystals", Wiley-Interscience, New York, 1963, p. 131.

28. J.J. Jonas, C.M. Sellars, and W.J. McG. Tegart, Met. Rev., 14 (1969)1.

29. J.E. Bailey and P.B. Hirsch, Phil. Mag., 5 (1960) 485.

30. R.J. McElroy and Z.C. Szkopiak, Int. Metall. Rev., 17 (1972) 175.

31. D.L. Holt, J. Appl. Phys., 41 (1970) 3197.

32. D. Kuhlmann-Wilsdorf, Trans. Metall. Soc. AIME, 224 (1962) 1047.

33. D. Kuhlmann-Wilsdorf, in J.P. Hirth and J. Weertmann (eds.), "Work Hardening", Gordon and Breach, New York, 1968, p. 97.

34. D. Kuhlmann-Wilsdorf, in A.W. Thompson (ed.), "Work Hardening in Tension and Fatigue", Metall. Soc. AIME, New York, 1977, p. 1.

35. D. Kuhlmann-Wilsdorf and J.H. van der Merwe, Mater. Sci. Eng., 55 (1982) 79.

36. D. Kuhlmann-Wilsdorf, Mater. Sci. Eng., 86 (1987) 53.

37. M.N. Bassim and D. Kuhlmann-Wilsdorf, Cryst. Latt. Def., 4 (1973) 9.

38. M.N. Bassim and D. Kuhlmann-Wilsdorf, Phys. Status. Solidi (a), 16 (1973) 241, 17 (1973) 281;379, 19 (1973) 335.

39. A. Seeger, in J.C. Fisher, W.A. Johnston, R. Thompson, and T. Vreeland (eds.), "Dislocations and Mechanical Properties of Crystals", J. Wiley, New York, 1957, p. 243.

40. P.B. Hirsch, "Internal Stresses and Fatigue in Metals", Elsevier, New York, 1958, p. 139.

41. P.J. Jackson and D. Kuhlmann-Wilsdorf, Scr. Metall., 16 (1982) 105.

42. P.J. Jackson, Mater. Sci. Eng., 81 (1986) 169.

43. U.F. Kocks, Phil. Mag., 13 (1966) 541.

44. M.R. Staker and D.L. Holt, Acta Metall., 20 (1972) 569.

45. Y.J. Chang, A.J. Shume, and M.N. Bassim, Mater. Sci. Eng., A103 (1988) L1.

46. C.T. Young, T.J. Headley, and J.L. Lytton, Mater. Sci. Eng., 81 (1986) 391.

47. M.N. Bassim and R.J. Klassen, Mater. Sci. Eng., 81 (1986) 163.

48. G. Langford and M. Cohen, Trans. ASM, 62 (1969) 623.

49. H.J. Rack and M. Cohen, Mater. Sci. Eng., 6 (1970) 320.

50. D. Griffiths and J.N. Riley, Acta Metall., 14 (1966) 755.

51. B. Bay and N. Hansen, in A. Horsewell, T. Leffers, and H. Lilholt (eds.), "Deformation of Polycrystals: Mechanisms and Microstructures, Proc. 2nd Riso Int. Symp. on Metallurgy and Materials Science, September 14-18, 1981", Riso National Laboratory, Riso, 1981, p. 137.

52. J. Gil Sevillano and F.J. Torrealdea, in A. Horsewell, T. Leffers, and H. Lilholt (eds.), "Deformation of Polycrystals: Mechanisms and Microstructures, Proc. 2nd Riso Int. Symp. on Metallurgy and Materials Science, September 14-18, 1981", Riso National Laboratory, Riso, 1981, p. 185.

53. C.E. Feltner and C. Laird, Acta Metall., 15 (1967) 1633.

54. C. Laird, Metall. Trans. A, 8A (1977) 851.

55. C. Laird, P. Charsley, and H. Mughrabi, Mater. Sci. Eng., 81 (1986) 433.

56. H.J. McQueen, Metall. Trans. A, 8A (1977) 807.

57. L.J. Cuddy, Metall. Trans., 1 (1970) 395.

58. D.A. Rigney, M.G.S. Naylor, R. Divakar, and L.K. Ives, Mater. Sci. Eng., 81 (1986) 409.

59. "Proceedings of the International Conference on Low Energy Dislocation Structures", M.N. Bassim, W.A. Jesser, D. Kuhlmann-Wilsdorf, and H.G.F. Wilsdorf (eds.), Elsevier Sequoia, Lausanne, 1986; also, Mater. Sci. Eng., vol. 81, 1986.

60. J.D. Embury, A.S. Keh, and R.M. Fisher, Trans. AIME, 236 (1966) 1252

61. E. Nes, W.B. Hutchinson, and A.A. Ridha, in H.J. McQueen, J.P. Bailon, J.I. Dickson, J.J.Jonas, and M.G. Akben (eds.), "Proc. 7th Int. Conf. on the Strength of Metals and Alloys, Montreal, August 12-16, 1985", Pergamon, Oxford,1985, p. 57.

62. A.J. Shume, Y.J. Chang, and M.N. Bassim, Mater. Sci. Eng., A108 (1989) 241.

63. C.M. Young, L.J. Anderson, and O.D. Sherby, Metall. Trans., 5 (1974) 519.

64. D.J. Lloyd and D. Kenny, Scr. Metall., 12 (1978) 903.

65. D.J. Lloyd and D. Kenny, Acta Metall., 28 (1980) 639.

66. R.B. Nethercott, J.A. Retchford, and R.A. Coyle, in R.C. Gifkins (ed.), "Proc. 6th Int. Conf. on the Strength of Metals and Alloys, Melbourne, August 16-20, 1982", Pergamon, Oxford, 1982, p. 535.

67. U.F. Kocks, J. Eng. Mater. Technol., 98 (1976) 76.

68. C.Y.J. Barlow, B. Bay, and N. Hansen, Phil. Mag. A, 51 (1985) 253.

69. F.J. Torrealdea and J. Gil Sevillano, in R.C. Gifkins (ed.), "Proc. 6th Int. Conf. on the Strength of Metals and Alloys, Melbourne, August 16-20, 1982", Pergamon, Oxford, 1982, p. 547.

70. A.S. Malin and M. Hatherly, Metal Sci., 13 (1979) 463.

71. P.T. Wakefield and M. Hatherly, Metal Sci., 15 (1981) 109.

72. F.J. Humphreys and J.W. Martin, Phil. Mag., 16 (1967) 927.

73. J.W. Martin, "Micromechanisms in Particle-Hardened Alloys", Cambridge University Press, 1980.

74. M.F. Ashby, in A. Kelly and R.B. Nicholson (eds.), "Strengthening Methods in Crystals", Applied Science Publishers, London, 1971, p. 137.

75. B. Ralph and N. Hansen, in A. Horsewell, T. Leffers, and H. Lilholt (eds.), "Deformation of Polycrystals: Mechanisms and Microstructures, Proc. 2nd Riso Int. Symp. on Metallurgy and Materials Science, September 14-18, 1981", Riso National Laboratory, Riso, 1981, p. 473.

76. N. Hansen and B. Ralph, Acta Metall., 34 (1986) 1955.

77. D.J. Lloyd and D. Kenny, Acta Metall., 28 (1980) 639.

78. J.D. Embury and R.M. Fisher, Acta Metall., 14 (1966) 147.

79. G. Langford, Metall. Trans. A, 8A (1977) 861.

80. J. Gil Sevillano, Mater. Sci. Eng., 21 (1975) 221.

81. M. Dollar, I.M. Bernstein, and A.W. Thompson, Acta Metall., 36 (1988) 311.

82. G.I. Taylor, Proc. R. Soc. London, Ser. A, 145 (1934) 362.

83. C.M. Young and O.D. Sherby, J. Iron Steel Inst., 211 (1973) 640.

84. A.W. Thompson, Metall. Trans. A, 8A (1977) 833.

85. S.V. Raj and G.M. Pharr, Mater. Sci. Eng., 81 (1986) 217.

86. F. Hultgren, Trans. Met. Soc. AIME 230 (1964) 898.

87. Z.S. Basinski, Phil. Mag., 4 (1959) 393.

88. N.F. Mott., Trans. Met. Soc. AIME, 218 (1960) 962.

89. P.B. Hirsch and D.H. Warrington, Phil. Mag., 6 (1961) 735.

90. H. Wiedersich, J. Metals, 16 (1964) 425.

91. F.R.N. Nabarro, Adv. Phys., 1 (1952) 268.

92. A.W. Thompson, Acta Metall., 23 (1975) 1337.

93. D. Kuhlmann-Wilsdorf, Metall. Trans., 1 (1970) 3173.

94. M.N. Bassim and M.R. Bayoumi, Mater. Sci. Eng., 81 (1986) 317.

95. M.N. Bassim and X.B. Huang, Mater. Sci. Eng., 96 (1987) 159.

96. D. Broek, Eng. Fract. Mech., 5 (1973) 55.

97. S.H. Goods and L.M. Brown, Acta Metall., 27 (1979) 1.

98. A.S. Argon, J. Im, and R. Safoglu, Metall. Trans. A, 6 (1975) 825.

99. J.R. Fisher and J. Gurland, Met. Sci., 15 (1981) 193.

100. J. Gurland and J. Plateau, Trans. ASM, 56 (1963) 351.

101. F.A. McClintock, S.M. Kaplan, and C.A. Berg, Int. J. Fract. Mech., 2 (1966) 614.

102. D.S. Wilkinson and V. Vitek, Acta Metall., 30 (1982) 1723.

103. H.G.F. Wilsdorf, Mater. Sci. Eng., 59 (1983) 1.

104. J.N. Greenwood, D.R. Miller, and J.W. Suiter, Acta Metall., 2 (1954) 250.

105. R.W. Bauer and H.G.F. Wilsdorf, Scr. Metall., 7 (1973) 1213.

106. R.N. Gardner, T.C. Pollock, and H.G.F Wilsdorf, Mater. Sci. Eng., 29 (1977) 169.

107. R.N. Gardner and H.G.F. Wilsdorf, Metall. Trans. A, 11A (1980) 653.

108. T.C. Pollock and H.G.F. Wilsdorf, Mater. Sci. Eng., 29 (1983) 7.

109. K. Jagannadham, T.C. Pollock, and H.G.F.Wilsdorf, Mater. Sci. Eng. (1989) submitted for publication.

110. K.F. Amouzouvi and M.N. Bassim, Mater. Sci. Eng., 62 (1984) 137.

111. M.N. Bassim, Mater. Sci. Eng., 95 (1987) 199.

112. "Standard Methods of Tension Testing of Metallic Materials: Designation E8-86", ASTM Annual Book of Standards, 1986.

113. R.J. Klassen, "The Ductile Fracture of HSLA Steel", MSc. Thesis, University of Manitoba, Winnipeg, Manitoba, 1985.

114. P.W. Bridgman, ASM Trans. Quart., 32 (1944) 553.

115. E.R. Marshall and M.C. Shaw, Trans. ASM, 44 (1952) 716.

116. D. Tabor, J. Inst. Metals, 79 (1951) 1.

117. G.F. Vandervoort, "Metallography: Principles and Practice", McGraw-Hill, New York (1984) Chapter 6.

118. J.E. Hilliard and J.W. Cahn, Trans. AIME., 221 (1961) 344.

119. C.W. Corti, P. Cotterill, and G.A. Fitzpatrick, Int. Metall. Reviews, 19 (1974) 77.

120. A.W. Thompson, Metallography, 5 (1972) 366.

121. J.R. Low and F. Garafalo, Proc. Soc. Exp. Stress Anal., 4 (1947) 16.

122. M.H. Loretto and R.E. Smallman, "Defect Analysis in Electron Microscopy", J. Wiley and Sons Inc., New York, 1975, p. 49.

123. N. Hansen and D. Kuhlmann-Wilsdorf, Mater. Sci. Eng., 81 (1986) 141.

124. C.D. Beachem, Metall. Trans. A., 6A (1975) 377.

125. A.J. Shume, M.Sc. Thesis, University of Manitoba, Winnipeg, Manitoba (1989).

126. M. Gensamer, E.B. Pearsall, W.S. Pellini, and J.R. Low, Jr., Trans. ASM, 30 (1942) 983.

127. B.E. O'Donnelly, R.L. Reuben, and T.N. Baker, Metals Tech., 11 (1984) 45.

128. B.E. O'Donnelly and T.N. Baker, Mater. Sci. Eng., 84 (1986) 131.

129. T. Gladman, I.D. McIvor, and F.B. Pickering, J. Iron Steel Inst., 210 (1972) 916.

130. L. Yumen and Z. Jingen, Mater. Sci. Eng., 84 (1986) 137.

131. M.N. Bassim, R.J. Klassen, M.R. Bayoumi, and H.G.F. Wilsdorf, Mater. Sci. Eng., 92 (1987) 107.

132. L.E. Miller and G.C. Smith, J. Iron Steel Inst., 208 (1970) 998.